THEORETICAL AND NUMERICAL INVESTIGATION OF InAs/GaAs QUANTUM DOT SOLAR CELL TO IMPROVE THE POWER CONVERSION EFFICIENCY

By

Tewodros Adaro Gatissa

A DISSERTATION SUBMITTED TO THE GRADUATE PROGRAM IN PARTIAL FULFILLMENT OF THE REQUIREMENTS FOR THE DEGREE OF DOCTOR OF PHILOSOPHY

AT

ADDIS ABABA UNIVERSITY

ADDIS ABABA, ETHIOPIA

MAY, 2024

ADDIS ABABA UNIVERSITY
DEPARTMENT OF
PHYSICS

The undersigned hereby certify that they have read and recommend to the Graduate Programs College of Natural and Computational Sciences for acceptance a thesis entitled "**Theoretical and Numerical Investigation of InAs/GaAs Quantum Dot Solar Cell to Improve the Power Conversion Efficiency**" by **Tewodros Adaro Gatissa** in partial fulfillment of the requirements for the degree of **Doctor of Philosophy**.

Dated: May, 2024

Research Supervisors: _____
Prof. Teshome Senbeta

_____
Dr. Belayneh Mesfin

External Examiner: _____
Prof. Mesfin Abayneh

Internal Examiner: _____
Dr. Newayemedhin Aberra

Chairperson: _____
Dr. Chernet Amente

ADDIS ABABA UNIVERSITY

Date: **May, 2024**

Author: **Tewodros Adaro Gatissa**

Title: **Theoretical and Numerical Investigation of InAs/GaAs Quantum Dot Solar Cell to Improve the Power Conversion Efficiency**

Department: **Physics**

Degree: **Ph.D.** Convocation: **June** Year: **2024**

Permission is herewith granted to Addis Ababa University to circulate and to have copied for non-commercial purposes, at its discretion, the above title upon the request of individuals or institutions.

Signature of Author

This thesis is dedicated to my sister Menbere Adaro Gatissa

RIP my beloved sister

Contents

List of Tables

List of Figures

Abstract

The concept of introducing an intermediate band to overcome the efficiency limit of single-bandgap solar cells was proposed by Luque and Martí in 1997. It is predicted that utilising the intermediate band for multi-photon absorption can significantly improve the photocurrent generation without accompanying output voltage loss. Quantum dots (QDs) have been proposed as a means for implementing intermediate band solar cells (IBSCs) to absorb low energy photons, due to their quantum confinement of carriers. The work reported in this thesis is concerned with the theoretical and numerical investigation of quantum dot solar cell (QDSC) using $InAs$ QD multi-layers embedded in the i-region of a $GaAs$ $n^+ - i - p^+$ structure. In particular, the dependence of QDSC parameters on the number of QD layers, QD size, and size dispersion and the impact of inserting $InAs$ QD multi-layers in the middle subcell of $Ga_{0.51}In_{0.49}P/GaAs/Ge$ triple-junction quantum dot solar cell (3J-QDSC). Numerical simulations show that, the solar cell parameters are strongly dependent on the number of QD layers, the average size and size dispersion of QDs. A maximum efficiency is obtained at optimum number of QD layers, QD size, and size dispersion. Above or below this optimal value degrades the efficiency of QDSC. The current density-voltage characteristics have been simulated and discussed for triple junction solar cell with and without $InAs$ QD. Inserting $InAs$ QDs increases the short circuit current and efficiency of 3J-QDSC (40.1%) with small degradation in open circuit voltage. In general, inserting optimized size, size dispersion, number of $InAs$ QD layers in the i-region of a $GaAs$ solar cell as well as in the middle subcell of triple-junction $Ga_{0.51}In_{0.49}P/GaAs/Ge$ solar cell improves both the short circuit current density and the efficiency of the solar cell with a small degradation in open circuit voltage.

Acknowledgements

Above all, I thank God for all of His blessings and direction!

I would like to express my deepest gratitude to my supervisors Prof. Teshome Senbeta and Dr. Belayneh Mesfin, for their crucial advise, respect, understanding, and scientific and academic insights that allowed the work to be completed successfully.

I am extremely grateful to the Department of Physics of Addis Abeba University for its financial support.

I would like to extend my sincere thanks to Bonga College of Education for sponsoring my study.

I would like to express my deepest appreciation to all staff members in the Department of Physics of Addis Ababa University.

Special appreciation to W/ro Tsilat for her persistent and unwavering treatment at the Department of Physics.

Words cannot explain how grateful I am to my mother-in-law, Zewko, for raising and taking care of my boys.

This journey would not have been possible without the love, patience, encouragement, and constant support of my wife, Miheret Hundessa, and my sons, Nathan and Christian Tewodros.

I would also want to thank my brother, Dawit Habte, and sisters, Tigist and Senayet Adaro, for their encouragement and support.

Many thanks to all of my friends and colleagues, particularly Abeba Yohannes, Samuel Kasahun, Mohammed Geta, and Daniel Birhanu, for our insightful conversations.

Tewodros Adaro

Addis Ababa, Ethiopia

May, 2024

Chapter 1

Introduction

1.1 Background

The ability to generate and use all kinds of energy sources has greatly contributed to the civilization we have reached today. The increase in the world population and the modern lifestyle of people has recently increased the demand for energy. According to the U. S. Energy Information Administration (EIA) prediction, global energy consumption will rise by 34% between 2022 and 2050 [1]. Therefore, generating additional and sustainable energy to match energy demand with energy supply is non-negotiable. Because of increased energy demand, as well as existing policy and energy security concerns, renewable energy sources, particularly solar and wind, must grow faster than any other energy source. By 2050, the installed power capacity must increase to $1\frac{1}{2}$ to 2 times what it was in 2022 in order to fulfil rising global energy demands (Fig. 1.1). In 2022, liquid fuels, natural gas, and coal accounted for more than half of global power generation. It is predicted that, Zero-carbon technologies will account for 81% to 95% of new global power generation capacity between 2022 and 2050 [1].

For decades, we have relied heavily on fossil fuels. Climate change is now predominantly believed to be caused by an increase in greenhouse gas concentrations in the atmosphere, such as CO_2, which is the byproduct of the combustion of fossil fuels. According to the Intergovernmental Panel on Climate Change (IPCC), the climate system is unquestionably

warming, as demonstrated by rising global average air and ocean temperatures, widespread melting of snow and ice, and rising global average sea level [2]. It is indisputable that we

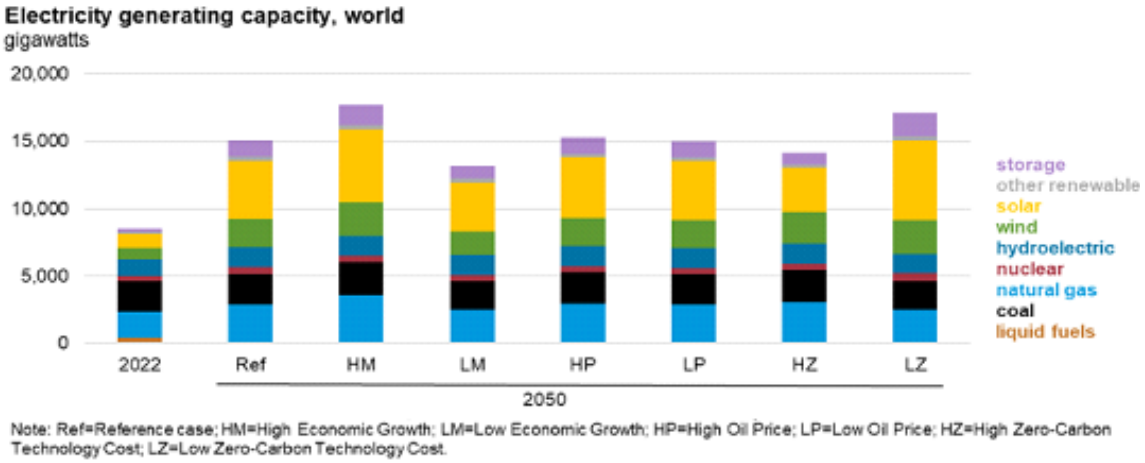

Figure 1.1: World energy generation capacity. Reproduced from Ref. [1].

must switch from fossil fuels to renewable energy.

The urge to shift from fossil fuels and towards renewable energies has been encouraged not just by the depletion of oil and gas supplies, but also by the need to reduce greenhouse gas emissions and avert global climate change. It is anticipated that replacing all energy demand with renewable energy will be a significant task for humanity. The difficulty then becomes is determining how to generate enough energy to meet the predicted growth in energy demand without producing greenhouse gases.

Solar energy has emerged as the most promising energy source to address this issue due to the enormous amount of solar radiation that reaches the earth's surface as well as recent significant advancements in solar energy technology. Planet Earth has received enough solar radiation to meet its energy needs. With current technologies, every square meter of land on Earth receives enough sunlight to generate 1,700 kWh of electricity annually. The entire solar energy that reaches the Earth's surface has the potential to meet current global energy needs 10,000 times more [3]. There is a huge gap between the amount of

solar energy used nowadays and its enormous potential. Figure 1.2 compares the availability of solar energy to that of other renewable energy sources. Widespread use of solar energy, which is free from environmental pollution, is not something that should be given time. However, converting solar energy into electrical energy in a more efficient and on a large scale is believed to be extremely challenging. According to the International Energy

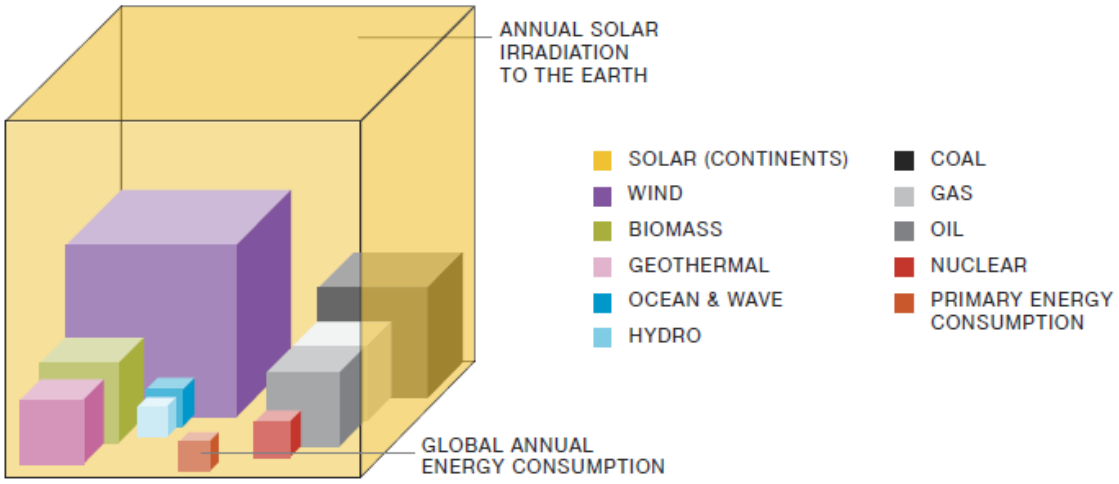

Figure 1.2: Solar irradiation versus established global energy resources (Fossil fuels are expressed with regard to their total reserves whereas renewable energies are expressed to their yearly potential). Reproduced from Ref. [2].

Agency forecast, non-fossil fuel sources such as solar, wind, hydropower, and nuclear will meet the majority of global electricity demand by 2050 [1]. Currently, solar energy contributes about 5.5% of global electricity generation, up from 4.6% in 2022 [4].

Solar power is an appealing solution for a long-term, sustainable energy source. Its supply greatly outstrips any foreseeable future energy demand. It is completely environmentally friendly, and its energy is freely delivered from the sun to the Earth. But using the sun's energy is not without difficulties. Overcoming the challenges to widespread solar power generation will necessitate engineering breakthroughs in multiple areas, including absorbing solar energy, converting it to useful forms, and storing it for use when the sun is obscured. The United States National Academy of Engineering concludes in its grand

engineering challenges report that making solar energy more efficient and inexpensive is one of the major engineering challenges of the twenty-first century [5]. If the engineering constraints of increasing the efficiency and lowering the cost of solar cells are overcome, solar power will demonstrate its dominance over fossil fuels as a sustainable driving force for civilization's long-term success.

The Photovoltaic effect was first discovered by, a French physicist, Alexandre-Edmund Becquerel in 1839 [6]. His finding laid foundations for solar cell technology. The photovoltaic effect is the fundamental basis of solar cell technology. In 1870s, the photovoltaic (PV) effect was first explored in solids such as selenium. It was expensive and had low efficiency (1% to 2%). A significant advancement in solar cell technology occurred, when the Czochralski method for producing highly pure crystalline silicon was developed [7]. In 1954, researchers at Bell Telephone Laboratory developed the first silicon single-crystalline solar cell with a 6% efficiency [8]. Within a few years, this efficiency was increased to 11% [7]. The photoconversion efficiency of silicon solar cells increased to 26.6% in 2017 [9], while a new world record efficiency of 26.81% was reported in 2023 [10], approaching the efficiency limits of silicon solar cells of 29.43% [11].

Until the 1973 global oil crisis, solar cells were used for space application, basically used for powering satellites. Due to the dramatic rise in oil prices, public interest in photovoltaic technology for terrestrial applications was growing. At the time, PV technology was transitioning from a specialty technology for space applications to a technology appropriate for terrestrial applications. In the late 1970s and early 1980s many companies began to develop PV modules and systems for terrestrial applications [12]. Solar cells are still vital for space applications, such as powering the International Space Station and orbiting satellites.

Solar cells are categorised into distinct groups based on the materials used in their manufacturing. In first generation solar cell technology, silicon (Si) is utilised in the production

of single crystalline and polycrystalline Si solar cells. Thin film solar cells are a second generation solar cell technology that employs materials such as amorphous Si [a-Si], cadmium sulphide [CdS], Cadmium Telluride [CdTe], Copper Indium Gallium DiSelenide [CIGS] etc. Third-generation solar cell technology applies advanced methods to harvest the maximum amount of solar energy incident on the solar cell and convert it more efficiently into electric energy. This category include dye sensitised solar cells, tandem solar cells, multi-junction solar cells, and quantum dot solar cells etc.

Single-junction solar cells may be able to reach air mass 1.5 (AM1.5) efficiencies of up to 30%–32% [13]. Some of the single junction solar cell which have been developed and demonstrated a good power conversion efficiency are Si (26.81% [10]), GaAs (27.6% [14]), CIGS (23.35% [15]), perovskite (23.6% [16]), Dye sensitised (11.9% [17, 18]), and Organic (15.2% [19]).

The variety of power loss mechanisms in solar cell devices make converting solar energy into usable electrical energy difficult [20]. The mismatch between the solar spectrum and the band gap of the semiconductor material is the most significant loss in single junction solar cells. Photons with energies less than the band gap cannot be absorbed (25.0%), and photons with energies considerably exceeding the band gap waste energy due to thermalization (29.8%) [21]. This energy loss due to spectral mismatch can be reduced by employing the intermediate band solar cell (IBSC) idea [22]. The principle of IBSC photovoltaic is to excite electrons two-step over a semiconductor band gap using an intermediate band [23]. The use of low-energy photons in conjunction with the intermediate band approach raises the maximum detailed balance efficiency from 40.7% to 63.1% [22].

Quantum Dots are semiconductor nanocrystals (NCs) that exhibit quantum confinement effects in all three dimensions. These quantum confinement effects allow their optical and electronic properties to be tuned by adjusting their shape and size, making their usage in optoelectronic materials attractive [24, 25]. A confined levels of quantum dot was proposed to obtain the operational principles of IBSC [26, 27]. The evidence of obtaining

three distinct quasi-Fermi levels [28, 29] and the generation of photocurrent by absorption of photons laying beneath the semiconductor band gap [26, 28, 29, 30], both of which are pillars of IBSC principles, has captured the interest of many researchers in the field of quantum dot solar cells.

Another popular method for avoiding these loss processes is to use a multijunction solar cell (MJSC) technique [13, 20]. A multi junction solar cell is made up of numerous single junction solar cells with varying bandgap energies joined by tunnel junctions [20]. The concept is based on the idea of stacking solar cells with different bandgaps to absorb a larger section of the solar spectrum and hence increase solar cell efficiency [13]. The multijunction solar cell technique can overcome the aforementioned most significant losses in single junction solar cells. The multijunction solar cell approach has several advantages, including the ability to capture a wide range of sunlight's wavelengths, which spans from ultraviolet to infrared [31] and the ability to minimise thermalization loss brought on by a high-energy photon absorbed by a material with a small bandgap [13]. In this thesis theoretical and numerical investigation of InAs/GaAs quantum dot solar cell to improve the power conversion efficiency was carried out.

1.2 Statement of the Problem

The most significant loss in conventional solar cells is caused by a spectral mismatch between the semiconductor band gap and the solar spectrum [32]. This issue can be reduced by using the intermediate band solar cell [22] and multi-junction solar cell concepts [13, 20]. The tunable band gap of quantum dots as a result of quantum confinement effect makes a good candidate for IBSC practical application [26, 27]. Several studies have demonstrated the splitting of three quasi-fermi levels [28, 29] and the improved spectral response in quantum dot solar cells [26, 28, 29, 30]. However, in numerous experimental reports [33, 34, 35, 36, 37, 38, 39, 40, 41, 42] the short circuit current density increases but

the open circuit voltage and the efficiency of QDSC decreases compared to the reference solar cell. This could be related to the number of quantum dots layers, quantum dot size, and quantum dots size non-uniformity (size dispersion).

Increasing the number of QD layers improves short circuit current but decreases the effective band gap, resulting in open circuit voltage deterioration. This competitive relationship between the number of QD layers and the effective band gap may result in the optimal number of QD layers for maximum efficiency.

When the size of QDs increases, the bandgap shift between the barrier conduction band and the intermediate band increases. This decreases electron escape from QDs to the barrier. As a result, larger QDs can easily recapture the photogenerated carrier during carrier transport [43]. This causes the recombination process to increase. When smaller QDs are employed, the bandgap shift is small. As a result, intermixing of quasi-Fermi level of conduction band and intermediate band could happen, which oppose the basic principle of IBSC. In addition, small QDs cannot absorb long wavelengths of light, which means less of the solar spectrum can be used. On the other hand, larger QDs absorb long wavelength light, but they are unfavorable for electron escape (transfer) due to larger recombination. In order to avoid recapturing of the photogenerated carrier and intermixing of quasi-Fermi level, appropriate size of QDs should be selected. In general, the competitive relationship between light absorption and electron escape from QD according to the size of the QDs might lead to the optimal QD size to provide maximum solar energy conversion efficiency. Since smaller size-dispersion QD ensembles have higher and sharper absorption peaks, they cover a lesser portion of the solar spectrum. On the other hand, larger size-dispersion QD ensembles have a lower absorption peak and a wider bandwidth that might causes stimulated emission problems. Therefore, the competitive relationship between peak absorption coefficient and line width broadening, could lead to an optimum QD size dispersion to provide maximum solar energy conversion efficiency.

Among the numerous technologies used to improve the conversion efficiency of solar cells,

the multi-junction (M-J) concept, especially the triple-junction (3-J) concept based on $InGaP$, $GaAs$ and Ge materials exhibit high efficiencies. Nevertheless, their performance is somehow restricted due to current limitation of the $GaAs$ middle subcell [44, 45, 46]. Inserting optimized size and number of layers of $InAs$ QD in the intrinsic region of n-i-p $GaAs$ subcell could bring both current match among the three subcells and efficiency improvement.

In this dissertation, first, the dependence of $InAs/GaAs$ quantum dot solar cells parameters on the number of quantum dot layers are investigated. Second, the effect of cubic and spherical $InAs$ quantum dot size and size dispersion on the QD absorption coefficient, the quantum dot photocurrent density and the performance of $InAs/GaAs$ quantum dot solar cells are studied. Finally, a theoretical model of a triple-junction quantum dot solar cell is developed using n/p $Ga_{0.51}In_{0.49}P$ (top subcell), n-i-p $InAs/GaAs$ QDSC (middle subcell), and n/p Ge (bottom subcell), and the effect of $InAs$ quantum dot insertion in the middle subcell of triple-junction solar cells is analysed. Therefore, consideration of numerical approaches is important. The numerical solutions and simulated findings in this work were generated using Mathematica 8 or 9.

1.3 Objectives of the Study

1.3.1 General Objective

The general objective of the study is

- Investigating an $InAs/GaAs$ quantum dot solar cell theoretically and numerically to improve the power conversion efficiency.

1.3.2 Specific Objectives

The specific objectives of the study are

- To investigate the dependence of quantum dot solar cell parameters on the number of quantum dot layers.
- To study the effect of cubic and spherical quantum dot size and size dispersion on the quantum dot absorption coefficient, quantum dot photocurrent density, and performance of quantum dot solar sells.
- To investigate the impact of inserting an $InAs$ quantum dot in the middle subcell of a triple-junction $Ga_{0.51}In_{0.49}P/GaAs/Ge$ solar cell.

1.4 Thesis Layout

Chapter 2 deals with the physics of n-p junction and n-p junction solar cell. In this chapter analytical equations of the dark current density, the short circuit current density, the open circuit voltage, and the efficiency of the solar cell are derived. Chapter 3 discuses about the theoretical model of $InAs/GaAs$ QDSC and $Ga_{0.51}In_{0.49}P/GaAs/Ge$ 3J-QDSC as well as the methods used for this study. The main results of the study are discussed in Chapters 4, 5, and 6. The dependence of quantum dot solar cell parameters on the number of quantum dot layers are discussed in Chapter 4. Chapter 5 study the effect of cubic and spherical quantum dot size and size dispersion on the quantum dot absorption coefficient, the quantum dot photocurrent density, and performance of quantum dot solar cells. The impact of inserting an $InAs$ quantum dot in the middle subcell of a triple-junction $Ga_{0.51}In_{0.49}P/GaAs/Ge$ solar cell is discussed in Chapter 6. Finally, summary, limitation of the study and recommendation for future work are presented in Chapter 7.

Chapter 2

Literature Review

Understanding the interaction of light and semiconductors is required for a complete comprehension of solar cells. The photovoltaic energy conversion process, sunlight as the main energy source, and the solar cell itself are all explained in this chapter. The next section includes a brief overview of solar irradiation, followed by a discussion of charge carriers' transport properties in semiconductors. The basic of semiconductors, the formation of n-p junctions, and solar cell operation are explained, and then current densities of n-p junction solar cells under illumination and in the dark are derived. Comprehensive explanations are also held regarding the intermediate band solar cells, the quantum dot intermediate band solar cells, and the multi-junction solar cells.

2.1 The Solar Resource

To generate electron-hole pairs in semiconductor materials, photons with the appropriate energy must be absorbed. Consequently, understanding the spectral distribution of solar radiation is essential [12]. Sunlight is composed of a wide range of wavelengths radiation which cover the ultraviolet, visible, and infrared portions of the electromagnetic spectrum. The visible wavelength range (300 – 800 nm) has the most solar radiation, with a peak in the blue-green wavelength range [47]. The number of photons with a given energy as

a function of wavelength (λ) is known as the spectral distribution of solar radiation. The sun is a complicated radiator and its spectrum is comparable to that of a black body at 6000 K [48]. Figure 2.1 depicts the AM0 spectrum (the standard for the extraterrestrial spectrum and the standard defined for space solar cell applications), the AM1.5 spectrum (the standard for the terrestrial solar spectrum and the standard defined for terrestrial solar cell applications), and the standard solar spectra of a blackbody at 6000 K.

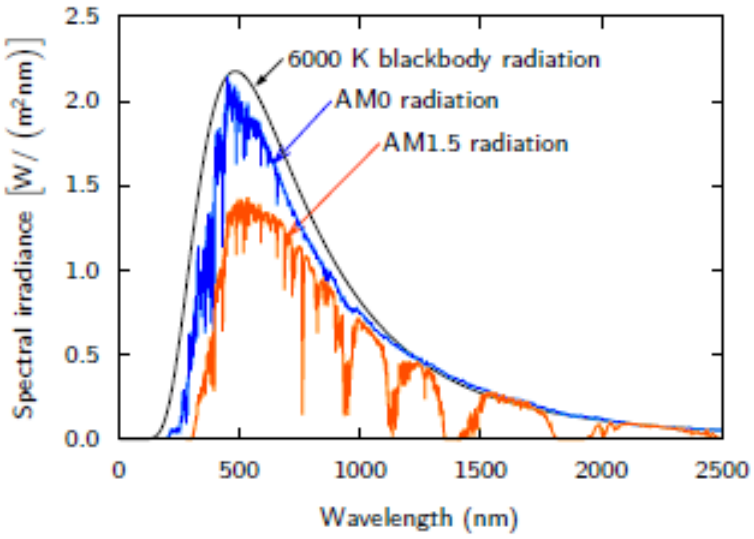

Figure 2.1: Different solar spectra: the blackbody spectrum of a blackbody at 6000 K, the extraterrestrial AM0 spectrum and the AM1.5 spectrum. Reproduced from Ref. [12].

The solar radiation spectrum is described by two parameters: spectral photon flux ($\phi_0(E)$) and spectral irradiance ($I_e(E)$) [12]. The spectral photon flux (ϕ_0), which is the number of photons with energy in the range E to $E + dE$ emitted through unit area per unit solid angle per unit time, is given by [47]

$$\phi_0(E) = \frac{2F_s}{h^3c^2} \frac{E^2}{\exp\left(\frac{E}{K_B T_S}\right) - 1}, \tag{2.1.1}$$

where K_B is the Boltzmann constant, h is the Planck constant, c is the speed of light in vacuum, and the geometrical factor F_s is obtained by integrating over the appropriate angular range. This range is a hemisphere at the black body's surface, where $F_s = \pi$. The

angular range decreases away from the surface and it is expressed by

$$F_s = \pi \sin^2 \theta_{sun}, \tag{2.1.2}$$

where θ_{sun} is the half angle that the radiating body subtains to the flux measurement site. $\theta_{sun} = 0.26^0$ for the sun as seen from Earth, F_s is decreased by a factor of 4.6×10^4 to $2.16 \times 10^{-5}\pi$.

The relationship between the photon flux density ($\phi_0(E)$) and the emitted energy flux density, or irradiance, $I_e(E)$, is [47]

$$I_e(E) = E \times \phi_0(E) = \frac{2F_s}{h^3c^2} \frac{E^3}{\exp\left(\frac{E}{K_B T_S}\right) - 1}. \tag{2.1.3}$$

The total emitted power density, or $\sigma_S T_S^4$, is obtained by integrating Eqn. (2.1.3) over E, where σ_S is Stefan's constant.

$$\sigma_S = \frac{2\pi^5 K_B^4}{15c^2h^3}. \tag{2.1.4}$$

At the surface, the sun produces a power density of $6.2 \times 10^7\ Wm^{-2}$, and this is reduced to $1353\ Wm^{-2}$ just outside the Earth's atmosphere [47]. The irradiance at AM0 is $I_e(AM0) = 1353\ Wm^{-2}$.

Solar radiation on Earth is attenuated by the scattering and absorption of solar energy by air molecules, dust, and aerosols in the atmosphere [12]. The intensity and spectral distribution of terrestrial solar radiation vary based on Earth's location and the Sun's position in the sky [47]. The optical air mass is defined as the ratio of the actual path length of sunlight to this minimal distance as defined by Eqn. (2.1.5). Specific solar spectra are labeled AMm_r (read: air mass m_r) [48]. The optical air mass is unity when the Sun is at its zenith, and the spectrum is known as the air mass 1 (AM1) spectrum

(Fig. 2.2). When the Sun is at an angle θ_z with the zenith, the air mass is given by [12, 48]

$$m_r = \frac{L_S}{L_z} = \frac{1}{\cos[\theta_z]}. \tag{2.1.5}$$

We receive an AM1.5 spectrum, when the Sun is 48.2^o from the zenith. The solar spectrum is attenuated by this air thickness to a mean irradiance of about 900 Wm^{-2}. For the sake of convenience, the $AM1.5$ spectrum is normalised to have an integrated irradiance of 1000 Wm^{-2}.

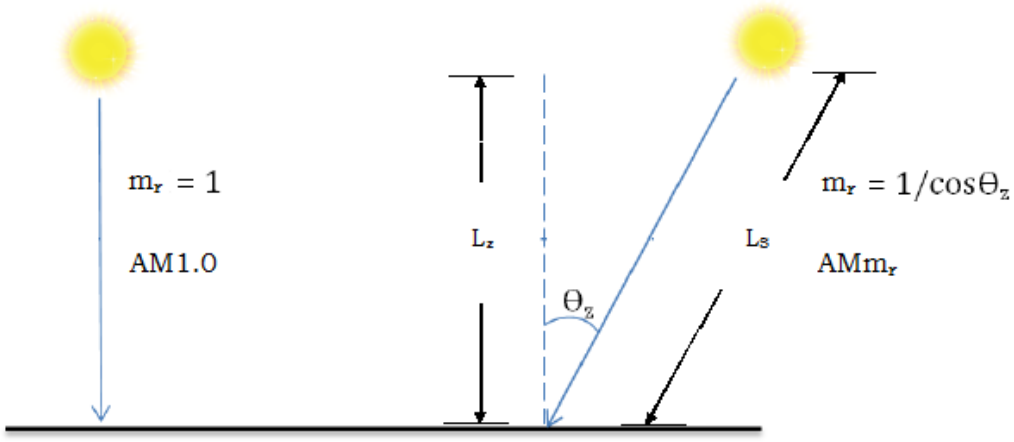

Figure 2.2: The schematic of Air Mass.

2.2 Transport Properties

The carrier transport phenomena are the foundation for determining the current-voltage characteristics of semiconductor devices. Currents are generated by the net flow of electrons and holes in a semiconductor. The movement of these charged particles is known as transport. There are two main transport mechanisms in a semiconductor crystal: drift (charge movement caused by electric fields) and diffusion (charge flow caused by density gradients).

2.2.1 Carrier Drift

The net movement of a charged particle in reaction to an electric field is called drift. The net charge drift results in a drift current. The electron and hole drift current densities are defined by Eqns. (2.2.1) and (2.2.2), respectively and the total drift current density expressed by Eqn. (2.2.3) [49].

$$J_n^{drift} = qn\mu_n\xi, \tag{2.2.1}$$

$$J_p^{drift} = qp\mu_p\xi, \tag{2.2.2}$$

$$J^{drift} = q(n\mu_n + p\mu_p)\xi, \tag{2.2.3}$$

where q is magnitude of the electron charge, n is the number of electrons, p is the number of holes, μ_n is the electrons mobility, μ_p is the holes mobility, and ξ is the electric field.

2.2.2 Carrier Diffusion

The diffusion-related particle transport is propelled by a gradient in the concentration of particles within a semiconductor. Current density resulting from diffusion is proportional to the gradient in particle concentration. The electron and hole diffusion current densities are defined by Eqns. (2.2.4) and (2.2.5), respectively and the total diffusion current density is expressed by Eqn. (2.2.6) [49].

$$J_n^{diff} = qD_n\nabla n, \tag{2.2.4}$$

$$J_p^{diff} = -qD_p\nabla p, \tag{2.2.5}$$

$$J^{diff} = q(D_n\nabla n - D_p\nabla p). \tag{2.2.6}$$

The total current due to both drift and diffusion is expressed by Eqn. (2.2.7)

$$J = q(D_n \nabla n - D_p \nabla p) + q(n\mu_n + p\mu_p)\xi. \tag{2.2.7}$$

The constants of proportionality, D_n and D_p, are referred to as electron and hole diffusion coefficients, respectively.

A one-dimensional drift-diffusion current density is written as

$$J_n = qD_n \frac{dn_p}{dx} + qn_p\mu_n\xi_x, \tag{2.2.8}$$

for minority carrier electron and

$$J_p = -qD_p \frac{dp_n}{dx} + qp_n\mu_p\xi_x, \tag{2.2.9}$$

for minority carrier hole.

2.3 Continuity Equation

Any divergence in the current density from any particular point within the material is due to the differences in particle generation and recombination, as well as variations in the carrier density at that location. The continuity equation demonstrates this.

The continuity equation for electrons is given by [50]

$$\vec{\nabla} \cdot \vec{J_n} = -q(G_n - R_n - \frac{\partial n}{\partial t}). \tag{2.3.1}$$

The continuity equation for holes is given by [50]

$$\vec{\nabla} \cdot \vec{J_p} = q(G_p - R_p - \frac{\partial p}{\partial t}), \tag{2.3.2}$$

where G_n and G_p are the electron and hole generation rate, respectively, caused by external influences such as the optical excitation with photons or impact ionization under large electric fields.

The recombination rates in p- and n-type materials depend on the minority carrier lifetimes and concentrations. The minority carrier electron recombination rate in the p-region is defined as [49]

$$R_n = \frac{n_p - n_{po}}{\tau_n}, \tag{2.3.3}$$

where n_p is the total minority carrier electron concentration, n_{po} is the thermal-equilibrium minority carrier electron concentration, and τ_n is the minority carrier electron lifetime in the p-region.

The minority carrier hole recombination rate in the n-region is defined as [49]

$$R_p = \frac{p_n - p_{no}}{\tau_p}, \tag{2.3.4}$$

where p_n is the total minority carrier hole concentration, p_{no} is the thermal-equilibrium minority carrier hole concentration, and τ_p is the minority carrier hole lifetime in the n-region.

2.4 Basics of Semiconductors

When a semiconductor material is exposed to light, it absorbs photons with energies (E) greater than or equal to the semiconductor bandgap (E_g). Electron-hole (E-H) pairs are produced when the absorbed energy breaks down covalent bonds. Solar energy production relies on the creation of these E-H pairs. A semiconductor appears transparent to photons with energy below the bandgap. Photons with energy greater than the bandgap will dissipate as heat. Basically, absorption is the transfer of electrons from the valence band (VB) to the conduction band (CB). After a long enough period of time, the electrons and holes

created in the semiconductor material during the absorption process will recombine again. Impurities and defects in the semiconductor, either on the surface or inside, promote this recombination process.

In semiconductor materials, photons with higher energy have shorter absorption depths and are absorbed at shallower depths, while photons with lower energy have greater absorption depths and are absorbed at greater depths. Assuming that every absorbed photon results in the creation of one electron-hole pair, the rate at which electron-hole pairs are generated at a distance x from the semiconductor surface is given by

$$G(E,x) = \alpha(E)\phi_0(E)(1-R(E))\exp[-\alpha(E)x], \tag{2.4.1}$$

where $\alpha(E)$ is the absorption coefficient, $\phi_0(E)$ is the number of incident photons per area per time per unit photon energy, and $R(E)$ the fraction of these photons reflected from the surface.

The absorption coefficient is a measure of how deeply photons of a specific energy are absorbed in a semiconductor material. For direct bandgap semiconductors, the absorption coefficient is given by [51]

$$\alpha(E) = \frac{\pi q^2 \hbar}{2\epsilon_r^{1/2}\epsilon_o m_o c E}\left(\frac{2|p_{cv}|^2}{m_o}\right)\left[\frac{\sqrt{2}(m_r^*)^{3/2}(E-E_g)^{1/2}}{\pi^2\hbar^3}\right]\left(\frac{2}{3}\right), \tag{2.4.2}$$

where ϵ_r is relative permittivity, m_r^* is the reduced mass of electron-hole pair, p_{cv} the momentum matrix, E_g is the band gap and E is the photon energy. Here units of E_g and E are in eV and the unit of $\alpha(\hbar\omega)$ is $1/\mu m$. Figure 2.3 shows a plot of the absorption coefficient as a function of photon energy for Si and GaAs. Since silicon has an indirect bandgap, the absorption process involves an additional particle called a phonon. Consequently, there is a lower chance of light absorption than with direct bandgap materials. As a result, Si absorption coefficient is lower than GaAs, a direct bandgap material. GaAs and other direct bandgap materials are therefore desirable for use in optical devices including lasers,

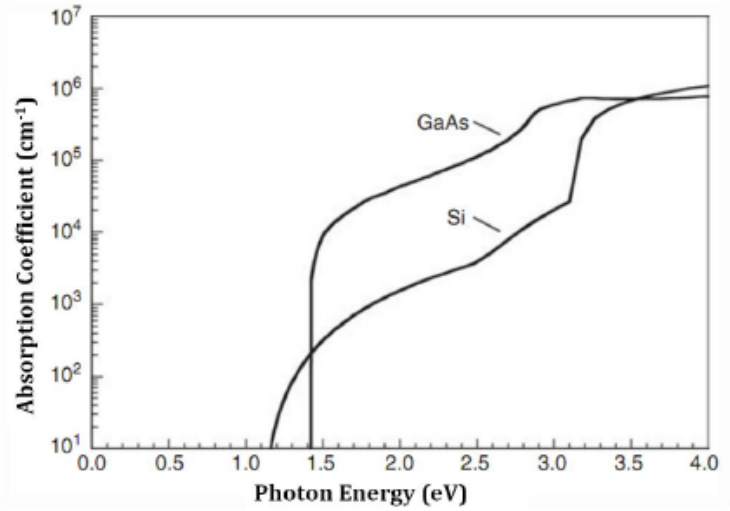

Figure 2.3: Absorption coefficient as a function of photon energy for Si and $GaAs$ at 300 K. Reproduced from Ref. [52].

photodiodes, and solar cells [52].

2.5 n-p Junction

The semiconductor junction is essential to solar cell operation. When an n-type semiconductor material with donor concentration N_D is put in contact with a p-type material of acceptor concentration N_A, the difference in charge densities on either side of the contact will cause charges to diffuse across the interface; holes into the n-type region, and electrons move into the p-type region. Near the interface, almost all dopant atoms get ionised; as seen in Fig. 2.4, electrons from the n-region move to occupy acceptor sites in the p-region, leaving positive stationary ions in the n-region [53]. There is no net current flow in thermal equilibrium because the drift and diffusion currents for each type of carrier exactly balance. The space-charge area is the region that separates n-type semiconductors from p-type semiconductors. Since it is essentially depleted of both holes and electrons, it is also frequently referred to as the depletion area. The regions on each side of the depletion region are effectively charge-neutral (sometimes referred to as quasi-neutral) if the p-type

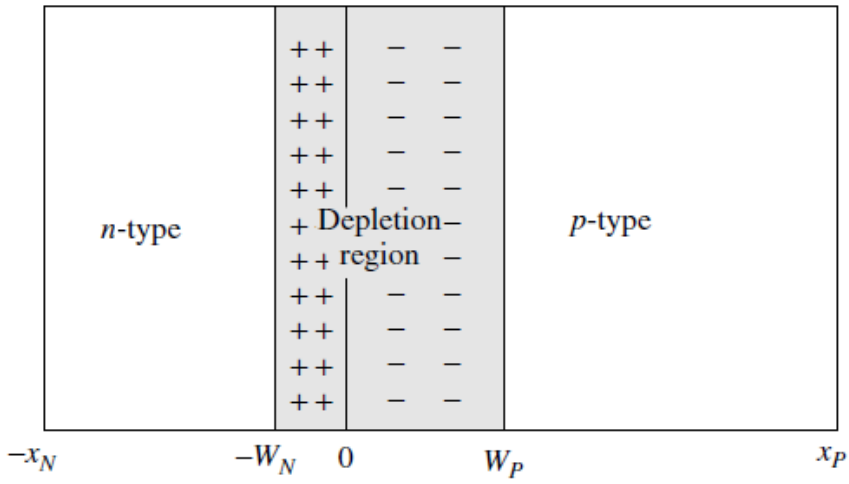

Figure 2.4: n-p junction. Reproduced from Ref. [52].

and n-type regions are thick enough. The built-in voltage, or V_{bi}, is the electrostatic potential difference that results from the junction creation. It results from the electric field that the depletion region's positive and negative space charges produce.

Since there is only one acceptor and one donor level in this scenario, Poisson's equation (Eqn. (2.5.1)) governs the electrostatics [54].

$$\nabla^2\phi = \frac{q}{\varepsilon_{sc}}(n_o - p_o + N_A^- - N_D^+), \tag{2.5.1}$$

where ϕ is the electrostatic potential, ε_{sc} is the electric permittivity of the semiconductor, p_o is the equilibrium hole concentration, n_o is the equilibrium electron concentration, N_A^- is the ionized acceptor concentration, and N_D^+ is the ionized donor concentration.

A simple one-dimensional (1D) pn-junction is shown in Fig. 2.4. It has a uniformly doped N_D on the n-type side and N_A on the p-type side, with the metallurgical junction at $x = 0$. For the sake of simplicity, it is assumed that the dopants are fully ionised and that each side is nondegenerately doped.

Within the depletion region, defined by -$W_N < x < W_P$, it can be assumed that p_o and

n_o are both negligible compared to $\mid N_A - N_D \mid$ so that Eqn. (2.5.1) can be simplified to

$$\nabla^2\phi = -\frac{q}{\varepsilon_{sc}}N_D, \qquad for \quad -W_N < x \leq 0 \tag{2.5.2}$$

$$\nabla^2\phi = \frac{q}{\varepsilon_{sc}}N_A, \qquad for \quad 0 \leq x < W_P \tag{2.5.3}$$

Outside the depletion region, charge neutrality is assumed and

$$\nabla^2\phi = 0, \qquad for \quad x \leq -W_N \quad and \quad x \geq W_P \tag{2.5.4}$$

This is called the depletion approximation in general.

The built-in voltage, or V_{bi}, is the electrostatic potential difference across the junction and may be found by integrating the electric field, or $\xi = -\nabla\phi$.

$$\int_{-W_N}^{W_P} \xi dx \equiv -\int_{-W_N}^{W_P} \frac{d\phi}{dx}dx \equiv -\int_{-W_N}^{W_P} d\phi \equiv \phi(-W_N) - \phi(W_P) = V_{bi} \tag{2.5.5}$$

Solving Eqns. (2.5.2), (2.5.3), and (2.5.4) and defining $\phi(W_P) = 0$, gives

$$\phi(x) = V_{bi}, \qquad x \leq -W_N \tag{2.5.6}$$

$$\phi(x) = V_{bi} - \frac{qN_D}{2\varepsilon_{sc}}(x + W_N)^2, \quad -W_N < x \leq 0 \tag{2.5.7}$$

$$\phi(x) = \frac{qN_A}{2\varepsilon_{sc}}(x - W_P)^2, \qquad 0 \leq x < W_P \tag{2.5.8}$$

$$\phi(x) = 0, \qquad x \geq W_P \tag{2.5.9}$$

The electrostatic potential must be continuous at $x = 0$. Therefore, from Eqns. (2.5.7) and (2.5.8),

$$V_{bi} - \frac{qN_D}{2\varepsilon_{sc}}W_N^2 = \frac{qN_A}{2\varepsilon_{sc}}W_P^2 \tag{2.5.10}$$

Here, too, the electric field is continuous since there is no interface charge at the metallurgical junction. Therefore, the derivative of Eqns. (2.5.7) and (2.5.8) with respect to x and evaluated at $x = 0$ gives

$$N_A W_P = N_D W_N. \tag{2.5.11}$$

Solving Eqns. (2.5.10) and (2.5.11) for W_N and W_P gives

$$W_N = \left(\frac{2\varepsilon_{sc} V_{bi}}{q} \left[\frac{N_A}{N_D} \right] \left[\frac{1}{N_A + N_D} \right] \right)^{1/2}, \tag{2.5.12}$$

$$W_P = \left(\frac{2\varepsilon_{sc} V_{bi}}{q} \left[\frac{N_D}{N_A} \right] \left[\frac{1}{N_A + N_D} \right] \right)^{1/2}, \tag{2.5.13}$$

where W_P is the depletion width in the p-region and W_N is the depletion width in the n-region.

The total depletion or space charge region width (W) is the sum of the two components, or

$$W = W_N + W_P. \tag{2.5.14}$$

Using Equations (2.5.12) and (2.5.13), we obtain

$$W = \left(\frac{2\varepsilon_{sc} V_{bi}}{q} \left[\frac{N_A + N_D}{N_A N_D} \right] \right)^{1/2}, \tag{2.5.15}$$

where $\varepsilon_{sc} = \varepsilon\varepsilon_0$ is the permittivity of the semiconductor, ε is the relative permittivity or dielectric constant, ε_0 is the permittivity of free space, and V_{bi} is the built-in potential barrier and it is given by [53]

$$V_{bi} = \frac{K_B T}{q} \ln \left[\frac{N_A N_D}{n_i^2} \right], \tag{2.5.16}$$

where T is the temperature of the semiconductor, and n_i is the intrinsic concentration of electrons.

2.6 Solar Cell Operation

2.6.1 Ideal Solar Cells

When light strikes a solar cell, it creates a voltage and a current that are used to create electricity. The fundamental processes in a solar cells operation are the generation of light-generated carriers, the collection of these carriers to produce a current, the establishment of a high voltage across the solar cell, and the dissipation of power in an external load. Equation (2.6.1) provides the current generated by light as [55]

$$J_L = q \int_0^W G(x) CP(x) dx, \tag{2.6.1}$$

where J_L is the light-generated current density, W is the thickness of the device and $CP(x)$ is the collection probability at a depth of x into the material.

The current density–voltage characteristics of a solar cell can be written as [55]

$$J(V) = J_o \left(\exp[\frac{qV}{mK_BT}] - 1 \right) - J_L, \tag{2.6.2}$$

where J_o is the reverse saturated current density, m is the ideality factor, and J_L is the light-generated current density. The current density–voltage behaviour of a solar cell, as shown in Fig. 2.5(A) is essentially the superposition of the solar cells dark current with the light-generated current. The J-V curve is moved down into the fourth quadrant where power can be extracted. Figure 2.5(B) shows the equivalent circuit of a solar cell, which is a current source in parallel with a rectifying diode. The current source represents the photo-generation of current and the diode represents the radiative recombination within the cell. The ideality factor and the dark saturation current can be increased to account for non-radiative recombination in a non-ideal solar cell. Under open-circuit conditions, the diffusion diode current and the light-generated current cancel each other out and hence no current flows.

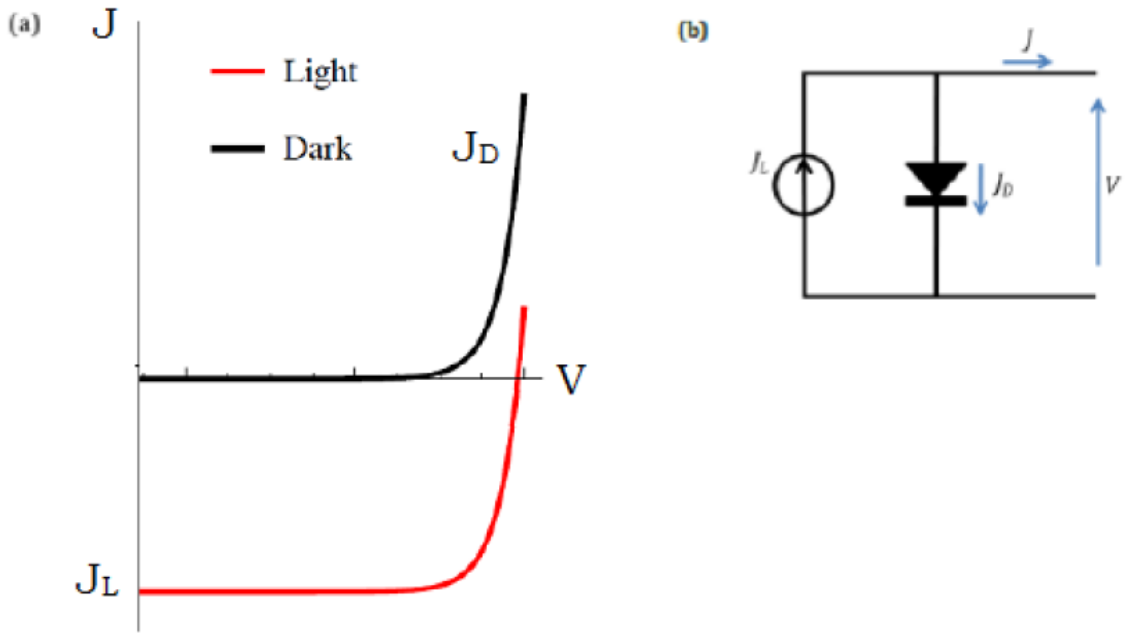

Figure 2.5: (A) J-V curve of a solar cell and (B) the equivalent circuit of a solar cell.

2.6.2 Losses in Solar Cells

Real solar cells have non-ideal characteristics due to losses that occur in the solar cell. A schematic that divides the losses into optical and electrical components is presented in Fig. 2.6. Lattice thermalisation results in a reduction in output voltage and sub-bandgap losses result in a reduction in output current. More than half of the losses in a single bandgap solar cell are accounted for these two optical losses alone: thermalization (29.8%) and below bandgap (25.0%) [21]. The output voltage is also decreased as a result of recombination losses.

2.6.3 Solar Cell Performance Parameters

Quantum Efficiency

Quantum efficiency (QE) is the ratio of the number of carriers collected by a solar cell to the number of incident photons at a given wavelength. If all photons of a particular wavelength are absorbed and carriers collected, then the QE at that wavelength is 1. This

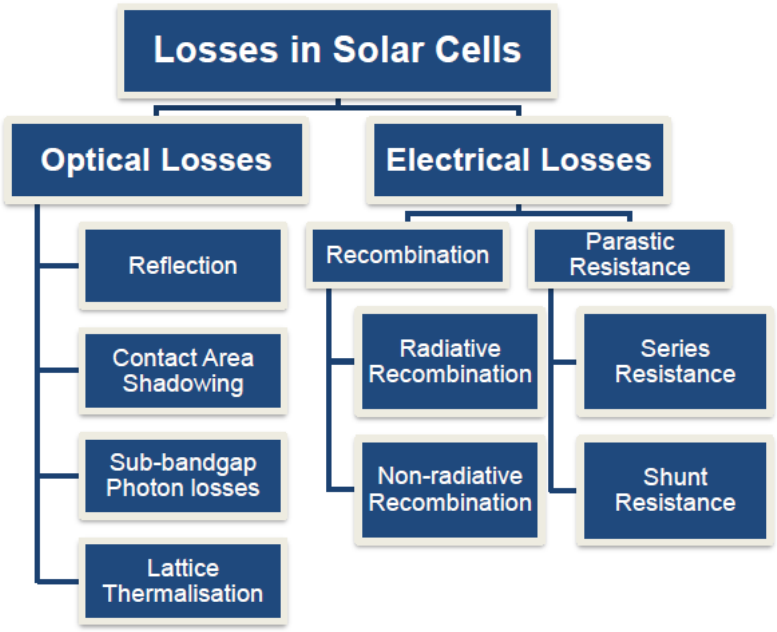

Figure 2.6: Types of losses in a solar cell.

is true for an ideal solar cell at all wavelengths. QE depends on the absorbing properties of the solar cell material and the carrier transport processes within it. The QE for an ideal and a practical solar cell is shown in Fig. 2.7. The tan/gold square line shown in Fig. 2.7 represents a quantum efficiency curve for an ideal solar cell. Although the ideal form of quantum efficiency is square, recombination factors cause most solar cells quantum efficiency to be lower. For real solar cell structures, the QE might be reduced by surface recombination at short wavelengths and bulk recombination at long wavelengths. The external quantum efficiency (EQE) of a solar cell includes the effects of transmission and reflection. The internal quantum efficiency (IQE) can be determined from the external quantum efficiency by measuring the transmission and reflection [55].

J-V Curve

The J-V curve of a solar cell is, perhaps the most important piece of information in characterizing solar cells. The short-circuit current density (J_{sc}), the open-circuit voltage (V_{oc}), the fill factor (FF) and the efficiency (η) can be determined from the J-V curve. It

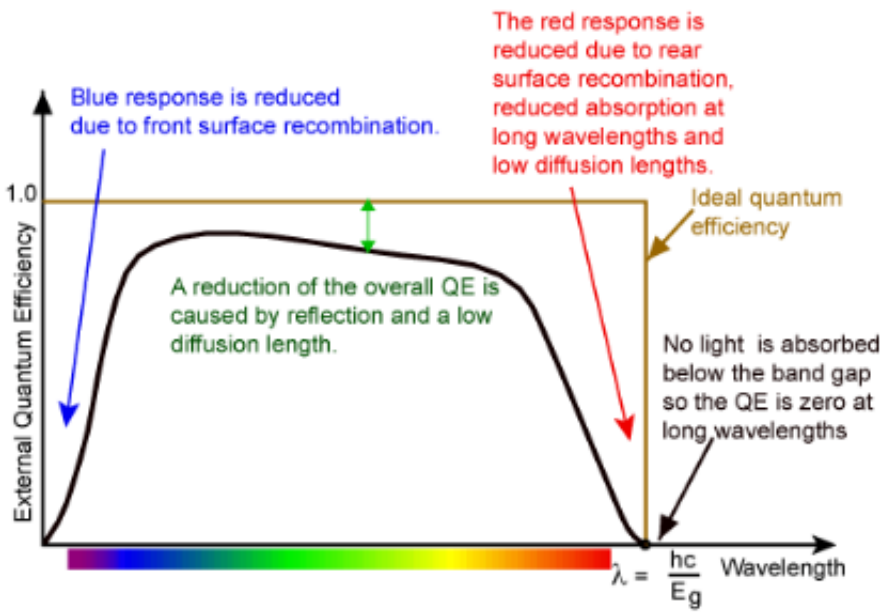

Figure 2.7: Quantum efficiency of an ideal solar cell and a practical solar cell. Reproduced from Ref. [55].

is the convention to invert the current density axis of the J-V curve, bringing it into the first quadrant as shown in Fig. 2.8.

Short Circuit Current Density

The short-circuit current density J_{sc} is the maximum current that can be drawn from a solar cell and it is achieved at zero voltage. For an ideal solar cell, $J_{sc} = J_L$. The short-circuit current density J_{sc} depends on the QE and the intensity and spectrum of the incident light. This dependence is interpreted as [56]

$$J_L = q \int_0^\infty \phi_0(\lambda) QE(\lambda) d\lambda, \tag{2.6.3}$$

where $\phi_0(\lambda)$ is the photon flux ($m^{-2}s^{-1}nm^{-1}$)

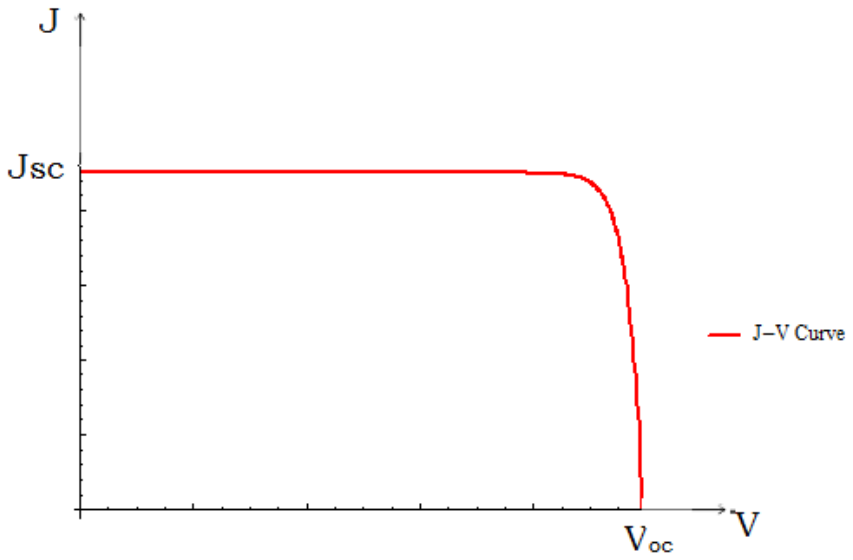

Figure 2.8: J-V curve of a solar cell, showing the short-circuit current density (J_{sc}) and the open-circuit voltage (V_{oc}).

Open Circuit Voltage

The open-circuit voltage (V_{oc}) is the maximum voltage available from a solar cell and it is achieved at zero current. V_{oc} depends on J_{sc} and J_o . J_{sc} typically has small variation whereas J_o may vary by orders of magnitude. Since J_o depends on recombination, V_{oc} can be seen as a measure of the recombination in the solar cell. The V_{oc} is given by [55]

$$V_{oc} = \frac{nK_BT}{q} ln\left(\frac{J_{sc}}{J_o} + 1\right). \tag{2.6.4}$$

Fill Factor

The fill factor (FF) is the ratio of the maximum power that can be extracted from a solar cell to the product of the J_{sc} and V_{oc} as shown by [55]

$$FF = \frac{P_m}{J_{sc}V_{oc}} = \frac{J_mV_m}{J_{sc}V_{oc}}, \tag{2.6.5}$$

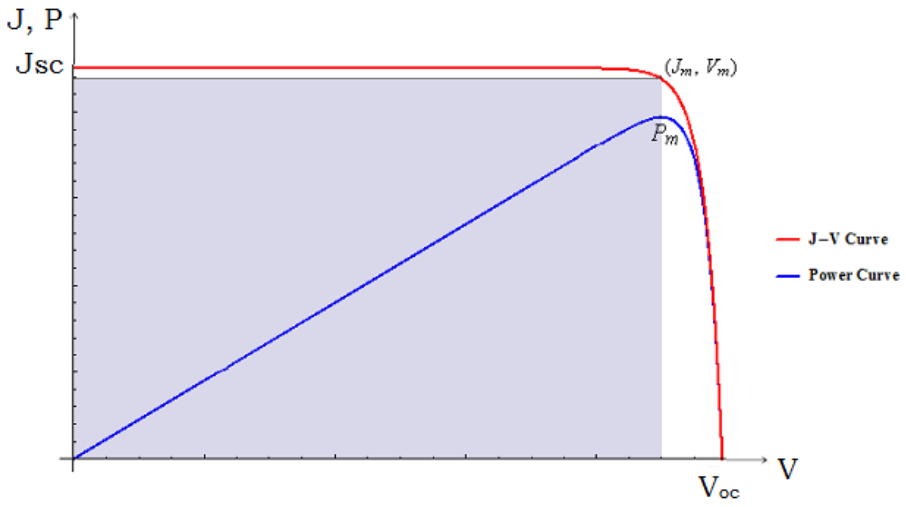

Figure 2.9: J-V curve showing the maximum power point.

where J_m and V_m refer to the current density and the voltage at the maximum power point. The fill factor is a measure of the p-n junction quality and series resistance of a solar cell. The maximum power point is also an important parameter and it is graphically represented in Fig. 2.9. The maximum power density (P_m) that can be extracted from a solar cell can then be calculated by

$$P_m = J_m V_m = J_{sc} V_{oc} FF. \tag{2.6.6}$$

Efficiency

Efficiency (η) is defined as the ratio of energy output from a solar cell to the input incident solar energy. It is perhaps the most commonly used parameter for a solar cell. Measurements of efficiency for terrestrial cells are usually done with the $AM1.5$ Global solar spectrum at 25 ^0C. The efficiency can be described as [55]

$$\eta = \frac{P_m}{P_{in}} = \frac{J_{sc} V_{oc} FF}{P_{in}}, \tag{2.6.7}$$

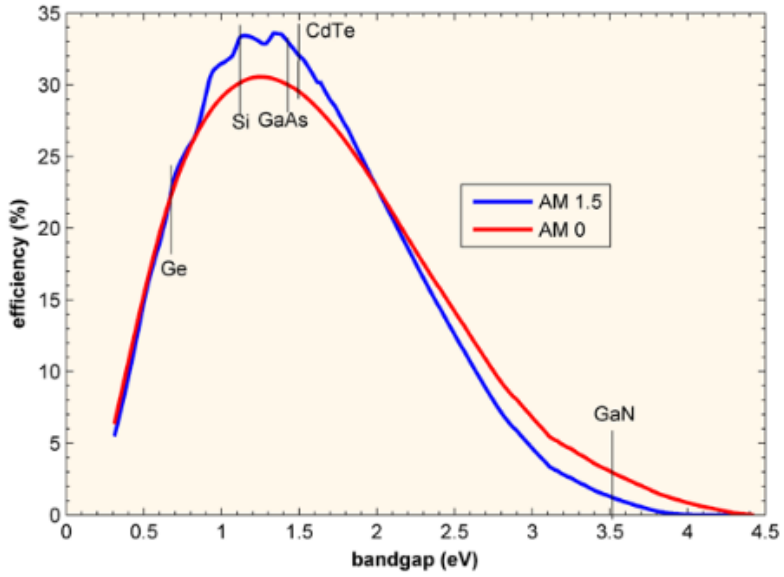

Figure 2.10: Limiting efficiency for single bandgap solar cells as a function of bandgap under the $AM0$ and $AM1.5$ global spectrum. Reproduced from Ref. [55].

where P_{in} is the input power density which is 1000 Wm^{-2} for the $AM1.5$ Global spectrum. The limiting efficiency of singe bandgap cells as a function of bandgap for the $AM0$ and $AM1.5$ Global spectrum is shown in Fig. 2.10 with some semiconductor materials highlighted. The maximum efficiency occurs at about 1.37 eV which is close to the bandgap of GaAs (1.43 eV).

2.7 n-p Junction Solar Cell Under Illumination

Figure 2.11 illustrates the n-p junction under illumination. The quasi-neutral region of the n-type, extending from the exposed surface at $x = 0$ to the edge of the depletion region at $x = x_n - W_n$ and the quasi-neutral region of the p-type, extending from the edge of depletion region at $x = x_n + W_p$ to the back surface at $x = x_n + x_p$. W_n and W_p are the depletion width in the n- and p-regions, respectively.

In the case of an abrupt n-p junction (Fig. 2.11) with uniform doping on both sides, no electric fields exist beyond the depletion region. Photogenerated carriers in these regions

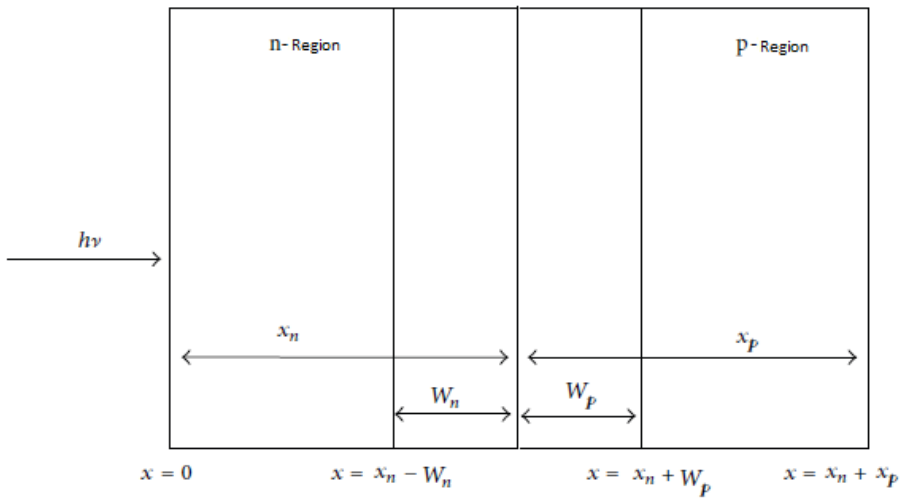

Figure 2.11: n-p junction under illumination

are collected by a diffusion process while that in the depletion region by drift process. Three regions comprise the collection of photogenerated carriers: the top neutral region, the depletion region, and the substrate neutral region.

2.7.1 Emitter Photocurrent Density

We concentrate on the diffusion of minority carrier holes in order to construct an expression for the component of the photocurrent that results from the generation in the emitter quasi-neutral region. Under a low-injection and steady-state conditions, the one-dimensional continuity equation for the minority carrier holes in the emitter (n-type layer) is calculated by combining Eqns. (2.3.2) and (2.3.4). The result is given as

$$G_p - \left(\frac{p_n - p_{no}}{\tau_p}\right) - \frac{1}{q}\frac{dJ_p}{dx} = 0. \tag{2.7.1}$$

Assuming that there is no electric field outside of the depletion region, the photocurrent in the n-side is thus solely contributed by diffusion current. Equation (2.2.9) is therefore simplified to

$$J_p = -qD_p\left(\frac{dp_n}{dx}\right). \tag{2.7.2}$$

For the top n-side of the junction, Eqns. (2.4.1), (2.7.1), and (2.7.2) can be combined to yield an expression:

$$D_p \frac{d^2 p_n}{dx^2} + \alpha\phi_0[1-R]\exp[-\alpha x] - \left(\frac{p_n - p_{no}}{\tau_p}\right) = 0. \tag{2.7.3}$$

The general solution to Eqn. (2.7.3) is

$$p_n - p_{no} = A\cosh[\frac{x}{L_p}] + B\sinh[\frac{x}{L_p}] - \frac{\alpha\phi_0[1-R]\tau_p}{\alpha^2 L_p^2 - 1}\exp[-\alpha x], \tag{2.7.4}$$

where $L_p = \sqrt{D_p\tau_p}$ is the diffusion length, A and B are constants. The constants A and B in Eqn. (2.7.4) are obtained by applying the following two boundary conditions (Eqns. (2.7.5) and (2.7.6)) [56].

1. Surface recombination with a recombination velocity of S_p occurs at the surface:

$$D_p \frac{d(p_n - p_{no})}{dx} = S_p(p_n - p_{no}) \qquad at \quad x = 0. \tag{2.7.5}$$

2. The electric field in the depletion region causes the excess carrier density to be small at the depletion edge:

$$p_n - p_{no} = 0 \qquad at \quad x = x_n - W_n. \tag{2.7.6}$$

The hole density is computed by using these boundary conditions in Eqn. (2.7.4). Equation (2.7.2) is utilised to compute the hole photocurrent density as a function of photon energy at the depletion edge of the n-emitter region ($x = x_n - W_n$). The result is as follows

$$J_p(E) = \left[\frac{q\phi(E)[1-R(E)]a_p}{a_p^2 - 1}\right]\left[\frac{(b_p + a_p) - \beta_1^p\exp[-\alpha x_j]}{\beta_2^p} - a_p\exp[-\alpha x_j]\right], \tag{2.7.7}$$

where q is the absolute value of the electronic charge, $a_p = \alpha L_p$, $b_p = \frac{S_p L_p}{D_p}$, $\beta_1^p = b_p \cosh[\frac{x_j}{L_p}] + \sinh[\frac{x_j}{L_p}]$, $\beta_2^p = b_p \sinh[\frac{x_j}{L_p}] + \cosh[\frac{x_j}{L_p}]$, $L_p = \sqrt{D_p \tau_p}$ is diffusion length of holes, S_p is surface recombination velocity of holes, D_p is diffusion constant of holes, τ_p is minority carrier life time of holes, and $x_j = x_n - W_n$ is the quasi-neutral width of n-region. The total hole photocurrent collected from the n-region is equal to

$$J_p^n = \int_{E_g}^{\infty} J_p(E) dE. \tag{2.7.8}$$

2.7.2 Base Photocurrent Density

A similar method to that outlined for the hole current in the emitter can be used to calculate the photocurrent resulting from the minority carrier electrons generated in the base. The one-dimensional continuity equation minority carrier electrons in the base (p-type layer) under low-injection and steady-state conditions is obtained by combining Eqns. (2.3.1) and (2.3.3), and it is presented as

$$G_n - \left(\frac{n_p - n_{po}}{\tau_n} \right) - \frac{1}{q} \frac{dJ_n}{dx} = 0. \tag{2.7.9}$$

Assuming that there is no electric filed outside of the depletion region. As a result, the photocurrent in the p-side is only contributed by the diffusion current. Consequently, Eqn. (2.2.8) is simplified to

$$J_n = q D_n \left(\frac{dn_p}{dx} \right) \tag{2.7.10}$$

For the bottom p-side of the junction, Eqns. (2.4.1), (2.7.9), and (2.7.10) can be combined to yield an expression:

$$D_n \frac{d^2 n_p}{dx^2} + \alpha \phi_0 [1 - R] \exp[-\alpha x] - \left(\frac{n_p - n_{po}}{\tau_n} \right) = 0. \tag{2.7.11}$$

The general solution to this equation is

$$n_p - n_{po} = C\cosh[\frac{x}{L_n}] + D\sinh[\frac{x}{L_n}] - \frac{\alpha\phi_0[1-R]\tau_n}{\alpha^2 L_n^2 - 1}\exp[-\alpha x], \tag{2.7.12}$$

where $L_n = \sqrt{D_n\tau_n}$ is the diffusion length of electrons, C and D are constants. The constants C and D are calculated by applying the following two boundary conditions (Eqns. (2.7.13) and (2.7.14)) [56].

1. Surface recombination occurs at the surface, with a recombination velocity of S_n:

$$-D_n\frac{d(n_p - n_{po})}{dx} = S_n(n_p - n_{po}) \qquad at \quad x = x_n + x_p. \tag{2.7.13}$$

2. The excess carrier density near the depletion edge is low due to the electric field in the depletion region:

$$n_p - n_{po} = 0 \qquad at \quad x = x_n + W_p. \tag{2.7.14}$$

The electron density is computed using these boundary conditions in Eqn. (2.7.12). Equation (2.7.10) is used to compute the electron photocurrent density that is collected at the depletion edge of the p-base region ($x = x_n + W_p$) as a function of photon energy. The result is given as

$$J_n(E) = \left[\frac{q\phi(E)[1-R(E)]a_n}{a_n^2 - 1}\right]\exp\big(-\alpha[x_j + W]\big)\left[a_n - \frac{\beta_1^n + (a_n - b_n)\exp(-\alpha H')}{\beta_2^n}\right], \tag{2.7.15}$$

where $a_n = \alpha L_n$, $b_n = \frac{S_n L_n}{D_n}$, $\beta_1^n = b_n\cosh[\frac{H'}{L_n}] + \sinh[\frac{H'}{L_n}]$, $\beta_2^n = b_n\sinh[\frac{H'}{L_n}] + \cosh[\frac{H'}{L_n}]$, $L_n = \sqrt{D_n\tau_n}$ is diffusion length of electrons, S_n is surface recombination velocity for electrons, D_n is diffusion constant of electrons, τ_n is minority carrier life time of electrons, $W = W_n + W_p$ is the width of the space-charge region and $H' = x_p - W_p$ is the quasi-neutral width of p-region.

The total electron photocurrent collected from the p-region is equal to

$$J_n^p = \int_{E_g}^{\infty} J_n(E)dE. \tag{2.7.16}$$

2.7.3 Depletion Region Photocurrent Density

It is reasonable to suppose that the built-in field separates all carriers generated in the space-charge layer. Therefore, we can take into account either electrons or holes when determining the current resulting from photogeneration in this region. We can suppose that the carriers are swept out of the space-charge region so quickly that there is no chance for recombination to occur, which makes the derivation considerably simpler than for the photocurrents in the quasi-neutral regions. Consequently, using electrons for our derivation

$$G_D - \frac{1}{q}\frac{dj_D}{dx} = 0. \tag{2.7.17}$$

The generation rate in the space-charge region is written by taking in to account the attenuation of light in the n-region

$$G_D(E,x) = \alpha\phi_0[1-R]\exp[-\alpha x_j]\exp[-\alpha(x-x_j)]. \tag{2.7.18}$$

The photocurrent generated inside the space-charge region as a function of photon energy is calculated using Eqn. (2.7.17) and it is given by

$$j_D(E) = q\int_{x_j}^{x_j+W} G_D(E,x)dx. \tag{2.7.19}$$

Evaluating Eqn. (2.7.19) gives

$$j_D(E) = q\phi_0[1-R]\exp[-\alpha x_j]\big[1-\exp[-\alpha W]\big], \tag{2.7.20}$$

The total photocurrent can be harvested from the space-charge region is

$$J_D = \int_{E_g}^{\infty} j_D(E) dE. \tag{2.7.21}$$

2.8 n–p Junction Solar Cell in the Dark

2.8.1 Recombination Current Densities in the Quasi Neutral Regions

A forward bias causes the built-in potential barrier of the junction to decrease and more majority carriers to diffuse across the junction in the dark. This results in a net flow of electrons from n to p and holes from p to n. This process is occasionally denoted as the majority carrier injection. Because the quasi Fermi levels in the space-charge region (SCR) are split by the applied bias, there is net recombination in that region which adds to the current. Under these circumstances, Eqn. (2.7.3) is modified to

$$D_p \frac{d^2 p_n}{dx^2} = \left(\frac{p_n - p_{no}}{\tau_p} \right). \tag{2.8.1}$$

and Eqn. (2.7.11) is reduced to

$$D_n \frac{d^2 n_p}{dx^2} = \left(\frac{n_p - n_{po}}{\tau_n} \right). \tag{2.8.2}$$

Equation (2.8.1) can be solved using the following boundary conditions (Eqns. (2.8.3) and (2.8.4))

$$p_n - p_{no} = \frac{n_i^2}{N_D} \left(\exp \left[\frac{qV}{K_B T} \right] - 1 \right) \qquad at \;\; x = x_n - W_n, \tag{2.8.3}$$

$$p_n - p_{no} = 0 \qquad at \;\; x = -\infty. \tag{2.8.4}$$

Similarlly, Equation (2.8.2) can be solved by applying the following boundary conditions (Eqns. (2.8.5) and (2.8.6))

$$n_p - n_{po} = \frac{n_i^2}{N_A}\left(\exp\left[\frac{qV}{K_B T}\right] - 1\right) \qquad at \;\; x = x_n + W_p, \tag{2.8.5}$$

$$n_p - n_{po} = 0 \qquad at \;\; x = \infty. \tag{2.8.6}$$

The recombination current density component due to the diffusion of minority carriers holes in the n-region is calculated by

$$J_{p,dark}^{diff} = -qD_p\left(\frac{d(p_n - p_{no})}{dx}\right). \tag{2.8.7}$$

Minority carriers hole recombination current density at $x = x_n - W_n$ is calculated as

$$J_{p,dark}^{diff} = \frac{qn_i^2 D_p}{L_p N_D}\left(\exp\left[\frac{qV}{K_B T}\right] - 1\right). \tag{2.8.8}$$

The recombination current density component due to the diffusion of minority carriers electrons in the p-region is calculated by

$$J_{n,dark}^{diff} = qD_n\left(\frac{d(n_p - n_{po})}{dx}\right). \tag{2.8.9}$$

Minority carriers electron recombination current density at $x = x_n + W_p$ is calculated as

$$J_{n,dark}^{diff} = \frac{qn_i^2 D_n}{L_n N_A}\left(\exp\left[\frac{qV}{K_B T}\right] - 1\right). \tag{2.8.10}$$

The total recombination current density due to diffusion of minority carriers in the n- and p-regions is given by

$$J_{dark}^{diff} = J_{01}\left(\exp\left[\frac{qV}{K_B T}\right] - 1\right), \tag{2.8.11}$$

where J_{01} is the reverse saturated current due to diffusion of minority carriers and it is given by

$$J_{01} = qn_i^2\left(\frac{D_p}{L_pN_D} + \frac{D_n}{L_nN_A}\right). \tag{2.8.12}$$

2.8.2 Recombination Current Density Within the Depleted Region

If the dominant recombination process is Shockley Read Hall (SRH) recombination through trap states then, we use

$$J_{dark}^{rec} = \int_{x_n-W_n}^{x_n+W_p} \frac{np - n_i^2}{\tau_n(p+p_t) + \tau_p(n+n_t)}dx, \tag{2.8.13}$$

where n_t is the value of the electron density when the electron Fermi level is equal to the trap level, and p_t is the value of the hole density when the hole Fermi level is equal to the trap level.

The recombination current density from the depletion region given by Eqn. (2.8.13) has the approximate form [47]

$$J_{dark}^{rec} = J_{02}\left(\exp\left[\frac{qV}{2K_BT}\right] - 1\right), \tag{2.8.14}$$

where J_{02} is the reverse saturated current due to SRH recombination and it is given by

$$J_{02} = \frac{qn_i(W_n + W_p)}{\sqrt{\tau_n\tau_p}}. \tag{2.8.15}$$

2.8.3 Total Recombination Current Density

The total recombination current density is defined as

$$J_{dark} = J_{dark}^{diff} + J_{dark}^{rec} \tag{2.8.16}$$

$$J_{dark} = J_{01}\left(\exp\left[\frac{qV}{K_BT}\right] - 1\right) + J_{02}\left(\exp\left[\frac{qV}{2K_BT}\right] - 1\right). \tag{2.8.17}$$

In indirect gap materials like silicon, diffusion lengths are long compared to the depletion width and very little recombination occurs in the depleted region, so J_{dark}^{rec} can be ignored. In that case we have

$$J_{dark} \approx J_{01}\left(\exp\left[\frac{qV}{K_BT}\right] - 1\right). \tag{2.8.18}$$

This is the Shockley or 'ideal' diode equation and is often quoted for the dark current of a solar cell.

In direct band gap materials where absorption is strong or where the SCR is wide, recombination within the depleted region may be dominant. Then

$$J_{dark} \approx J_{02}\left(\exp\left[\frac{qV}{2K_BT}\right] - 1\right). \tag{2.8.19}$$

If more than one process is important then J_{dark} may appear to vary like

$$J_{dark} \approx J_{0}\left(\exp\left[\frac{qV}{mK_BT}\right] - 1\right), \tag{2.8.20}$$

where J_0 is a constant and m is the ideality factor. An ideal diode has $m = 1$. In real cells we often see a change in slope from J_{dark}^{rec} dominating at low bias ($m = 2$), to J_{dark}^{diff} at high bias ($m = 1$).

2.9 Intermediate Band Solar Cells

The basic structure of an IB solar cell comprises an IB material inserted between p- and n-type conventional semiconductors [57]. The IB splits the overall bandgap E_g into two sub-bandgaps, E_L and E_H. The lowest energy level, E_L, is often the one dividing the IB from the CB (inset in Fig. 2.12). Through more efficient use of the solar spectrum, the intermediate band solar cell (IBSC) can surpass the Shockley-Quiesser efficiency limit of

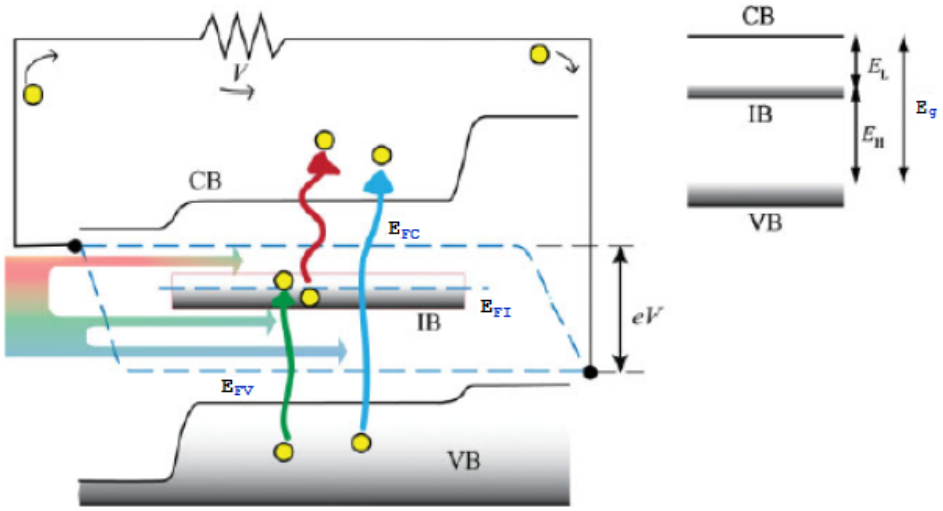

Figure 2.12: Photon absorption process and quasi-Fermi level split in an IB solar cell. Reproduced from Ref. [57].

30% for a single junction solar cell [58]. As was previously noted, sub-bandgap photon losses are one of the main losses in single bandgap solar cells. In order to increase the efficiency of solar cells, it is imperative to capture the low energy infrared portion of the solar spectrum, which makes up a significant portion of the spectrum.

The IBSC idea is depicted in Fig. 2.12. Sub-bandgap photon absorption is made possible by the intermediate band (IB) within the semiconductor bandgap. Apart from the standard photon absorption process involving electron transitions between the VB and CB, there exists another photon absorption process that involves transitions between the VB and IB, followed by the IB and CB. Each band has a distinct quasi-Fermi level because carrier relaxation between bands occurs much slower than carrier relaxation within bands: E_{FC}, E_{FV}, and E_{FI} (dashed blue lines in Fig. 2.12) [57]. The additional photon absorptions should increase the photocurrent without lowering the output voltage in order to achieve the efficiency improvement predicted by the IBSC concept. This requires distinct quasi-Fermi levels for each of the energy bands. The quasi-Fermi levels for electrons (E_{FC}) in the CB and holes (E_{FV}) in the VB, divided by the electron charge, yield the voltage obtained from the IBSC.

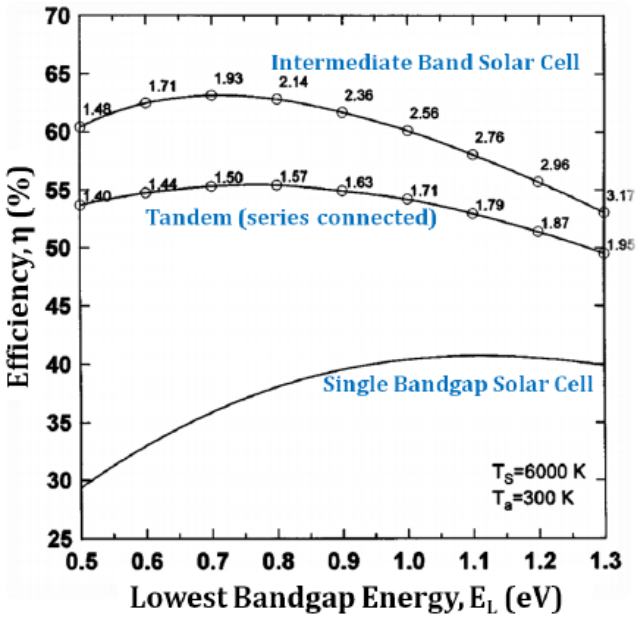

Figure 2.13: Limiting efficiency for an intermediate band solar cells and a double junction tandem solar cell as a function of the lowest bandgap energy. The limiting efficiency of a single bandgap solar cell is also included for comparison. The numbers on the plot represent the highest bandgap in the intermediate band and tandem cells. Reproduced from Ref. [22].

Figure 2.13 illustrates the calculated limiting efficiency as a function of the lowest bandgap for an IBSC and a two-terminal tandem solar cell [22]. In comparison to a two junction tandem cell and a single bandgap cell, the IBSC was found to have a full concentration blackbody spectrum limiting efficiency of 63%. The best bandgaps for an IBSC to be implemented are $E_{CV} = 1.93\ eV$, $E_{VI} = 1.23\ eV$, and $E_{IC} = 0.7\ eV$, as can be seen in Fig. 2.13. These calculations are predicated on the suppression of non-radiative recombination, the absence of ohmic losses, the cells temperature of 300 K, and the illumination provided by an isotropic photon gas at 6000 K.

2.10 Quantum Dot Intermediate Band Solar Cells

For the purpose of implementing the IBSC, several IB materials have been suggested. These include $Ti_xGa_{1-x}P$ [59], Cr-doped II-VI compounds [60], and transition meta-doped chalcopyrite-type semiconductors [61]. To our knowledge, the first bulk IB solar cell was made utilising $ZnTe$ doped with oxygen impurities in order to form the IB [62, 63]. Despite having a lower output voltage than the reference cell, the cell produces a higher current and has a higher efficiency. The quantum efficiency of the oxygen-doped cell clearly demonstrates sub-bandgap absorption.

On the other hand, it was proposed that nanotechnology be used to build the required IB [26]. Quantum dots (QDs) are nanoscale semiconductor material clusters that confine carriers in three dimensions. Due to the complete size quantization of electronic levels in the QDs [64], which results in a density of states like a delta function. QDs achieve three-dimensional potential wells that ideally isolate the IB from the CB, making them essential (or at least preferred) for IB solar cells over other low-dimensional structures like quantum wells or wires [26, 57]. To facilitate the creation of distinct quasi- Fermi levels, these discrete density of states have the ability to produce a zero density of states between the IB and the CB [65]. In particular, as shown in Fig. 2.14, narrowly spaced quantum dot arrays

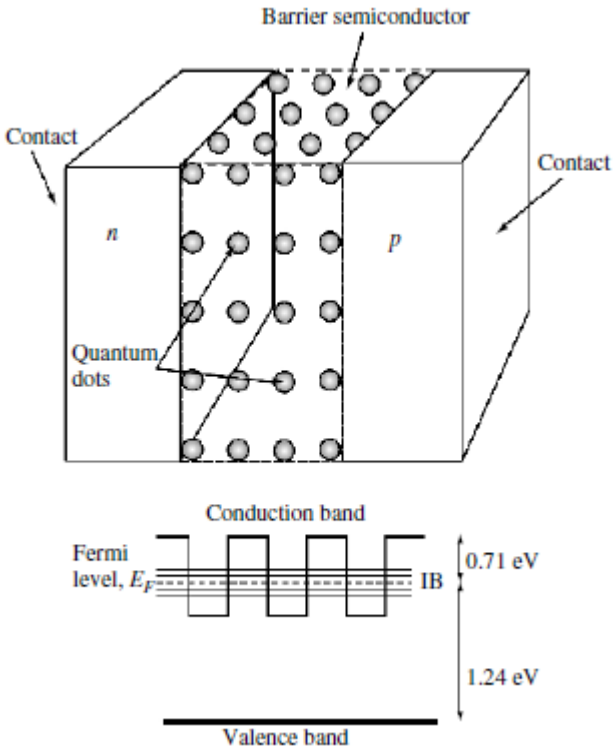

Figure 2.14: IB formation in QD arrays. Reproduced from Ref. [26].

may generate the necessary band [26]. Typically, the QDs are positioned in the intrinsic region of a p-i-n solar cell structure and embedded in a barrier material with a larger bandgap. The confined electron levels within the potential well established as a result of the conduction band offset between the barrier and the dots create the intermediate states in QD IBSCs. Figure 2.14 gives an illustration of this. Material systems including GaSb/GaAs [66], In(Ga)As/GaAs [33, 34, 35, 67, 68], and InAs/GaNAs [69] have provided evidence for the fundamental concepts of QD IBSC. Numerous experimental findings [33, 34, 35, 36, 37, 38, 39, 40, 41, 42] of QDSC demonstrate that there is a loss in open circuit voltage and conversion efficiency but an increase in short circuit current density when compared to reference cells. Few QDSC experimental findings [70, 71] demonstrate an improvement in short circuit current density and conversion efficiency despite a drop in open circuit voltage, in contrast to reference cells.

2.10.1 Evidence for the Concept of Intermediate Band Solar Cell Using Quantum Dots

Adequate experimental evidence has already been shown for sub-bandgap photocurrent in IBSCs. The QE measurements for an InAs QD IBSC and a single junction GaAs cell are presented in Fig. 2.15. As can be indicated photons are absorbed by the IBSC below the GaAs bandgap, but the reference cell only absorbs above the GaAs bandgap. It has been demonstrated that the sub-bandgap photon absorption in the present InAs/GaAs QD IBSCs is mostly caused by photon excitation of electrons from the VB to the IB. Thermal escape and tunnelling mechanisms cause the IB-CB transition [72]. This cannot result in the great efficiency anticipated since it is incompatible with the IBSC model. It takes a second sub-bandgap photon transition to supply the energy needed to maintain the output voltage. It has been shown that there are two sub-bandgap photon transitions (VB-IB and IB-CB) in an IBSC at 6K [73]. The purpose of the low temperature is to reduce thermal escape. Although two-photon absorption was initially only seen at low temperatures for the majority of QD IBSC, a recent work has shown evidence of two-photon absorption for an InAs/GaNAs QD IBSC at room temperature [74]. These promising results were obtained by direct Si-doping of the QDs in the QDSC structure rather than δ-doping the inter-dot layer.

2.10.2 InAs/GaAs QD Solar Cells

The InAs/GaAs QD material system has been used extensively as a test subject to validate the QD IBSC's operating principles. The InAs/GaAs QD material system has been employed mostly because it is relatively well known, rather than because it has the optimum band alignments for an intermediate band solar cell. Having stated that, knowledge gained from this material system can be transferred to other situations.

Even though these solar cells don't have ideal bandgaps, simulations indicate that high

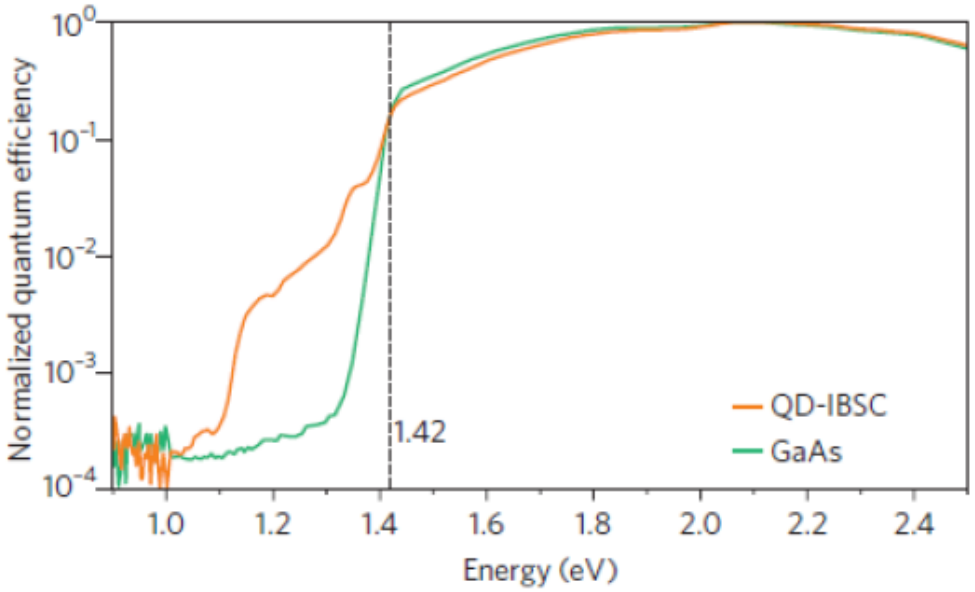

Figure 2.15: Comparison of the normalised quantum efficiency of a GaAs solar cell and a QD IBSC. Reproduced from Ref. [75].

illumination concentration produces efficiencies higher than single junction solar cells. This is because, in contrast to the CB-VB transition, recombination increases more slowly across the IB [75]. The sizes, shape, and composition of the quantum dots materials will determine the intermediate band position. The size distribution of the QD and the separation between dot layers determine the width of the IB [76]. These solar cell architectures frequently exhibit two narrowly separated peaks in their photoluminescence, one of which corresponds to the VB-IB transition and the other to the VB-CB transition. The absence of a third peak indicates that the second sub-bandgap transition (IB-CB) is not occurring optically, as would be predicted from the luminescence signature of intermediate band materials. In an InAs/GaAs material system, the wetting layer beneath the QDs causes the formation of an energy level below the CB, which forms a continuum with it and reduces the solar cell's effective bandgap. A quasi-continuum of states is formed in the VB by closely spaced confined levels because the effective mass of holes is larger than that of electrons [76]. The total bandgap of the InAs/GaAs solar cell is limited to roughly 1.3 eV

by this VB offset in addition to the gap shrinkage in the CB due to the wetting layer [75]. The energy differential between the IB and the CB, which in this instance is around $\sim$ 0.3 eV [77], then becomes another issue. Because of the small energy gap, electrons can easily thermalize into the CB rather than being drawn there by photons.

2.11 Multi-Junction Solar Cells

The most efficient solar cells available right now are multi-junction solar cells (MJSC), sometimes known as tandem cells [78]. Over a 30-year period, monolithic III-V MJ cells (for concentrator cells and modules) have shown impressive growth, with efficiency increasing from 31.8% to 47.6% [79]. Since concentrators make MJSCs more affordable, they have gained acceptability for usage in terrestrial applications despite their original development for space purposes [80]. Their exceptional efficiency can be attributed to a particular design that enables the solar cell to selectively absorb light from various wavelengths of the sun. A MJSC is made up of series-connected p-n junction solar cells, with the greatest bandgap solar cell positioned at the top and the smallest at the bottom. A tunnel junction connects the different cells, as seen in Fig. 2.16(b). To achieve high efficiency in the MJSC, bandgaps must be distributed and allocated effectively. Different III-V compound semiconductors can be alloyed to provide a wide range of bandgaps (Fig. 2.16(a)). It's critical to make sure extra current isn't squandered because the MJSC's lowest current-producing cell sets the overall cell's current. The hunt is on to discover a 1.0 eV bandgap material, such as InGaP/GaAs/Ge, that may be placed in the current limiting region of a MJSC in order to increase efficiency and short circuit current. Detailed balance calculations have demonstrated that spectral adjustment of MJSC via quantum dots may result in higher efficiency [81].

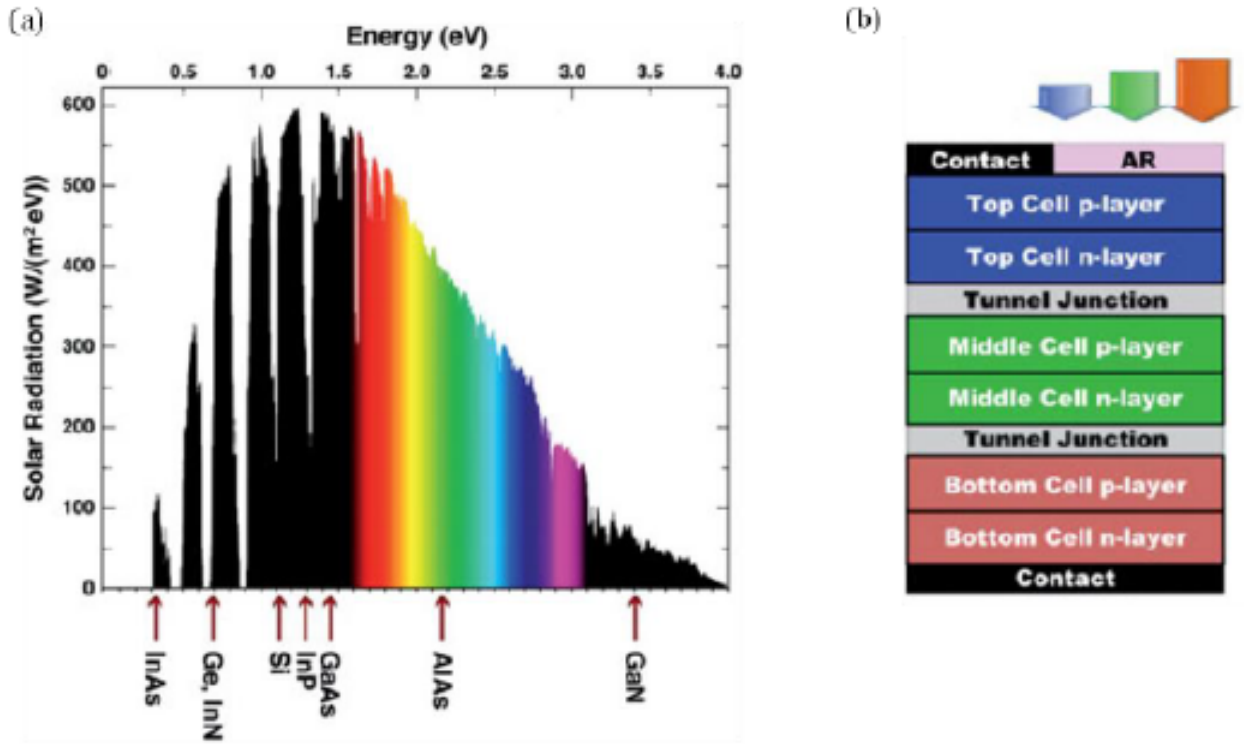

Figure 2.16: (a) Bandgaps of semiconductors shown on the AM1.5 spectrum and (b) a schematic of the multi-junction solar cell structure. Reproduced from Ref. [82].

Chapter 3

Theoretical Modelling of Quantum Dot Solar Cells

3.1 Introduction

Intermediate band and multi-junction solar cells approaches are the simplest and most effective methods for increasing the photo-generated current density and efficiency of solar cells by absorbing low-energy photons. Quantum dots, which are low-dimensional semiconductors, have been suggested as an intermediate band to ensure that the intermediate solar cell technique operates properly. Using the well-known stacking technique in the Stranski–Krastanow growth mode [83], a high-density array of QDs can be produced. The vertical alignment of QDs is typically caused by the strain fields of the lower QDs layer extended into the barrier material. Electronic states can take on a wire-like character because of the strong vertical coupling between QDs [84]. Consequently, channelling the electrons and holes through the coupling between aligned QDs can result in high internal quantum efficiency for the collection of carriers photoexcited in the QDs. This phenomenon makes it possible to effectively separate and inject the electrons and holes generated by QDs into nearby p and n regions. Section 3.2 describes the model of

$InAs/GaAs$ QDSC and methods used to investigate the dependency of QDSC parameters on the number of QD layers, size, and size dispersion of QDs. Section 3.3 discusses the model of $Ga_{0.51}In_{0.49}P/GaAs/Ge$ triple junction quantum dot solar cell and methods used to investigate the impact of inserting $InAs$ QD in the middle subcell.

3.2 $InAs/GaAs$ Quantum Dot Solar Cell

A theoretical model of an $InAs/GaAs$ quantum dot solar cell is designed by embedding $InAs$ quantum dot multi-layers in the intrinsic region of the $n^+ - i - p^+$ $GaAs$ structure. This theoretical model include realistic estimates for the light absorption, photocurrent generation in p- and n-type $GaAs$ regions and $InAs/GaAs$ QDs i-region, as well as the surface and bulk minority-carrier recombination and junction generation-recombination currents. For an abrupt junction with uniform doping on both sides, no electric fields exist beyond the i-region. Photogenerated carriers in the n- and p-regions are collected through diffusion, whereas those in the i-region are collected via drift. We use the diffusion of minority carrier holes and electrons to calculate the photocurrent generated in the n- and p-regions. The photogenerated carriers in the i-region are a combination of those from the $GaAs$ barrier and $InAs$ quantum dots. To calculate photocurrent generated and collected by barrier $GaAs$ and $InAs$ QDs, a strong electric field in the i-region is assumed. Therefore, photogenerated carriers are swiftly swept out of the i-region, preventing recombination from occurring. The dark current density is calculated using minority carrier diffusion at the depletion layer borders and thermal emission within the i-region.

Numerical simulations are utilised to investigate the dependency of $InAs/GaAs$ QDSC parameters on the number of QD layers, as well as the impact of cubic and spherical $InAs$ QD size and size dispersion on the absorption coefficient, photocurrent, and power conversion efficiency of the $InAs/GaAs$ QDSC.

3.3 $Ga_{0.51}In_{0.49}P/GaAs/Ge$ Triple Junction Quantum Dot Solar Cell

This dissertation's theoretical model of a triple-junction quantum dot solar cell includes n/p $Ga_{0.51}In_{0.49}P$ as the top subcell, $n^+ - i - p^+$ $GaAs$ with $InAs$ QDs in the i-region as the middle subcell, and n/p Ge as the bottom subcell. The photocurrent and dark current densities for each subcell are computed analytically. The drift-diffusion process yields an equation for the photocurrent densities generated and collected in the top and bottom subcells. The dark current density for the top and bottom subcells are calculated based on minority carrier diffusion at the depletion layer margins and depletion-region recombination current density (SRH recombination). The photocurrent and dark current densities for the middle subcell ($InAs/GaAs$ QDSC) are identical to those described in Section 3.2.

The current density of a triple-junction quantum dot solar cell is calculated numerically utilising the current densities of its three subcells. The open circuit voltage of a triple-junction quantum dot solar cell is the sum of the open circuit voltages of each subcell, while the short circuit current density is the lowest of the subcells. To accomplish current matching among the three subcells, doping concentration, subcell thickness, and $InAs$ QD size are numerically simulated. The influence of introducing an $InAs$ quantum dot in the middle subcell of a triple junction $Ga_{0.51}In_{0.49}P/GaAs/Ge$ solar cell is investigated using numerical simulations of the J-V curve.

Chapter 4

Dependence of Quantum Dot Solar Cell Parameters on the Number of Quantum Dot Layers

4.1 Introduction

The sun energy is one of the most promising renewable energy sources [12]. A solar cell can convert the sun energy into electrical energy. Conventional solar cells have a big loss of energy because of the spectral mismatch between the bandgap of a semiconductor material and the energy distribution of photons in the solar spectrum [32]. Photons with energies lower than the energy bandgap of absorber material are not absorbed and cannot generate electron-hole pairs [12]. This loss of energy caused by spectral mismatch can be minimized by using the intermediate band solar cell (IBSC) concept [22]. The idea of IBSC photovoltaic is exciting electrons by two-step over a semiconductor band gap with the help of intermediate band [23]. Using low-energy photons with the concept of the intermediate band method enhances the maximum detailed balance efficiency from 40.7% to 63.1% [22]. To obtain the operating principles of IBSC, a confined levels of quantum dot (QD) was proposed [26, 27]. The proof of obtaining three distinct quasi-Fermi levels [28, 29] and the generation of photocurrent by absorption of photons laying under the semiconductor band gap [26, 28, 29, 30], which are the pillars of IBSC principles, has attracted the interest of many researchers in the field of quantum dot solar cells (QDSC).

Previous experimental reports [85] on quantum well solar cells revealed that embedding up to 50 layers of $InGaAs$ quantum wells in the i-region of a p-i-n GaAs cell structure increases photocurrent and cell efficiency but decreases the open circuit voltage. However, in [86] it was reported that increasing the number of wells from 50 to 65 leads in a drop in cell efficiency. Another experimental report [66] revealed that the inclusion of 10 stacks of $GaSb$ QDs in the i-region of $GaAs$-based solar cells significantly improves the spectral response. This cell has a higher short circuit current and a lower open circuit voltage than the cell without QDs. Abiseka [87] experimentally showed the influence of the thickness of the absorber layer on the efficiency of PbS QD solar cell. It was found that a device with absorber layers 240 nm thick performed the best, with increasing thickness leading to a reduction in efficiency. Takeyoshi [36] also reported that increasing the number of stacked layers to 150 increases the external quantum efficiency and short circuit current density of multi-stacked $In_{0.4}Ga_{0.6}As$ QD solar cells. Similarly, an experimental report [38] using $In_{0.4}Ga_{0.6}As/GaAs$ QD solar cells reveals that increasing the number of QD layers from 10 to 30 and 50 results in an increase in short circuit current density and a decrease in open circuit voltage and efficiency.

Quantum dot solar cells short circuit current density, open circuit voltage and efficiency are highly dependent on the dot parameters, QDs areal density, QDs volume density [88, 89] and number of QD layers [90]. Experiments to determine the influence of the number of QD layers on the cell efficiency are currently underway. Here, we focus on brief theoretical analysis of the dependency of QDSC reverse saturation current, short-circuit current, open-circuit voltage, fill factor, and efficiency on the number of QD layers. Previous theoretical model [90] used different-sized QDs in different layers of the structure, but each layer has the same-sized QDs. The present study uses periodically distributed same-sized QDs in all layers in order to maintain only one electron confined state in all QD layers. Furthermore, our theoretical model presents the effect of the number of quantum dot layers on the solar cell parameters in a more simplified and general form than other

model [90], which use the carrier emission and capturing process in the multilayer QD region, requiring complicated numerical calculations.

Our theoretical model of QDSC is presented in Section 4.2. In this section, we discuss the photocurrent generated and collected in the device, and then the efficiency of quantum dot solar cell. By means of equations derived in Section 4.2, the detail analysis of the impact of the number of quantum dot layers on QDSC parameters are presented in Section 4.3. Section 4.4 concludes our findings.

4.2 Model

Figure 4.1 illustrate the model of InAs/GaAs QDSC used in this theoretical study. In this model InAs QD multi-layres are inserted in the intrinsic region of the $n^+ - i - p^+$ $GaAs$ structure. To a first approximation the depletion approximation can be used to calculate the current-voltage characteristics of an $n^+ - i - p^+$ junction solar cell. We considered a structure with n, i, and p layer thicknesses x_j, W_D, and $H^{'}$ and set $x = 0$ at the front surface of the cell. The p and n doping densities are N_A and N_D, respectively. Because

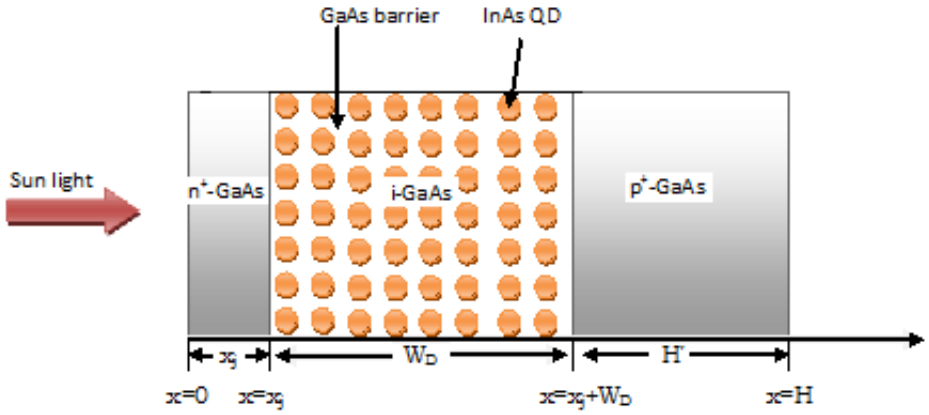

Figure 4.1: Quantum dot solar cells model.

the doping levels in the p and n regions are so much higher, then the depletion widths within the p and n regions are very small and can be neglected. Then, the space charge

region thickness is equal to the i-region thickness.

The net current is given by the sum of J_n and J_p at any point and is constant through the device in steady state. Evaluating J at x_j, we find

$$J = J_p(x_j) + J_n(x_j) \tag{4.2.1}$$

$$J = J_p(x_j) + J_n(x_j + W_D) + J_i \tag{4.2.2}$$

$$J = \int j_p(x_j, E)dE + \int j_n(x_j + W_D, E)dE + \int j_i(E)dE \tag{4.2.3}$$

4.2.1 Photocurrent Calculation of QDSC

The photocurrent generated and collected in the neutral n- and p-regions of QDSC model indicted as Fig. 4.1, are similar to the analysis of the n–p junction in Chapter 2 with minor modification. $Wn = 0$ and $Wp = 0$ for hole and electron photocurrent expressed in Eqn. (2.7.7) and Eqn. (2.7.15), respectively. Therefore, the total hole photocurrent collected from the n-region is similar to Eqn. (2.7.8) and the electron photocurrent collected from the p-region is similar to Eqn. (2.7.16).

The photocurrent generated and collected from the i-region is the sum photocurrent generated and collected from the $InAs$ quantum dots and the $GaAs$ barrier region.

To calculate the photocurrent generated and collected from the QD ensembles, we can write the generation term as [91].

$$G_D(E, x) = \alpha_{QD}(E)\phi_0(E)[1 - R(E)] \exp\big[-\alpha_{QD}(E)(x - x_j)\big], \tag{4.2.4}$$

where $\alpha_{QD}(E)$ is the absorption coefficient of QD ensemble, ϕ_0 is the photon flux and $R(E)$ is the surface reflection coefficient.

The quantum dot photocurrent generation as a function of photon energy is calculated

from

$$j_D(E) = q \int_{x_j}^{x_j + n_l S_{QD}} G_D(E, x) dx. \tag{4.2.5}$$

The integral in Eqn. (4.2.5) gives

$$j_D(E) = q\phi_0 \big[1 - R(E)\big] \big[1 - \exp\left[-\alpha_{QD}(E) n_l S_{QD}\right]\big], \tag{4.2.6}$$

were n_l is the number of QD layers and S_{QD} is the size of a single QD and defined by $S_{QD} = a_0$ and $S_{QD} = 2\overline{R}$ for cubic and spherical QD, respectively.

The total photocurrent collected from the quantum dot is given by

$$J_D = \int_{E_{QD}}^{E_g} j_D(E) dE, \tag{4.2.7}$$

where E_{QD} is the QD energy band gap and E_g is the bulk material energy bang gap.

Now, let consider the volume of single QD is V_D and the volume density of QDs is n_D (number of QDs per volume of i-region). Then, the total volume of i-region can be written as

$$V_{i-region} = (N_{QD})(V_D) + V_{barrier}, \tag{4.2.8}$$

where $V_{i-region}$ is the total volume of i-region, $V_{barrier}$ is the volume of i-region without QDs, and N_{QD} is the total number of QDs in the i-region. The volume density of QDs can be defined as $n_D = \frac{N_{QD}}{V_{i-region}}$.

Dividing both side of Eqn. (4.2.8) by $V_{i-region}$ gives

$$1 = (n_D)(V_D) + \frac{V_{barrier}}{V_{i-region}}. \tag{4.2.9}$$

Therefore, the fraction of i-region volume not occupied by QDs become $\frac{V_{barrier}}{V_{i-region}} = 1 - V_D n_D$.

The generation rate in the barrier region is written by taking in to account the attenuation

of light in the n-region and the fraction of i-region not occupied by quantum dots [91]

$$G_B(E,x) = \phi_0[1-R(E)]\exp\left[-\alpha(E)x_j\right]\left[(1-n_D V_D)\alpha(E)\right]\exp\left[-[1-n_D V_D]\alpha(E)\big(x-x_j\big)\right]. \tag{4.2.10}$$

The barrier photocurrent generated inside the i-region as a function of photon energy is

$$j_B(E) = q\int_{x_j}^{x_j+W_D} G_B(E,x)dx, \tag{4.2.11}$$

where W_D is the width of the i-region. Evaluating Eqn. (4.2.11) gives

$$j_B(E) = q\phi_0[1-R(E)]\exp\left[-\alpha(E)x_j\right]\left[1-\exp\left[-(1-V_D n_D)\alpha(E)W_D\right]\right]. \tag{4.2.12}$$

The total photocurrent can be harvested from the barrier region is

$$J_B = \int_{E_g}^{\infty} j_B(E)dE. \tag{4.2.13}$$

For trap free i-region, the photocurrent generated by light of a given photon energy in the i-region equals the sum of Eqns. (4.2.6) and (4.2.12)

$$j_i(E) = j_B(E) + j_D(E). \tag{4.2.14}$$

From Eqns. (4.2.7) and (4.2.13) total photocurrent collected from i-region is given by

$$J_i = \int_{E_g}^{\infty} j_B(E)dE + \int_{E_{QD}}^{E_g} j_D(E)dE. \tag{4.2.15}$$

From Eqns. (2.7.8), (2.7.16) and (4.2.15) the short-circuit current density of the cell is write as

$$J_{sc} = f_i(J_p^n + J_i + J_n^p), \tag{4.2.16}$$

where $f_i = 1$ is the transport factor.

4.2.2 Efficiency Calculation of QDSCs

The behavior of a solar cell is modeled by using the standard superposition approximation of an ideal diode equation. The current density is expressed as [47]

$$J(V) = J_{sc} - J_o\left[\exp\left(\frac{qV}{K_B T_c}\right) - 1\right], \tag{4.2.17}$$

where J_o is the total reverse saturated current, T_c is the temperature of the solar cell and K_B is Boltzmann's constant.

The reverse saturation current of the junction (J_o) represents the contribution of minority carriers generated at the depletion layer edges (J_{s1}) and in the i-region (J_{s2}) due to thermal excitation as given by Eqns. (4.2.20) and (4.2.21), respectively [91]. Such a current is controlled by the band gap of GaAs (E_{gB}) and average band gap of the i-region (E_{eff}).

$$E_{eff} = (1 - V_D n_D)E_{gB} + (V_D n_D)E_{gD}, \tag{4.2.18}$$

where E_{gD} is the band gap of QD and it is given by [92]

$$E_{gD} = E_g(InAs) + \frac{\pi^2 \hbar^2}{2\mu \overline{R}}, \tag{4.2.19}$$

where μ is effective mass of electron-hole pair, $E_g(InAs)$ is the band gap of bulk InAs and $\overline{R}$ is the average radius of spherical QDs.

The contribution of minority carriers generated at the depletion layer edges (J_{s1}) is expressed as

$$J_{s1} = A \exp\big(-\frac{E_{gB}}{\nu K_B T_c}\big), \tag{4.2.20}$$

where $\nu = 1.2$ is the ideality factor [91], $A = qN_v N_c\big(\frac{D_n}{N_A L_n} + \frac{D_p}{N_D L_p}\big)$. Here, N_v and N_c represent the valance and conduction band effective density of state in bulk, respectively. While N_A and N_D represent the acceptor and donor concentrations in the p-type and

n-type regions, respectively.

The thermal generation current in the i-region (J_{s2}) is obtained utilising a detailed balance between incident and emitted radiation in thermal equilibrium.

$$J_{s2} = A^{eff} \exp\big(-\frac{E_{eff}}{\nu K_B T_c}\big). \tag{4.2.21}$$

Here $A^{eff} = \dfrac{4\pi q n^2 KT}{c^2 h^3} E_{eff}^2$, and n is the i-region average index of refraction.

When the net current density in Eqn. (4.2.17) is zero and the voltage produced is the open-circuit voltage [49]. The open circuit voltage (V_{oc}) can be calculated as

$$V_{oc} = \frac{K_B T_c}{q} ln\bigg(\frac{J_{sc}}{J_o} + 1\bigg). \tag{4.2.22}$$

The fill factor (FF) of a solar cell is defined by

$$FF = \frac{V_{max} J_{max}}{V_{oc} J_{sc}}, \tag{4.2.23}$$

where V_{max} and J_{max} are the voltage and current density of the solar cell at the maximum power point, respectively. The fill factor can be expressed as a function of an open circuit voltage V_{oc} using a semi-empirical formula [93], assuming that the solar cell behaves as an ideal diode

$$FF = \frac{v_{oc} - ln[v_{oc} + 0.72]}{v_{oc} + 1}, \tag{4.2.24}$$

where $v_{oc} = \frac{q}{\nu K_B T} V_{oc}$ is a normalized voltage.

Finally, the cell power conversion efficiency is calculated using

$$\eta = \frac{V_{max} \times J_{max}}{P_0} = \frac{FF \times V_{oc} \times J_{sc}}{P_0}, \tag{4.2.25}$$

where P_0 is the incident solar power ($P_0 = 116\ mW/cm^2$ for 1 Sun, 1.5 AM condition)

4.3 Results and Discussion

We use parameters in Table 4.1, for theoretical analysis of the dependency of quantum dot solar cell J_{sc}, V_{oc}, FF and η on n_l.

Table 4.1: The physical parameters used in calculations.

Parameters	Unit	Value	Ref.
Electron surface recombination velocity (S_n)	cms^{-1}	6×10^3	[91]
Hole surface recombination velocity (S_p)	cms^{-1}	6×10^3	[91]
Electrons diffusion length of GaAs (L_n)	μm	2	[91]
Hole diffusion length of GaAs (L_p)	μm	3	[91]
Electron diffusion constant of GaAs (D_n)	cm^2s^{-1}	200	[91]
Hole diffusion constant of GaAs (D_p)	cm^2s^{-1}	10	[91]
Average radius of InAs QD ($\overline{R}$)	nm	3.1	
Number of InAs QD layers		$1 - 484$	
Volume of a single InAs QD (V_D)	cm^3	1.25×10^{-19}	
Areal density of InAs QDs (A_D)	cm^{-2}	$4.43 \times 10^7 - 2.6 \times 10^{12}$	Eqn. (4.3.2)
Volume density of InAs QDs (n_D)	cm^{-3}	$1.47 \times 10^{11} - 4.2 \times 10^{18}$	Eqn. (4.3.3)
Surface reflection coefficient ($R(\lambda)$)		0.1	[91]
Band gap of bulk GaAs (E_{gB})	eV	1.424	[94]
Band gap of bulk InAs ($E_g(InAs)$)	eV	0.354	[94]
Band gap of InAs QDs (E_{gD})	eV	1.0532	Eqn. (4.2.19)
Acceptor concentration (N_A)	cm^{-3}	1.4×10^{18}	[91]
Donor concentration (N_D)	cm^{-3}	1.7×10^{17}	[91]
n-region width (X_j)	μm	0.8	[91]
p-region width ($H^{'}$)	μm	2.0	[91]
i-region width (W_D)	μm	3.0	[91]

The absorption coefficient of bulk GaAs is calculated using Eqn. (4.3.1) [51]

$$\alpha(\hbar\omega) = \frac{\pi q^2 \hbar}{2\epsilon_r^{1/2}\epsilon_o m_o \hbar\omega c}\left(\frac{2|P_{cv}|^2}{m_o}\right)\left[\frac{\sqrt{2}(m_r^*)^{3/2}(\hbar\omega - E_g)^{1/2}}{\pi^2\hbar^3}\right]\left(\frac{2}{3}\right) = \frac{5.1\sqrt{\hbar\omega - E_g}}{\hbar\omega}, \tag{4.3.1}$$

where $\epsilon_r = 12.9$ is relative permittivity of GaAs [94], m_r^*=0.058 m_o is the reduced mass of electron-hole pair of GaAs (m_e= 0.067 m_o, m_h= 0.45 m_o) [51], the momentum matrix of bulk GaAs is approximated as $\frac{2|P_{cv}|^2}{m_o} = 25.7$ eV [51] , E_g is the band gap of bulk GaAs and $\hbar\omega$ is the photon energy. The units for E_g and $\hbar\omega$ are eV, while the unit for $\alpha(\hbar\omega)$ is $1/\mu m$.

The average refractive index of i-region is 4.16 [95], effective density of state of GaAs in valance band (N_v) and conduction band (N_c) are given by $N_v = 9 \times 10^{18}\ cm^{-3}$ and $N_c = 4.7 \times 10^{17}\ cm^{-3}$, respectively [94].

Quantum dot areal density (A_D) can be approximated by

$$A_D = \frac{1}{(2\overline{R} + X_B)^2}, \tag{4.3.2}$$

where $\overline{R}$ is average radius of QD, X_B is barrier width between QDs.

Quantum dot volume density (n_D) in terms of n_l can be written as [96]

$$n_D = \frac{n_l A_D}{W_D}. \tag{4.3.3}$$

If we have n_l number of QD layers in a fixed width W_D of i-region, then we will have $n_l + 1$ barrier width for a periodically distributed QDs. The width of the i-region can be written as $W_D = n_l(2\overline{R}) + (n_l + 1)X_B$. Therefore, the number of QD layers becomes $n_l = \dfrac{W_D - X_B}{2\overline{R} + X_B}$. Hence, the variation of the number of QD layers is due to the variation of barrier width. From this equation we can see that, to increase the number of QD layers inserted in the i-region, the barrier width must be reduced. When the QDs touch each other, the maximum number of QD layers inserted in the i-region is achieved. For $\overline{R} = 3.1$ nm, $X_B = 0$ and W_D=3.0 μm, the maximum number of QD layers inserted in the i-region becomes 484.

A spherical quantum dot optical absorption coefficient is given by [97]

$$\alpha_{QD}(\hbar\omega) = \frac{3\pi\beta}{4\overline{R}} \sum_{(n,l)} \frac{(2l+1)}{\xi k_{n,l}^2} \exp\left[- \frac{(\frac{k_{n,l}}{x_s} - 1)^2}{2\xi^2} \right], \tag{4.3.4}$$

where $(2l + 1)$ is the degeneracy, $k_{n,l}$ is the zeros of the spherical Bessel functions with index n and order l, β is a dimensionless constant defined by Eqn. (4.3.6) below and ξ is the Gaussian function relative standard deviation defined as $\xi = \dfrac{\sqrt{< (R - \overline{R})^2 >}}{\overline{R}}$ and x_s

is the reduced photon energy given by

$$x_s^2 = \frac{\hbar\omega - E_g}{\frac{\hbar^2}{2\mu\overline{R}^2}}, \tag{4.3.5}$$

where $\hbar\omega$ is the photon energy and E_g is the semiconductor material energy band gap. The constant β is given by

$$\beta = \frac{1}{\sqrt{2\pi}}\left(\frac{A\mu}{\pi^2\hbar^2}\right), \tag{4.3.6}$$

where A is defined as [97]

$$A = \frac{2\pi q^2|P_{cv}|^2}{m_0^2\varepsilon_r^{1/2}\varepsilon_0 c\omega}, \tag{4.3.7}$$

where μ is the reduced mass, P_{cv} is the momentum matrix element, ω is the photon frequency, c is the speed of light, ε is the permittivity of the host material, ε_0 is the permittivity of free space, and m_0 is the electron mass . The electron effective mass in bulk GaAs (0.067 m_0) and the vertical heavy hole effective mass in bulk InAs (0.34 m_0) are considered to be the most acceptable values for the electron and hole effective mass in InAs/GaAs quantum dots, respectively [98]. The momentum matrix element (P_{cv}) is defined as [99]

$$|P_{cv}|^2 = \frac{3m_0^2E_{gD}(E_{gD} + \Delta E_{so})}{2(3E_{gD} + 2\Delta E_{so})}\left(\frac{1}{m_e^*} - \frac{1}{m_0}\right), \tag{4.3.8}$$

where E_{gD} is the bandgap of the QD, ΔE_{so} is the spin-orbit splitting of valence bands and m_e^* is the electron effective mass. The band gap of QD is defined by Eqn. (4.2.19) and has a value $E_{gD} = 1.0532$ eV for spherical InAs QD of $\overline{R} = 3.1$ nm and $\Delta E_{so} = 0.41\ eV$ for InAs [52], thus $\dfrac{2|P_{cv}|^2}{m_0} \simeq 16.2$ eV.

4.3.1 Effect of the Number of QD layers (n_l) on the Reverse Saturated Current Density

It is necessary to first analyse the effect of the number of QD layers on reverse saturation current density, to fully comprehend the dependency of QDSC open circuit voltage, fill factor, and efficiency on the number of QD layers. Figure 4.2 illustrates the effect of the number of QDs layers on the reverse saturated current density caused by thermal excitation in the interior of the i-region (J_{s2}); plotted according to Eqn. (4.2.21). It is

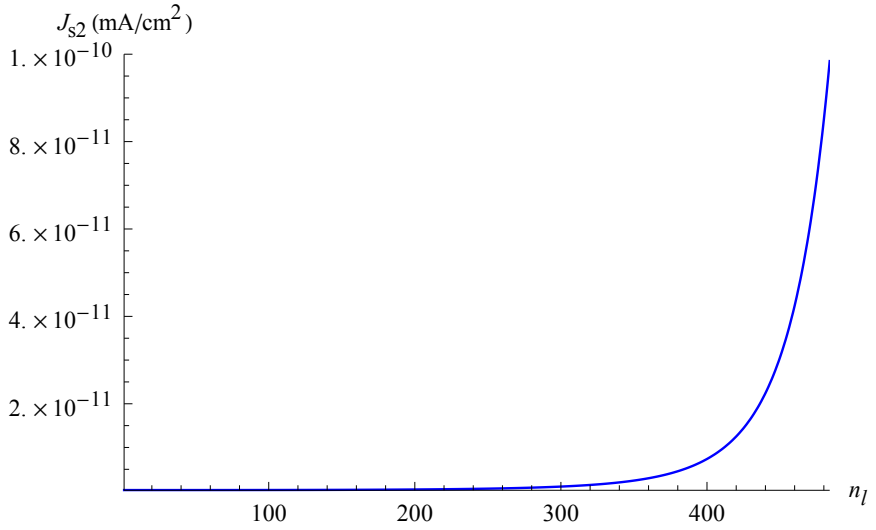

Figure 4.2: The dependency of reverse saturated current density due thermal excitation (J_{s2}) on the number of QD layers (n_l) with the help of Eqn. (4.2.21).

observed from the graph that the J_{s2} has a negligible increases till about 300 QD layers before it starts to increase exponentially. In particular, J_{s2} starts to increases very rapidly just after $\sim$ 350 QD layers. The possible reason for this can be analyzed by combining Eqn. (4.2.21) and (4.2.18), i.e., the combination of the two equations indicates that as the number of quantum dot layers increases, the effective band gap decreases whereas the reverse saturated current density increases. The decrease in the effective band gap is attributed to an increase in the recombination of carriers at the QD/barrier interface. Therefore, it can be concluded that an increase in number of QDs to over 300 QD layers increases the thermal recombination process in the intrinsic region.

The total reverse saturation current can be written by combining Eqn. (4.2.20) and Eqn. (4.2.21). It is given by

$$J_o = J_{s1} + J_{s2}. \tag{4.3.9}$$

It is worth noting that J_{s1} do not depend on the number of QDs layers and has a calculated value of $J_{s1} = 7.9 \times 10^{-16}\ mA/cm^2$. Figure 4.3 shows the effect of the number of QD

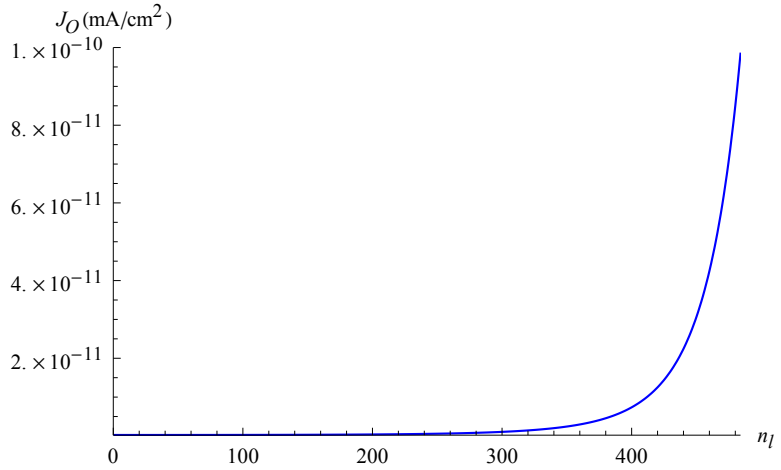

Figure 4.3: The dependency of total reverse saturated current density (J_o) on the number of QD layers (n_l) with the help of Eqn. (4.3.9).

layers on the total reverse saturation current drawn using Eqn. (4.3.9). The total reverse saturation current [Fig. 4.3] shows the same characteristics as the reverse saturated current due to thermal excitation [Fig. 4.2]. Both the reverse saturation current due to thermal excitation and the total reverse saturation current increases from $J_{s2} = 2.5{\times}10^{-13}\ mA/cm^2$ at $n_l = 0$ to $J_{s2} \sim 1.0 \times 10^{-10}\ mA/cm^2$ at $n_l = 484$. Form the aforementioned values of J_{s1} and J_{s2}, we see that the total reverse saturation current of quantum dot solar cell is dominated by thermal excitation. That is the reason why Fig. 4.2 and Fig. 4.3 are identical. Experimental report of InGaAs/GaAs quantum dot solar cell shows that as the number of QD layers is increased, so did the dark saturation current [36]. This demonstrates increased carrier recombination in the depletion region with an increase in the QD layers.

4.3.2 Dark Current Density-Voltage Characteristics Curve

Most solar cells behave like diodes [47]. The dark current density $J_{dark}(V)$ of ideal diodes is given by

$$J_{dark}(V) = J_o\left[\exp\left(\frac{qV}{K_B T_c}\right) - 1\right]. \tag{4.3.10}$$

Figure 4.4 depicts the effect of the number of QD layers on the dark current, plotted according to Eqn. (4.3.10). It is seen from the figure that the cut-in voltage of the

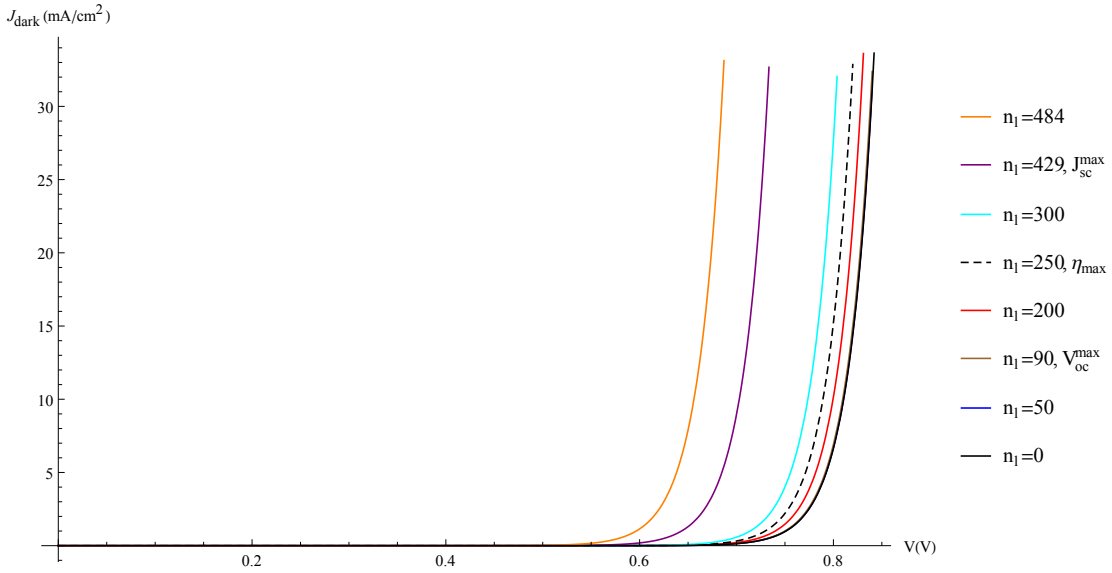

Figure 4.4: The dark current density-voltage characteristics curve plotted using Eqn. (4.3.10).

J_{dark} versus voltage (V) curve is determined by the number of QDs layers, i.e., the cut-in voltage decrease as the number of layers increases. In particular, J_{dark} is almost the same for QD layers of $n_l = 0$, 50 and 90 (as can be seen overlapped in Fig. 4.4), while J_{dark} has the largest value for $n_l = 484$ compared to the others. As it is discussed above, the recombination current in QDSC increase as the number of QD layers increases. This results in a decrease in the open-circuit voltage (V_{oc}) due to carrier recombination.

4.3.3 Effect of n_l on the Quantum Dot Photocurrent Density

Figure 4.5 illustrates the effect of number of QD layers on the QD photocurrent density drawn according to Eqn. (4.2.7). Figure 4.5 shows that the quantum dot photocurrent density increases when the number of QD layers increases and reach the maximum value of $J_D = 14.2\ mA/cm^2$ at $n_l = 484$. This figure shows the slope of the QD photocurrent

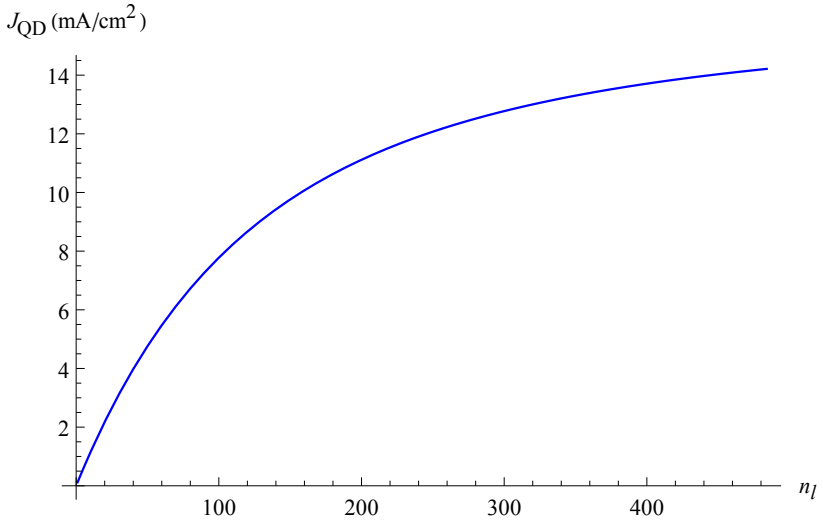

Figure 4.5: The dependence of QD photocurrent density (J_D) on the number of QD layers (n_l); plotted using Eqn. (4.2.7).

density becomes sharp from $n_l = 0$ to $\sim$ 200 but the slope slow downs after $n_l \sim$ 200. This is due to the attenuation of the light with increasing number of QD layers. When the number of QD layers increases beyond a certain limit, the generation of electron-hole pairs in QD ensembles decreases. As a result, for QD layers greater than $\sim$ 200, a small improvement in QD photocurrent density is observed. The observed increase in QD photocurrent density with number of quantum dot layers is in good agreement with the experimental report of InAs/GaAs quantum dot solar cell [39]. In this experimental report, it is found that the external quantum efficiency (EQE) at all QD-related transitions increases as the number of QD layers increases; which asserts that QD-related absorption processes are responsible for the generation of a part of the QDSC's short circuit current density.

4.3.4 Effect of n_l on the Barrier Photocurrent Density

The effect of the number of QD layers on the barrier photocurrent density is shown in Fig. 4.6; plotted according to Eqn. (4.2.13). It shows that the barrier photocurrent density

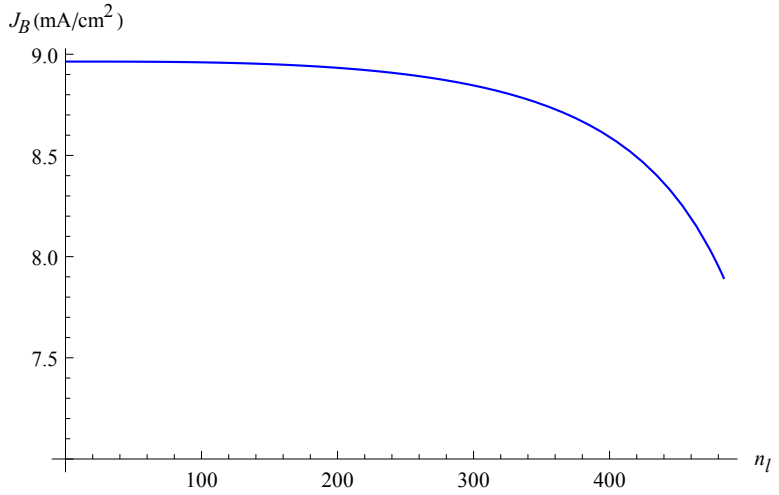

Figure 4.6: The dependence of the barrier photocurrent density (J_B) on the number of QD layers (n_l); plotted using Eqn. (4.2.13).

decrease with increasing number of QD layers for a fixed width of the i-region, reaching a minimum of 7.9 mA/cm^2 at $n_l = 484$. Small degradation of the barrier photocurrent density is observed up to $\sim$ 300 number of QD layers. However, above $\sim$ 300 number of QD layers, the degradation of barrier photocurrent density increases with increasing number of QD layers. When the number of QD layers inserted in the intrinsic region increases, then the fractional volume of i-region occupied by QDs increases. Therefore, the photocurrent generated by the barrier region decreases. The decrease in the barrier photocurrent density is related with the decrease in fractional volume of the barrier region. The relation between the barrier photocurrent density with the number of QD layers may be explained using the spectral response curve of InAs/GaAs quantum dot solar cell reported in Ref. [39]. In this experimental report, as the number of QD layers increases, the spectral response decreases for wavelengths less than the GaAs band edge while it increases for wavelengths greater than the GaAs band edge. This result confirms that the decrease in barrier photocurrent density and the increase in QD photocurrent is due

to the increase in the number of QD layers. Therefore, increasing the number of QD layers improves the QD photocurrent by absorbing lower energy photons and decreases the barrier photocurrent density by decreasing the volume fraction of the barrier region.

4.3.5 Effect of n_l on the Total Photocurrent in the i-region

Figure 4.7 shows the effect of the number of QD layers on the total photocurrent of the i-region, drawn using Eqn. (4.2.15). The total photocurrent collected from the i-region is the

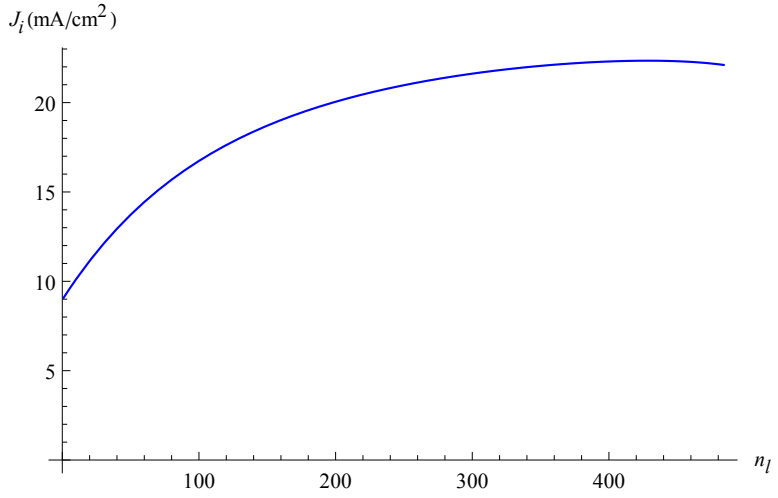

Figure 4.7: The dependence of the total photocurrent density in the i-region (J_i) on the number of QD layers (n_l); plotted using Eqn. (4.2.15).

sum of QD photocurrent density and barrier photocurrent density and it is also dependent on the number of layers of the quantum dots. The Figure shows that J_i increases with an increase in n_l and reach a maximum value of $J_i = 22.35\ mA/cm^2$ at $n_l = 429$ and then decreases to $J_i = 22.1\ mA/cm^2$ when the number of QD layers increases to 484. The observed variation of the i-region photocurrent density with the number of QD layers is in good agreement with the theoretical model of $In_xGa_{1-x}N/GaN$ quantum dot solar cell reported in Ref. [90].

4.3.6 Effect of n_l on the Short Circuit Current Density

The short circuit current density is the sum of the photocurrent densities from the n-, p-, and i-regions. The minority hole photocurrent density (J_p^n) from the emitter is defined by Eqn. (2.7.8) and is calculated to be $J_p^n = 24.23\ mA/cm^2$. The minority electron photocurrent density (J_n^p) from the base is defined by Eqn. (2.7.16) and is calculated to be $J_n^p = 0.22\ mA/cm^2$. Figure 4.8 illustrates the effect of the number of QD layers (n_l) on

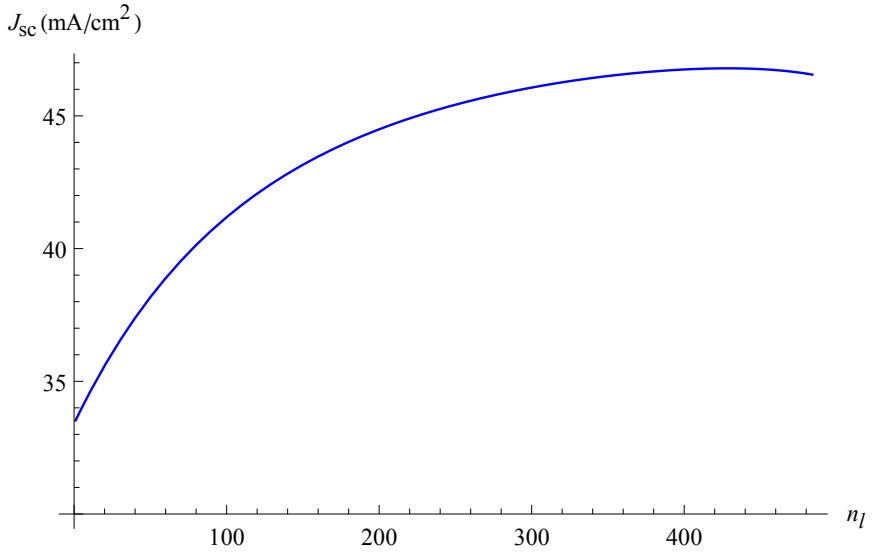

Figure 4.8: The dependence of the short circuit current density (J_{sc}) on the number of QD layers (n_l); plotted using Eqn. (4.2.16).

the short circuit current density plotted according to Eqn. (4.2.16). It is found that J_{sc} increases as n_l increases and reach its maximum value of $J_{sc} = 46.8\ mA/cm^2$ at $n_l = 429$ and then decrease to $J_{sc} = 46.6\ mA/cm^2$ when n_l increase to 484, as shown in Fig. 4.8. Hence, the insertion of large number of QD layers in the i-region has greatly enhance the photogenerated current density J_{sc} of the theoretically modeled device. This model improved short-circuit current density with an increase in QD layers is in good agreement with the experimental and theoretical results reported in Refs. [36, 39, 66, 85, 87, 90, 100, 101].

4.3.7 Effect of n_l on the Open Circuit Voltage

Figure 4.9 shows the effect of the number of QD layers on the open circuit voltage drawn according to Eqn. (4.2.22). The effect of n_l on the V_{oc} of QDSC can be related through the dependence of V_{oc} on both J_{sc} and J_o. Figure 4.9 shows that a small open circuit

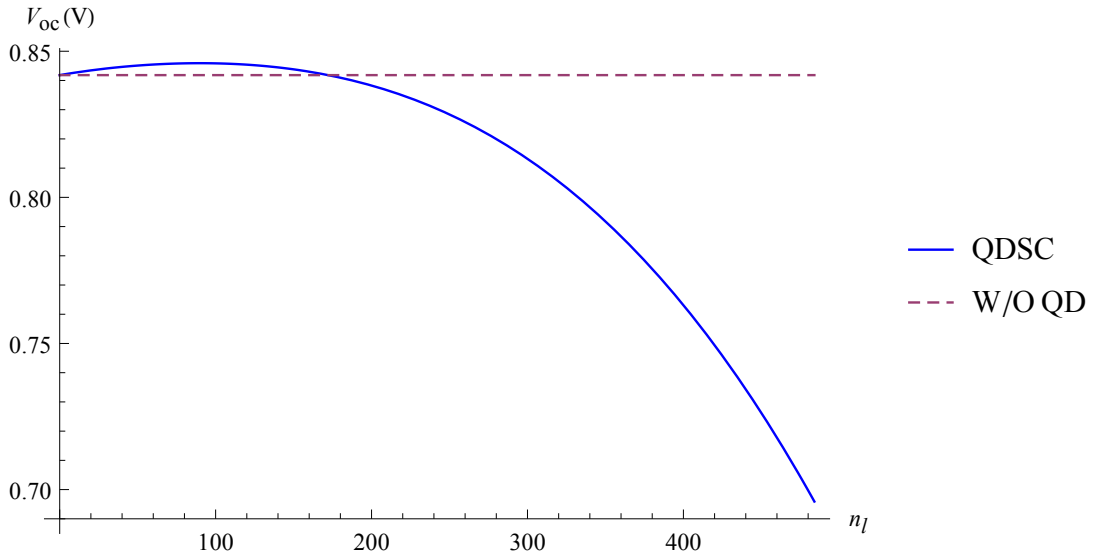

Figure 4.9: The dependence of (A) the open circuit voltage (V_{oc}) on the number of QD layers (n_l); plotted using Eqn. (4.2.22).

improvement is observed up to $n_l = 180$. Maximum $V_{oc} = 0.85\ V$ is obtained at $n_l = 90$. Above $n_l = 180$, the open circuit voltage decreases very rapidly. The increase in V_{oc} associated with a fast increase in J_{sc} for the number of QD layers less than $\sim$ 180 [Fig. 4.8], whereas a very slow increase in total reverse saturated current density is observed for the number of QD layers less than $\sim$ 180 [Fig. 4.3]. A fast degradation in open circuit voltage is the result of a fast increase in J_o above $n_l \sim 350$ [Fig. 4.3] and a small J_{sc} improvement above $n_l \sim$ 200 [Fig. 4.8]. The degradation in open circuit voltage with the increase in the number of QD layers in this model agrees with experimental and theoretical results reported in Refs. [36] and [90], respectively.

4.3.8 Effect of n_l on the Fill Factor

Figure 4.10 depicts the effect of the number of QD layers on the fill factor, plotted according to Eqn. (4.2.24). It shows that a small fill factor improvement is observed up to QD layers

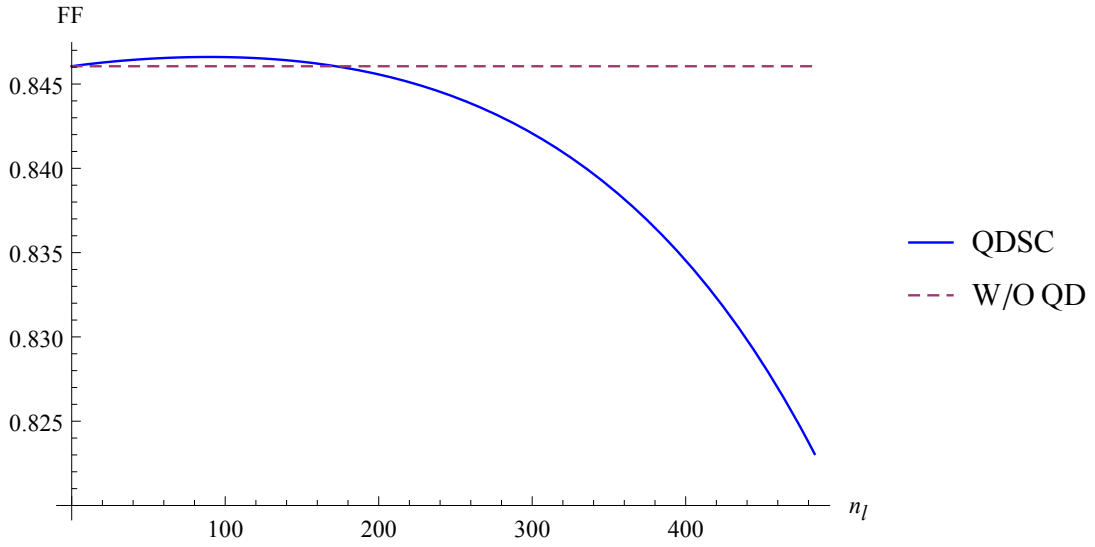

Figure 4.10: The dependence of the fill factor (FF) on the number of QD layers (n_l); plotted using Eqn. (4.2.24).

of $n_l = 180$. The maximum fill factor, i.e., $FF = 84.7\%$ is obtained at $n_l = 90$. The slight increase in the fill factor may be attributed to improved carrier transport through the intrinsic and emitter regions. Above $n_l = 180$, the fill factor decreases very rapidly. This decrease in fill factor with an increase in the number of QDs layers (beyond $n_l = 180$) can be related with a decrease in carrier transport through the intrinsic and emitter regions as a result of space charge accumulation and an increase in the recombination current with increasing number of QDs layers. Our result is in good agreement with the experimental result reported in Ref. [36].

4.3.9 Current Density-Voltage Characteristic Curves

Figure 4.11 depicts the current density-voltage (J-V) characteristic curves of InAs/GaAs QDSC structure, drawn according to Eqn. (4.2.17). The J-V characteristic curves show

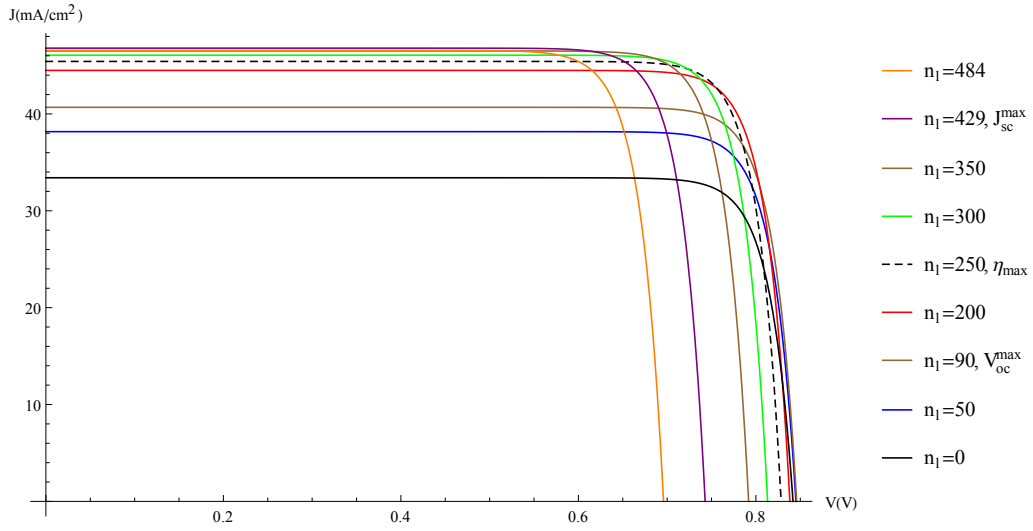

Figure 4.11: The effect of the number of QD layers (n_l) on the current density-voltage (J-V) curve, plotted using Eqn. (4.2.17).

that when the number of QDs layers increases, the short circuit current increases and the open circuit voltage decreases. However, the increase in J_{sc} above $n_l = 250$ is small, while the decrease in V_{oc} becomes more pronounced; indicating that a further increase in the QD layers above $n_l = 250$ results in a decrease of the efficiency of the QDSC structure. This theoretical model shows that using quantum dots as an intermediate band will improve the J_{sc} of the solar cell as well as its efficiency. However, there is an optimum value (about $\sim n_l = 250$) of the number of QD layers that results to the maximum possible efficiency of the theoretically modeled QDSC. It is worth noting that the obtained current density-voltage (J-V) characteristics curve agrees with the experimental result studied in Ref. [36].

4.3.10 Effect of n_l on the Efficiency

Figure 4.12 illustrates the dependence of quantum dot solar cell efficiency on the number of QD layers, plotted according to Eqn. (4.2.25). It shows that there is an optimum number of QDs layer to get maximum efficiency, which is in good agreement with the experimental reports in Refs. [36, 39, 66, 85, 87, 100] and theoretical model of quantum dot solar cells studied in Refs. [90, 102, 103]. The efficiency of QDSC is found to be

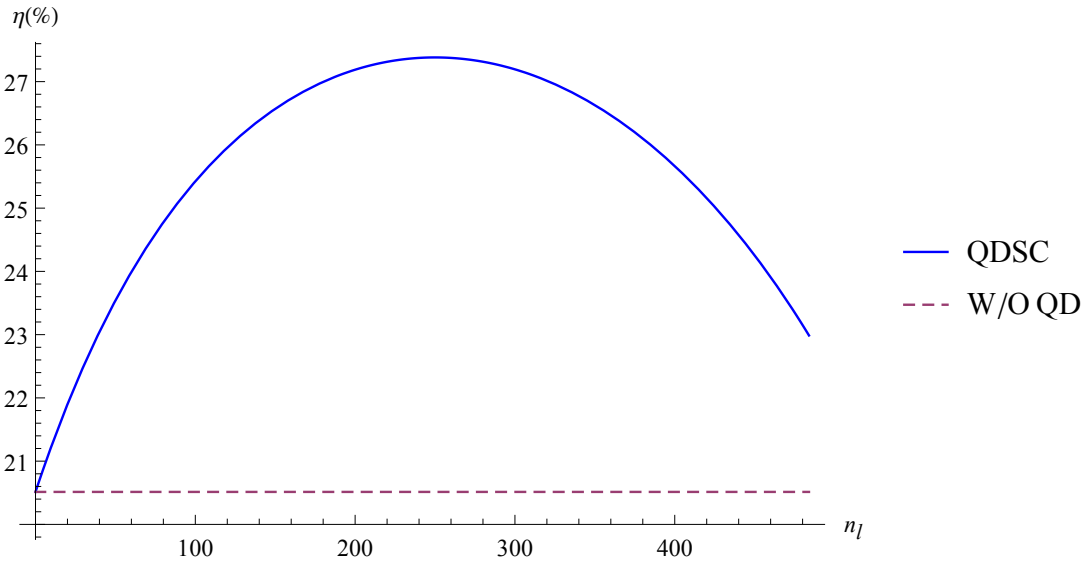

Figure 4.12: The dependence of efficiency (η) on the number of QD layers (n_l), obtained using Eqn. (4.2.25).

maximum at $n_l = 250$, and increasing the number of QD layers above this value reduces the cell's efficiency. The increase in efficiency up to 250 QD layers is due to a greater increase in short circuit current density than a decrease in the open circuit voltage and fill factor. When the number of layers exceeds 250, the slope of short circuit current density slows, because of the slope of QD photocurrent density starts to slow and the negative slope of barrier photocurrent density beginning to rise as a direct result of the attenuation of light and increasing volume fraction of QDs. Similarly, as the number of QD layers exceeds 250, the reverse saturation current due to thermal excitation increases as a result of a decrease in effective band gap. Thus, short circuit current density improved

slowly while open circuit voltage and fill factor degraded more rapidly. We can say that, the decrease in efficiency above 250 QD layers is caused by an increase in short circuit current density, which is less significant than a decrease in open circuit voltage and fill factor. Finally, we deduce that 250 layers of QD are optimal for maximum efficiency. The calculated value of J_{sc}, V_{oc}, FF and η are given in Table 4.2 along with the same configuration of solar cell with out QDs. Table 4.3 shows the comparison between our theoretical model of InAs/GaAs QD solar cell and published theoretical and experimental report of InAs/GaAs QD solar cell.

Table 4.2: The calculated value of J_{sc}, V_{oc}, FF and η of solar cell with and without QDs.

solar cell	n_l	J_{sc} (mA/cm^2)	V_{oc} (V)	F.F (%)	η (%)
without QD	0	33.4	0.84	84.6	20.5
QDSC (V_{oc}^{max})	90	40.7	0.85	84.7	25.1
QDSC (η_{max})	250	45.4	0.83	84.4	27.4
QDSC (J_{sc}^{max})	429	46.8	0.74	83.1	24.9

Table 4.3: J_{sc}, V_{oc}, FF, and η comparison for InAs/GaAs quantum dot solar cell. Note that:- NA stands for "Not Available".

InAs/GaAs QD solar cell	n_l	J_{sc} (mA/cm^2)	V_{oc} (V)	F.F (%)	η (%)
This Model	250	45.4	0.83	84.4	27.4
Theoretical [91]	NA	45.17	0.746	84.2	25.0
Experimental [39]	20	25.0	0.9	75.0	12.4
Experimental [101]	40	23.78	0.99	82.3	14.3

4.4 Conclusions

We investigated the dependence of quantum dot solar cell parameters on the number of quantum dot layers. In particular, a theoretically modeled InAs/GaAs n-i-p SC is considered. The results indicate that inserting InAs multilayer QDs into the intrinsic region of GaAs significantly improves the conversion efficiency of the n-i-p structure. The short circuit current density increased from 33.4 mA/cm^2 (without QDs) to 45.4 mA/cm^2 (with QDs), a relative enhancement of 35.9%. The conversion efficiency of the solar cell device

improved from 20.5% without QDs to 27.4% with QDs, which a relative enhancement of 33.7%. However, the efficiency of QDSC is determined by the number of QDs layers. This theoretical model shows that there is an optimum number of quantum dots layers ($n_l = 250$) to get maximum efficiency ($\eta_{max} = 27.4\%$). Above the optimum number of QDs layers the efficiency decreases. The result obtained in this theoretical model of InAs/GaAs quantum dot solar cell can be used for experimental study of QDSCs as well as in the design and fabrication of better performance solar cell panels.

Chapter 5

Effect of Cubic and Spherical Quantum Dot Size and Size Dispersion on the Performance of Quantum Dot Solar Cells

5.1 Introduction

Quantum dots are used in optoelectronics due to their three-dimensional quantum confinement of charge carriers [104, 105] and reference their in. Theoretically, solar cell energy conversion efficiency can be more than 63% by using semiconductor nanoparticles with appropriate band alignment as an intermediate band [22, 106, 107]. The overlap of the confined states of electrons results in the formation of the intermediate energy level, which can help for additional generation-recombination centers [108, 109]. These energy levels can differ due to QD size variations [104, 106, 109], allowing for absorption spectra and emissions that can be highly tunable [104]. This provides a desirable overlap between the solar spectrum and QD's absorption spectra [22, 91, 104].

Understanding the quantum dot absorption coefficient is crucial for improving QDSC power conversion efficiency. When Quantum dots of different sizes exist in a material, a Gaussian size distribution function is used to derive information about the quantum dot sample under size distribution [110]. Several researchers have investigated the effect of

QD shape, size, and size non-uniformity on the absorption spectrum of a semiconductor quantum dot system [97, 111, 112, 113]. However, the correlations between these factors used to improve power conversion efficiency of solar cells have yet to be fully revealed.

The decrease in absorption coefficient with increasing QD size was reported in Si QD [114] and InAs QD [43]. Smaller size QDs with high absorption coefficients indicate that the particles are approaching the strong confinement regime [115]. This demonstrates that the quantum confinement effect contributed to the size-dependent absorption coefficient of QDs and the quantum effect becomes more pronounced for particle distributions with a smaller mean particle diameter [116].

The type of QD used, the size of QD, the volume density of QDs, the constituent elements that make up the QD in the case of ternary QDs, the type of separating barrier, and the energy bandgap difference between the QD and the barrier all have a significant impact on the efficiency of a quantum dot solar cell [109]. To achieve the predicted high power conversion efficiencies in QDSCs, the QDs must be closely spaced, periodically distributed in all three dimensions, and homogeneous in size [117]. Several researchers have demonstrated the quantum dot size-dependent photovoltaic performance of QD SCs. Experimental results demonstrated that increasing the size of CdTe [118], CdS [119], and Si [120] quantum dots to an optimum value increases solar cell efficiency, whereas increasing above that value decreases the QDSC efficiency. According to the theoretical study of [121, 122], the photovoltaic performance of InAsN/GaAsSb QDSC is dependent on the size of the InAsN QD. Maximum efficiency is reached in these reports at an optimal size of InAsN QD. These experimental and theoretical studies indicated a correlation between QDSC efficiency and QD size.

The theoretical model in Ref. [122] used the detailed balance theory of Shockley and Queisser to demonstrate the size-dependent power conversion efficiency of QDSC. In addition, only the loss due to radiative recombination is considered. The current study uses a drift-diffusion model, as presented in Chapter 4, to explain the cubic and spherical QD

size and size dispersion dependent power conversion efficiency of QDSC.

We investigate the effects of quantum dot size and size dispersion on QDSC performance using ideal cubic and spherical InAs QDs. The absorption coefficients of cubic and spherical QDs are discussed in Section 5.2. Section 5.3 provides an in-depth analysis of the effect of QD size, size non-uniformity, and shape on the absorption coefficient of QD ensembles, QD photocurrent, and QDSC power conversion efficiency. Our findings are concluded in Section 5.4.

5.2 Model

We studied two forms of QDSC in this Chapter. Figures 5.1 and 5.2 show cubic and spherical $InAs$ quantum dots inserted in the i-region of a $GaAs$ barrier, respectively.

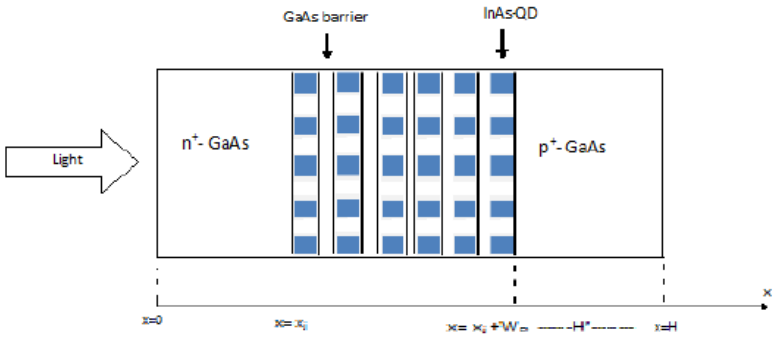

Figure 5.1: Model of QDSC with cubic QDs

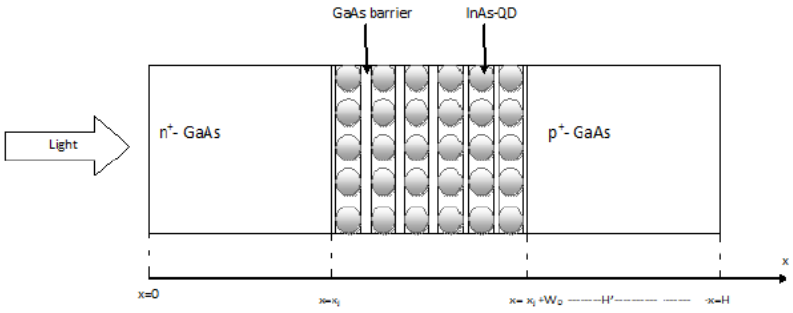

Figure 5.2: Model of QDSC with spherical QDs

5.2.1 The Optical Absorption Coefficient $\left[\alpha_{QD}(\hbar\omega)\right]$ of an Ideal Cubic QD

The absorption coefficient of cubic QD systems has been studied in detail [111, 112]. For ideal cubic QD ensemble of average size a_o, the optical absorption coefficient is given by [112]

$$\alpha_{QD}(\hbar\omega) = \frac{\beta}{a_o}\sum_{(n^2)}\frac{g(n^2)}{\xi n^2}\exp\left[-\frac{(\frac{n}{x_c}-1)^2}{2\xi^2}\right]. \tag{5.2.1}$$

Dividing Eqn. (5.2.1) by (β/a_o) gives the relative optical absorption coefficient that is given by

$$\alpha_{QD}^{rel}(\hbar\omega) = \sum_{(n^2)}\frac{g(n^2)}{\xi n^2}\exp\left[-\frac{(\frac{n}{x_c}-1)^2}{2\xi^2}\right], \tag{5.2.2}$$

where g is the degeneracy of the energy level determined by $n^2 = \sum n_j^2$ where $j = 1, 2, 3...$, and β is a constant given by Eqn. (4.3.6).

Defining two dimensionless parameters in Eqn. (5.2.1): the reduced photon energy x_c

$$x_c^2 = \frac{\hbar\omega - E_g}{\frac{\pi^2\hbar^2}{2\mu a_0^2}}, \tag{5.2.3}$$

and the relative standard deviation of the dot size ξ as

$$\xi = \frac{\sqrt{\left\langle (a-a_0)^2\right\rangle}}{a_0}, \tag{5.2.4}$$

where a is the side length of a QD, E_g is the bandgap energy of the semiconductor material, $\hbar\omega$ is the photon energy, and μ the reduced mass of electron–hole pair.

Equation (5.2.1) describes a set of Gaussian absorption peaks with $n/x_c = 1$ at the peak position. As a result, the photon energy at the peaks is determined only by the average dot size a_0, and the energies are unaffected by the size distribution. i.e.,

$$\hbar\omega = E_g + \frac{n^2\pi^2\hbar^2}{2\mu a_0^2}. \tag{5.2.5}$$

The energy bandgap of cubic QD E_{QD} is given by [123]

$$E_{QD} = E_g(InAs) + \frac{3\pi^2\hbar^2}{2\mu a_0^2}, \tag{5.2.6}$$

where $E_g(InAs)$ is the bandgap of bulk $InAs$.

5.2.2 The Optical Absorption Coefficient $\left[\alpha_{QD}(\hbar\omega)\right]$ of an Ideal Spherical QD

The optical absorption coefficient of a spherical quantum dot ensemble with an average radius of $\overline{R}$, have been studied in detail [97], and it is given by

$$\alpha_{QD}(\hbar\omega) = \frac{3\pi\beta}{4\overline{R}} \sum_{(n,l)} \frac{(2l+1)}{\xi k_{n,l}^2} \exp\left[- \frac{(\frac{k_{n,l}}{x_s} - 1)^2}{2\xi^2} \right]. \tag{5.2.7}$$

Dividing Eqn. (5.2.7) by $(\beta/2\overline{R})$ gives the relative optical absorption coefficient that is given by

$$\alpha_{QD}^{rel}(\hbar\omega) = \frac{3\pi}{2} \sum_{(n,l)} \frac{(2l+1)}{\xi k_{n,l}^2} \exp\left[- \frac{(\frac{k_{n,l}}{x_s} - 1)^2}{2\xi^2} \right], \tag{5.2.8}$$

where $(2l+1)$ is the degeneracy. In these equations, $k_{n,l}$ refers to the zeros of the spherical Bessel functions with index n and order l.

The reduced photon energy x_s for spherical QD is given by

$$x_s^2 = \frac{\hbar\omega - E_g}{\frac{\hbar^2}{2\mu\overline{R}^2}}. \tag{5.2.9}$$

Equation (5.2.7) represents a set of Gaussian absorption peaks with peak position at $k_{nl}/x_s = 1$. Thus the peaks have photon energy determined by the average dot radius $\overline{R}$ only; the energies are not affected by the size distribution. i.e.,

$$\hbar\omega = E_g + \frac{k_{nl}^2\hbar^2}{2\mu\overline{R}^2}. \tag{5.2.10}$$

The energy bandgap of spherical QD E_{QD} is given by [92]

$$E_{QD} = E_g(InAs) + \frac{\pi^2\hbar^2}{2\mu\overline{R}^2}. \tag{5.2.11}$$

5.3 Results and Discussion

In our theoretical model, $InAs$ QDs are embedded in the i-region of the $GaAs$ n-i-p structure to enhance solar radiation absorption below the bandgap of $GaAs$. To make the bandgap of $InAs$ QDs below the bandgap of bulk $GaAs$, the average size of a cubic $InAs$ QD must be more than 4.4 nm ($a_0 > 4.4\ nm$) and the average radius of a spherical $InAs$ QD must be greater than 2.5 nm ($\overline{R} > 2.5\ nm$). If the average size/radius of QDs falls below this value, the bandgap of $InAs$ QDs becomes larger than the bandgap of $GaAs$. We use comparable volumes of cubic and spherical $InAs$ QDs to investigate the effect of QD size and size dispersion on the QD absorption coefficient, QD photocurrent, and QDSC efficiency. For comparison in the figures, the average radius of the spherical $InAs$ QDs ($\overline{R}$) is stated in terms of the average size of the cubic $InAs$ QDs (a_0), using $\overline{R} = 0.62a_0$. To improve photocurrent generation, the absorption spectra of QDs must match the portion of the solar spectrum. The spectrum of the QD absorption coefficient is primarily governed by dot parameters such as dot size, size non-uniformity (also known as size dispersion; ξ), and dot shape. As a result, the spectrum of the absorption coefficient of QDs can be optimized by selecting suitable dot parameters to serve this purpose.

5.3.1 Absorption Coefficient Spectrum

We employ a comparable volume of cubic InAs QD ensemble ($a_0 = 5.0\ nm$) and spherical InAs QD ensemble ($\overline{R} = 3.1\ nm$) to investigate the effect of QD size dispersion (ξ) on the absorption coefficient spectrum of an InAs/GaAs QD system. For this analysis, four QD size dispersion values ($\xi = 0.01,\ 0.02,\ 0.05,\ and\ 0.1$) were utilized. The lowest confined

state in cubic and spherical InAs quantum dot systems, denoted by $n^2 = 3$ [111, 112, 113] and $k_{1,0} = \pi$ [97], respectively.

Figure 5.3 depicts the effect of QDs size dispersion on the optical absorption spectra of InAs cubic and spherical quantum dot ensembles at the lowest transition. The horizontal axis represents photon energy, as specified by Eqns. (5.2.5) and (5.2.10) for cubic and spherical QD systems, respectively. The absorption coefficient of the cubic and spherical QDs are given by Eqns. (5.2.1) and (5.2.7), respectively. As shown in Fig. 5.3, increasing ξ results in a significant decrease in absorption intensities and an increase in the line width of the optical absorption coefficient spectrum. The absorption spectrum peak is due to

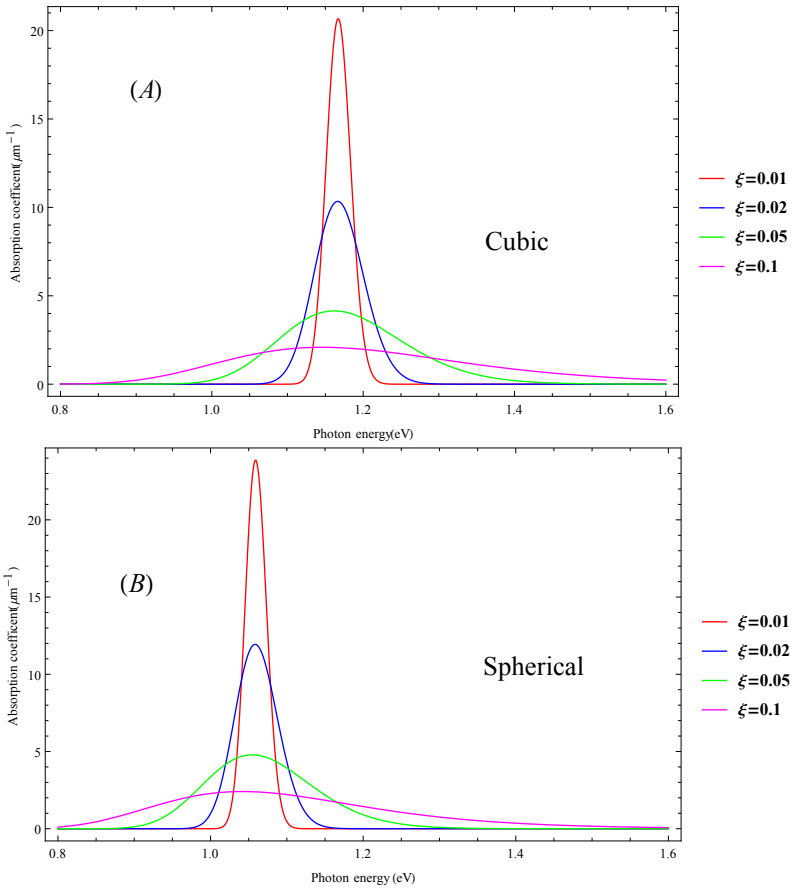

Figure 5.3: Absorption spectra of the lowest transition of the InAs/GaAs QD system corresponding to both cubic (A) and spherical (B) quantum dots for relative standard deviation $\xi = 0.01,\ 0.02,\ 0.05,\ and\ 0.1$. The photon energy for cubic and spherical QD systems are defined by Eqns. (5.2.5) and (5.2.10) are used, respectively. The absorption coefficients of the cubic and spherical QD systems are defined by Eqns. (5.2.1) and (5.2.7) are employed, respectively.

light absorption by quantum dots, and its sharpness is proportional to the QDs size dispersion. The physical interpretation of a QDs ensemble with a smaller ξ value is that the probability of finding QDs with a particular size (a_0) or radius ($\overline{R}$) is large. As a result of the more uniform QDs size in the ensemble, there is an intense optical absorption coefficient peak at the resonance energy. The optical absorption coefficient spectrum will have a narrower line width because it covers a smaller portion of the solar spectrum. A higher ξ value, on the other hand, indicates that the probability of finding QDs of a particular size (a_0) or radius ($\overline{R}$) is small. Due to higher levels of QDs size/radius non-uniformity in the ensemble, the intensity of the optical absorption coefficient peaks at the resonance energy is reduced. As the QD ensemble optical absorption coefficient covers a larger portion of the solar spectrum, the optical absorption coefficient spectrum will have a broader line width. The peak absorption coefficient of a spherical QDs ensemble is greater than that of a cubic QDs ensemble of the same volume. In contrast, the bandgap edge resonant energy of cubic QDs ensembles is 0.1 eV photon energy higher than that of spherical QDs ensembles. Our analysis is in good agreement with the work reported in [97] for a GaAs QD system, regardless of the type of QDs. It was found that spherical GaAs QD has a higher absorption peak than cubic GaAs QD and that the resonant energy of cubic GaAs QD is higher than that of spherical GaAs QD of comparable volume. Available experimental report of absorption and photoluminescence (PL) of the optical emission from the ground state of InAs QDs ensembles has energy around 1.1 eV [124], 1.0 eV [125], 1.075 eV [126], 1.05 eV [127], and 1.17 eV [128] for InAs/GaAs QD ensembles. The present theoretical model peak absorption coefficient from the ground state is at a resonant energy of 1.16 eV (for cubic QDs of $a_0 = 5.0\ nm$) and 1.06 eV (for spherical QDs of $\overline{R} = 3.1\ nm$).

Figure 5.4 shows the effects of size dispersion on the relative absorption spectra of InAs cubic and spherical quantum dot ensemble for the lowest three transitions. For cubical InAs quantum dot ensemble the lowest three confined states are specified by the quantum number $n^2 = 3,\ 6,\ and\ 9$ [111, 112, 113], and for spherical InAs quantum dot ensemble the

lowest three confined states are specified by the quantum number $k_{nl} = \pi,\ 4.49,\ and\ 5.76$ [97]. In Fig. 5.4, the three lowest transitions were plotted for four values of $\xi = 0.01$ (Figs. 5.4A and 5.4E), 0.02(Figs. 5.4B and 5.4F), 0.05 (Figs. 5.4C and 5.4G), and 0.1 (Figs. 5.4D and 5.4H). In each of these plots, the solid lines represents the individual relative absorption spectrum and the dot lines represent their superposition. Fig. 5.4A to 5.4D are corresponding to the cubic QD system and Fig. 5.4E to 5.4H are corresponding to the spherical QD system.

When $\xi = 0.01\ and\ 0.02$, the relative absorption peaks corresponding to different transition levels are separated in both the cubic (Figs. 5.4A and 5.4B) and spherical QD systems (Figs. 5.4E and 5.4F). Since the QDs ensemble has greater size homogeneity, overlapping between nearby transitions is not observable in these absorption spectra. When $\xi = 0.05$, the two higher energy absorption peaks begin to overlap, but the three peaks remain distinct in both cubic (Fig. 5.4C) and spherical QD (Fig. 5.4G). The overlapping between the second and third transitions occurs at photon energies ranging from $\sim\ 2.1\ to\ \sim\ 2.4\ eV$, as shown in Figs. 5.4C and 5.4G. When $\xi = 0.1$, only the first relative absorption peak is resolved in both cubic (Fig. 5.4D) and spherical QD (Fig. 5.4H). The overlapping between the second and third transitions occurs in the photon energy range of $\sim\ 1.8\ to\ \sim\ 3.3\ eV$, while the overlapping between the first and second transitions occurs in the photon energy range of $\sim\ 1.3\ to\ \sim\ 1.8\ eV$. Furthermore, at $\xi = 0.1$, the superposition spectra of the three transitions show an intense absorption peak and a broader line width (dotted line in Figs. 5.4D and 5.4H). The overlapping between nearby transitions, as well as the photon energy range of the overlapping confined states, increases as the QDs size non-uniformity increases, as shown in Fig. 5.4. It was found that the resolvability of absorption peaks depends on ξ. According to the prior discussion, the overlapping between nearby transitions arises due to QD size non-uniformity. As a result, photons with energies within the overlapping range are capable of triggering electron transitions from either of the nearby

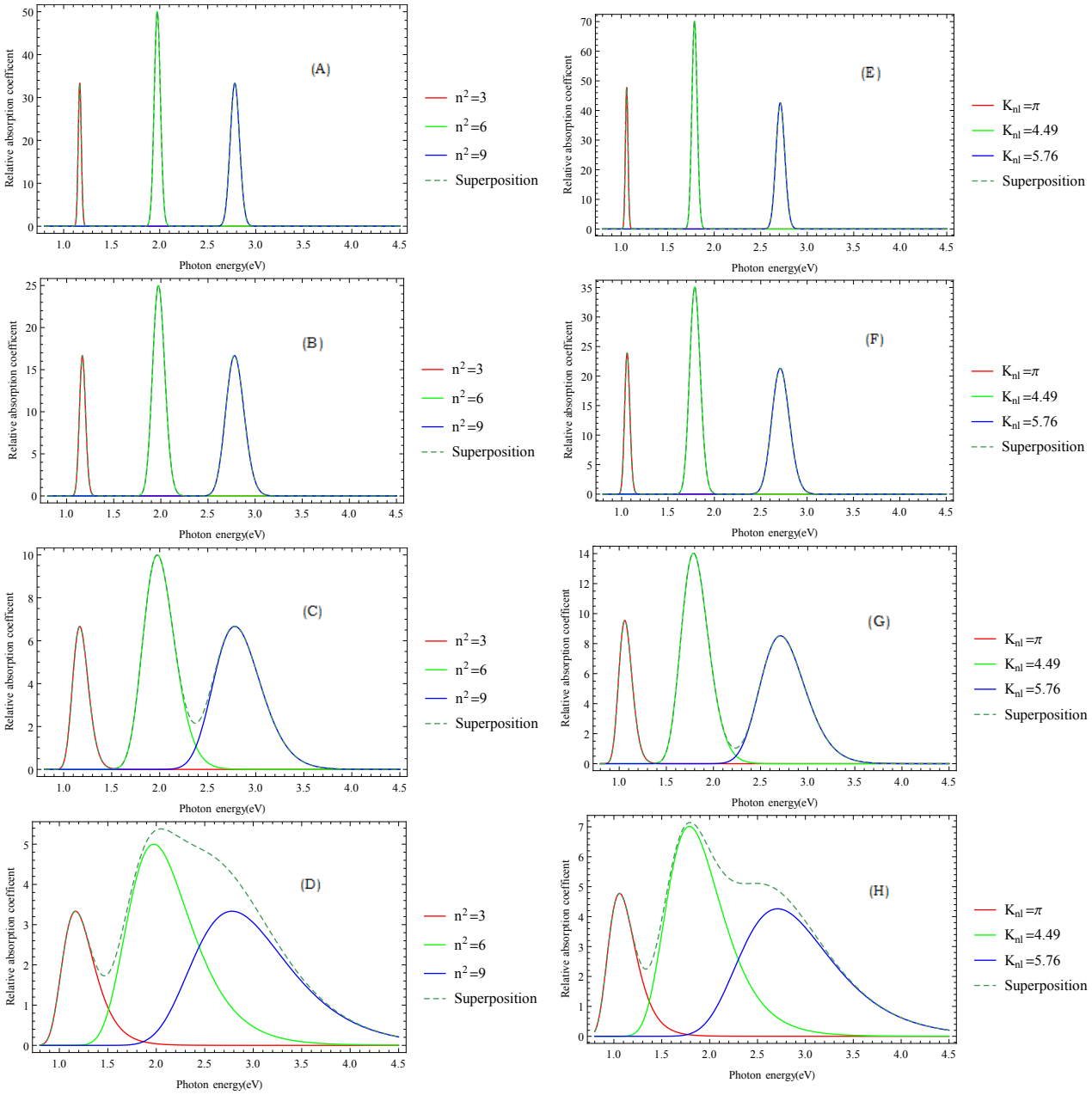

Figure 5.4: Relative absorption spectra of the lowest three transitions of the InAs/GaAs QD system corresponding to both cubic (A-D) and spherical (E-H) quantum dots for relative standard deviation $\xi = 0.01,\ 0.02,\ 0.05,\ and\ 0.1$. In each of these plots, the solid and dotted lines represent the individual absorption peaks and their superposition, respectively. The photon energy for cubic and spherical QD systems are defined by Eqns.(5.2.5) and (5.2.10) are employed, respectively. The relative absorption coefficients of the cubic and spherical QD systems are defined by Eqns. (5.2.2) and (5.2.8) are used, respectively.

confined states. The overlapping of relative absorption peaks with increasing ξ was observed in theoretical reports of GaAs QD [97, 111] and $In_{0.7}Ga_{0.3}N/GaN$ QD system [112]. To investigate the effects of QD average size/radius on the absorption coefficient, we must first understand the effect of quantum confinement on the QD system's momentum matrix. The momentum matrix element is defined by Eqn. (4.3.8) is dependent on the energy bandgap of QD, so as on the average size of QDs. Smaller average-size QDs have a higher momentum matrix element due to higher quantum confinement energy, whereas larger average-size QDs have a lower momentum matrix element due to lower quantum confinement energy.

The effect of QD size on the absorption coefficient of QDs ensembles is investigated by combining Eqns. (4.3.6), (4.3.7), (5.2.1), and (5.2.3) for cubic QD and Eqns. (4.3.6), (4.3.7), (5.2.7), and (5.2.9) for spherical QD. According to these equations and the size-dependent momentum matrix element (Eqn. (4.3.8)), it is expected that the absorption coefficient decreases as the size of QD increases.

Figure 5.5 allows us to analyze the effects of the size/radius of QDs on the optical absorption spectrum of cubic and spherical quantum dot systems with comparable volumes. The average sizes of the cubical QD ensemble are $a_0 = 5.0,\ 6.0,\ 7.0,\ and\ 8.0\ nm$ and the average radius of spherical QD ensemble are $\overline{R} = 3.1,\ 3.7,\ 4.3,\ and\ 4.96\ nm$. These average sizes are chosen so that the cubic and spherical quantum dots will have comparable volumes. For each linewidth of the Gaussian function, it is shown that the curves corresponding to cubic and spherical quantum dots are similar. It is observed that the absorption coefficient of QDs decreases when the size/radius of QDs increases. In addition, one can see that the absorption peak shifted to the lower photon energy (reds shift) when the average size/radius of QD increases. The possible explanation for this is that smaller size/radius QDs have larger absorption coefficients due to larger confinement energy and larger QDs have smaller absorption coefficients due to poor confinement energy. In general, the peak shift in the absorption spectra is related to the size of the QDs. Our result

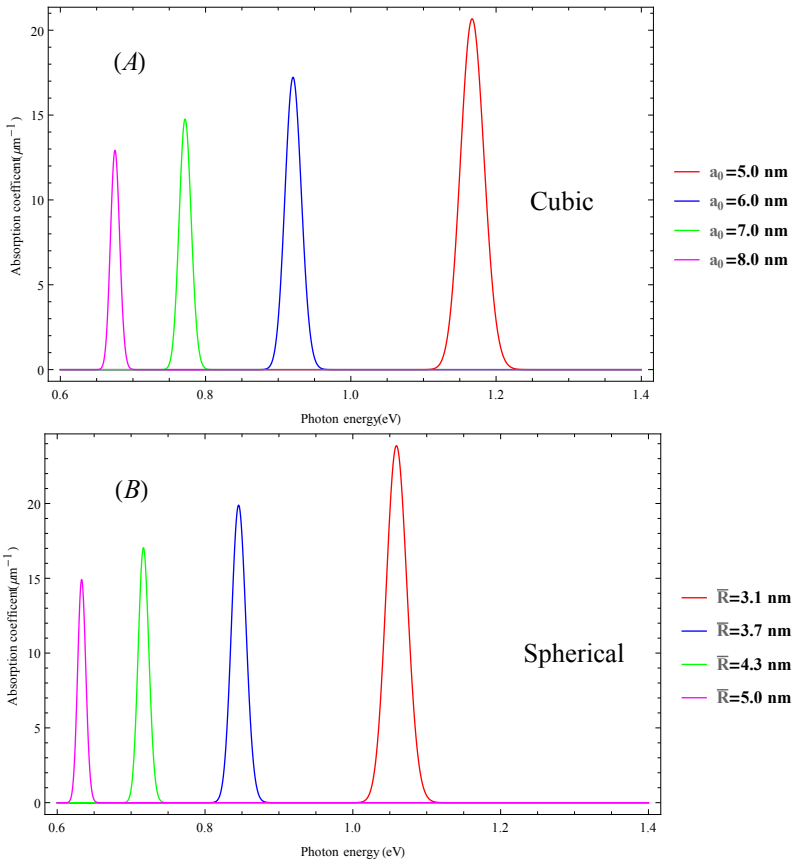

Figure 5.5: Absorption spectra of the lowest transition of the InAs/GaAs QD system corresponding to both cubic (A) and spherical (B) quantum dots for relative standard deviation $\xi = 0.01$. The photon energy for cubic and spherical QD systems are defined by Eqns. (5.2.5) and (5.2.10) are used, respectively. The absorption coefficients of the cubic and spherical QD are defined by Eqns. (5.2.1) and (5.2.7) are employed, respectively.

is in good agreement with experimental [114] and theoretical reports [43].

We compared our model absorption spectrum of 5 nm InAs/GaAs with the theoretical model [43] of 5 nm InAs/GaAs absorption spectra and experimental report [42] of the electroluminescence (EL) spectra of 5 nm dot-hight InAs/GaAs QDSC. In our model, the peak absorption coefficient for ground state transition of cubic QDs ensembles is located at 1.16 eV, and in the Srimurugan et.al. [43] it is located at a wavelength of 1135 nm (1.09 eV). Similarly, in the Jihene et.al. [42] the EL band maxima located at a wavelength of 1120 nm (1.11 eV). Thus, our model absorption spectrum of 5 nm InAs/GaAs cubic QD was found to be matching with the theoretically calculated absorption coefficient of 5 nm InAs cubic QDs as well as the experimental result of 5 nm dot-hight InAs/GaAs QDSC .

Figure 5.6 depicts the variation of the QD absorption coefficient with QD size and size dispersion. Figure 5.6A shows the effect of QDs size on the absorption coefficient. It is observed that the absorption coefficient decreases when QD size increase. This is in agreement with the absorption spectrum of Fig. 5.5. The high absorption coefficient of smaller-size QDs implies that the particles are approaching the strong confinement regime. This confirms that the quantum confinement effect plays a part in the size-dependent absorption coefficient of QDs [43]. A similar finding was obtained in an InAs QD theoretical model [43].

Figure 5.6B shows the effect of QDs size dispersion on the absorption coefficient. It is observed that the absorption coefficient decreases when QD size dispersion increases. This is in agreement with the absorption spectrum of Fig 5.3. A higher QD absorption coefficient for smaller size dispersion indicates that the absorption coefficient spectrum has a narrower line width and a sharp peak, covering a smaller portion of the solar spectrum. A lower QD absorption coefficient for larger size dispersion indicates that the absorption coefficient spectrum has a broader line width, covering a larger portion of the solar spectrum.

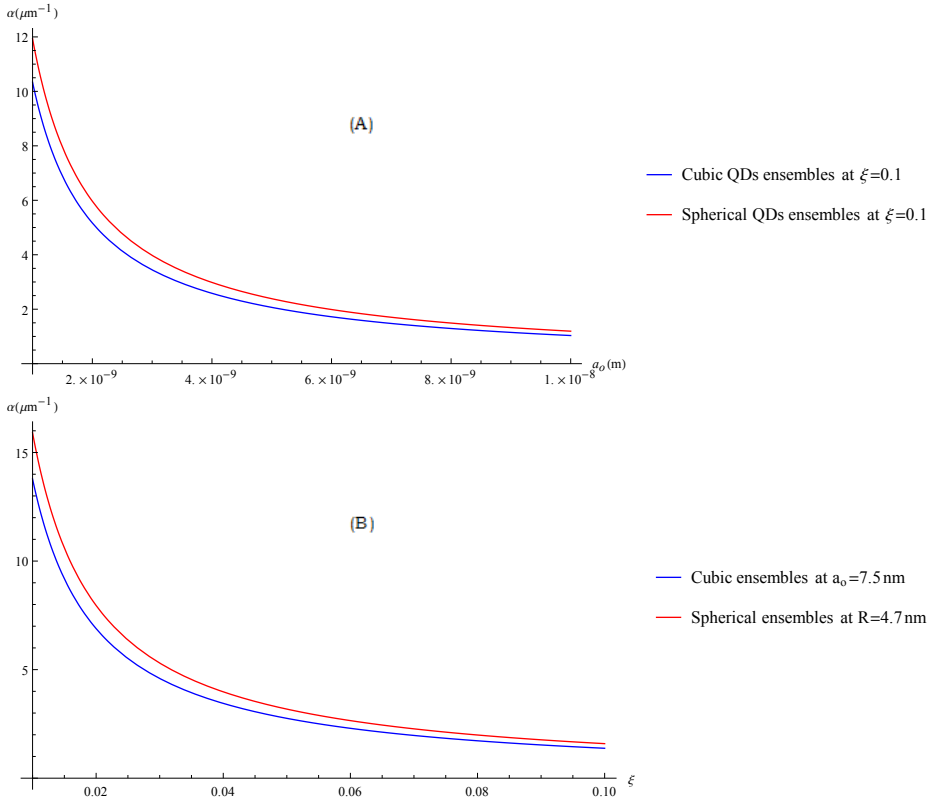

Figure 5.6: Effect of QD size (A) and size-dispersion (B) on the absorption coefficient of QD ensemble. The bandgap energy for cubic and spherical QDs are defined by Eqns. (5.2.6) and (5.2.11) are employed, respectively. The absorption coefficients of the cubic and spherical QDs are defined by Eqns. (5.2.1) and (5.2.7) are used, respectively.

5.3.2 Quantum Dot Photocurrent

Figure 5.7 depicts the simultaneous effect of both QD average size and QDs size dispersion on QD photocurrent. Maximum J_{QD} values are found for cubic QDs with a_o ranging from 7.2 nm to 9.5 nm and ξ ranging from 0.05 to 0.25 (Fig. 5.7A). Similarly, the better J_{QD} values for spherical QDs (Fig. 5.7B) are achieved within $\overline{R}$ ranging from 4.2 nm to 5.6 nm and ξ ranging from 0.06 to 0.26. As a result, there is an optimum range of average QD size and QDs size dispersion to achieve maximal QD photocurrent. Increasing above or decreasing below this optimal range reduce QD photocurrent. Therefore, to improve the quantum dot photocurrent the optimized size and size dispersion of QD must be chosen. To investigate the effect of QD size on quantum dot photocurrent, $\xi = 0.1$ was optimized applying the optimum range of ξ for achieving maximum QD photocurrent, as depicted in Fig. 5.7. Figure 5.8A shows the effect of QD size on quantum dot photocurrent.

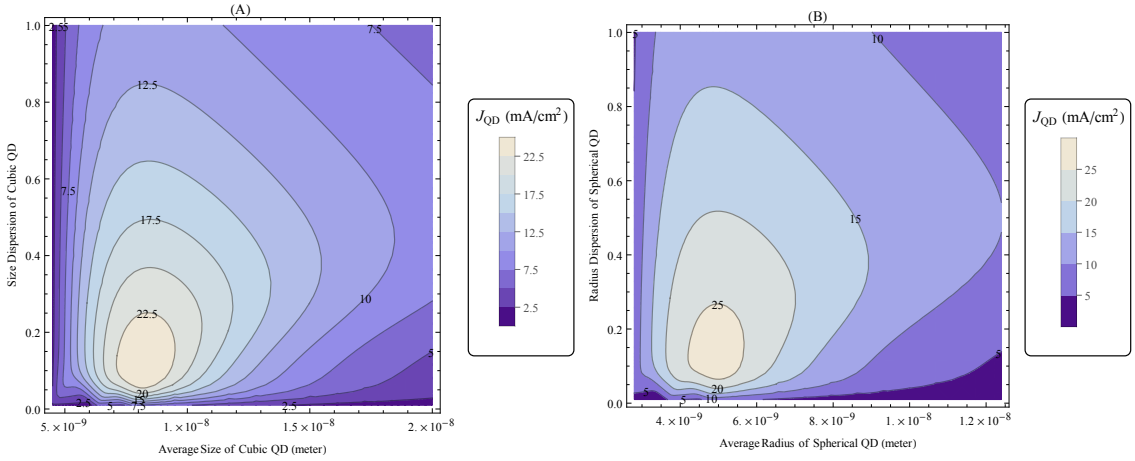

Figure 5.7: Quantum dot photocurrent as functions of average size of QD and QD size dispersion (A) cubic QDs and (B) spherical QDs. The quantum dot photocurrent is defined by Eqns. (4.2.7).

There is an optimum QDs size to get maximum QD photocurrent. The dependence of QD photocurrent on QD size can be explained by applying the size-dependent nature of the QD absorption coefficient and the wavelength range of the higher-intensity solar spectrum. Since small QDs cannot absorb long wavelengths of light, only a portion of the solar

spectrum can be utilized. Larger QDs, on the other hand, absorb long wavelength light, although the vast majority of the solar spectrum lies in the visible range. This competitive relationship between light absorption based on QD size and the solar spectrum could lead to the optimal QD size to obtain maximum QD photocurrent. The maximum quantum dot photocurrent can be obtained at the cubic QD average size of $a_o = 8.1\ nm$ ($J_{QD} = 24.7\ mA/cm^2$) and the spherical QD average radius of $\overline{R} = 5.0\ nm$ ($J_{QD} = 26.9\ mA/cm^2$). Fig. 5.8A also demonstrates that the QD photocurrent of QDSC with cubic and spherical QDs is roughly the same for QD sizes larger than $\sim\ 10.0\ nm$. On the other hand, below $\sim\ 10.0\ nm$ of QD size QDSC with spherical QDs has a higher QD photocurrent than cubic QDs. The lack of shape-dependent QD photocurrent characteristics in the large-size QDs could be due to poor confinement energy. Since the confinement energy decreases with increasing QD size, addressing the shape effect on QD photocurrent is pointless in the low confinement energy regime. It should be noted that $\overline{R} = 0.62a_0$ was used in the prior discussion and Fig. 5.8A for convenience.

To analyze the effect of QD size dispersion on quantum dot photocurrent, a QD average size of $a_o = 8.0\ nm$ was optimized using the optimal range of average QD size for achieving maximum QD photocurrent, as depicted in Fig. 5.7. Figure 5.8B shows the effect of QD size non-uniformity (ξ) on the quantum dot photocurrent. It is observed that there is an optimum QDs size dispersion to get maximum quantum dot photocurrent for both cubic and spherical QDs. The QDs size dispersion-dependent nature of the QD absorption coefficient and the solar spectrum are used to explain why this could happen. Because smaller size dispersion QD ensembles have higher and sharper absorption peaks, they cover a lesser portion of the solar spectrum. On the other hand, larger-size dispersion QD ensembles have a lower absorption peak and a wider bandwidth, allowing them to cover greater portions of the solar spectrum. Because of the competitive relationship between peak absorption coefficient and line width broadening, an optimum size dispersion of QD is obtained to provide maximal QD photocurrent. The highest quantum dot photocurrent

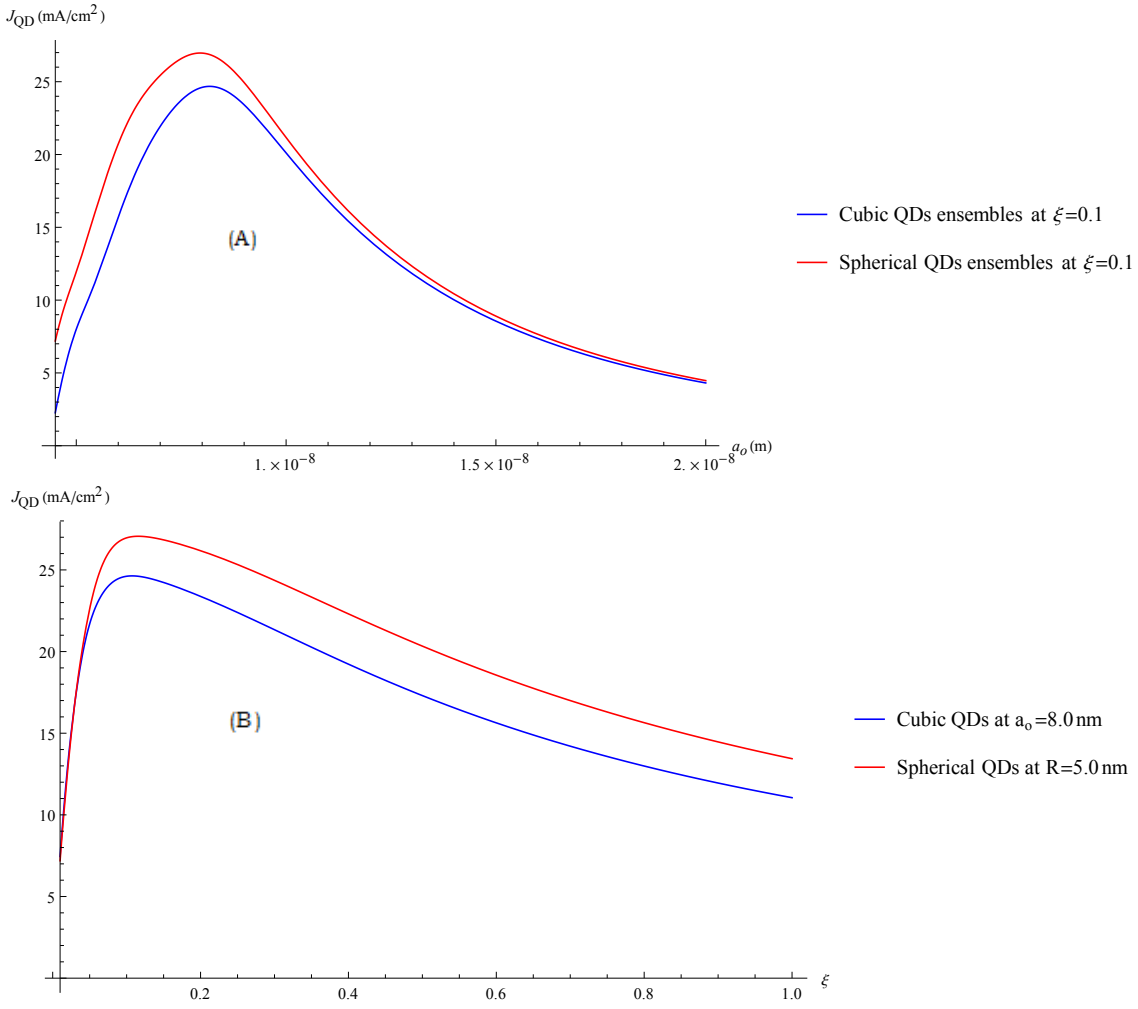

Figure 5.8: Effect of QD size (A) and size dispersion (B) on quantum dot photocurrent. The quantum dot photocurrent is defined by Eqns. (4.2.7).

can be obtained at the QDs size dispersion of 0.11 ($J_{QD} = 24.6\ mA/cm^2$) and 0.12 ($J_{QD} = 27.0\ mA/cm^2$) for the cubic and spherical QDs, respectively. It should be noted that for each QD size dispersion, there is a specific QD average size that provides the highest QD photocurrent. Figure 5.8B also demonstrates that the QD photocurrent of QDSC with cubic and spherical QDs is roughly the same for QD size dispersion less than $\sim$ 0.04. Above this value of QDs size non-uniformity, the QD photocurrent of QDSC with spherical QDs is larger than cubic QDs. As a result, addressing the shape-dependent properties of QD photocurrent is worthless for size non-uniformity less than $\sim$ 0.04 in this particular investigation.

5.3.3 JV Characteristics

Figure 5.9A shows the effect of QD size on the JV curve of QDSC with cubic QDs ensembles, it shows that there is a higher improvement in short circuit current for $a_o = 8.1\ nm$. Figure 5.9B shows the effect of QD size on the JV curve of QDSC with spherical QDs ensembles, it shows that there is a higher improvement in short circuit current for $\overline{R} = 5.0\ nm$. For both cubic and spherical QDs ensembles the open circuit voltage decrease as the size of QDs increases. We notice that changing the size of QDs changes both the short circuit current and open circuit voltage by a significant amount. The drop in open circuit voltage with increasing QDs size can be explained by the bandgap shift caused by the quantum confinement effect. When the size of QDs increases, the bandgap shift between the conduction band of the barrier and the intermediate band increases, which decrease escaping of the electrons from QDs to the barrier. Thus, larger size QD can easily recapture the photogenerated carrier during carrier transport [43]. This results in an increase in the recombination process. In other words, when the size of QDs increases, the effective bandgap decreases (i.e. the conduction band shifts downwards due to the weaker quantum confinement effect). The decrease in the effective bandgap increases the recombination at QD/barrier interface which leads to a decrease in V_{oc}. The decrease in short circuit current

with an increase in the size of QDs is related to the mismatch between the bandgap of QDs and the solar spectrum. A similar JV curve is observed in the theoretical model of InAs/GaAs QDSC[43].

Figure 5.10 shows the JV curve of QDSC for different QDs size dispersion. It shows that short circuit current decrease as the size dispersion increases but no significant change in the open circuit voltage was observed when the size dispersion of QDs increases. This can be explained by the strong relationship between V_{oc} and the size of QDs. For a fixed size of QDs, there is no significant change in the open circuit voltage with a change in QDs size dispersion.

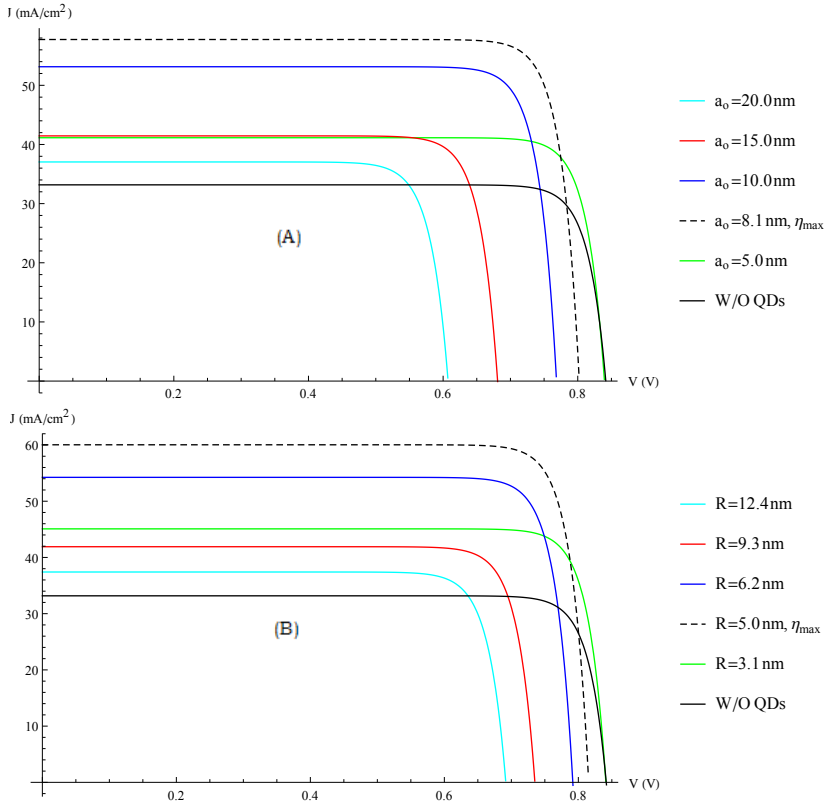

Figure 5.9: JV curve of cubic QD (A) and spherical QD (B) for different QDs size. The current density of a solar cell is defined by Eqns. (4.2.17).

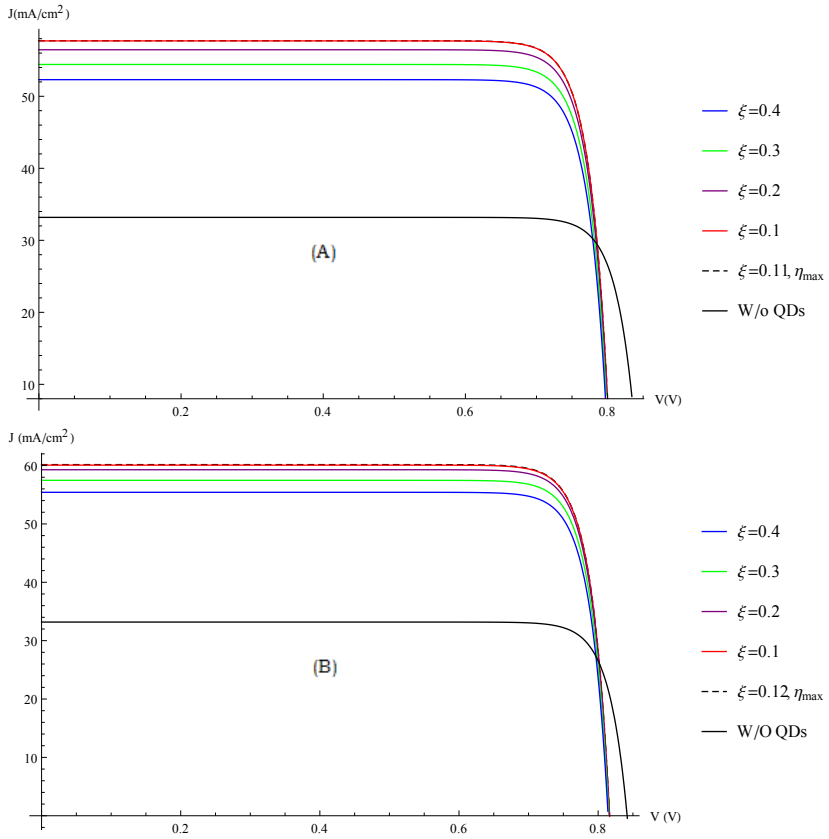

Figure 5.10: JV curve of cubic QD (A) and spherical QD (B) for different QDs size dispersion. The current density of a solar cell is defined by Eqns. (4.2.17).

5.3.4 Efficiency

Figure 5.11 illustrates the effect of both QD average size and QDs size dispersion on QDSC efficiency. The highest η values for cubic QDs obtained within a_o ranging from 7.3 nm to 8.4 nm and ξ ranging from 0.07 to 0.17 (Fig. 5.11A). Similarly, the highest η values for spherical QDs (Fig. 5.11B) are obtained within $\overline{R}$ ranging from 4.3 nm to 5.2 nm, and ξ ranging from 0.07 to 0.2. As a result, there is an optimal range of average QD size and QDs size dispersion to achieve maximum efficiency. Increases outside of this optimal range reduce efficiency. Therefore, to enhance the efficiency of QDSC the optimized size and size dispersion of QD must be chosen.

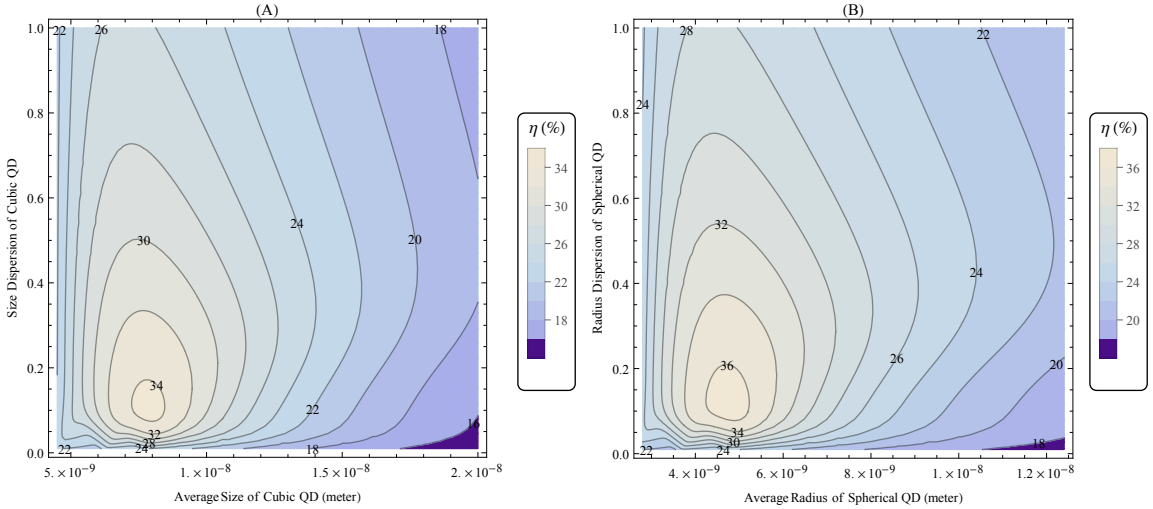

Figure 5.11: QDSC efficiency as functions of average size of QD and QD size dispersion (A) Cubic QDs and (B) Spherical QDs. The efficiency is defined by Eqns. (4.2.25).

To investigate the variation in QDSC efficiency with QDs size, $\xi = 0.1$ was optimized using the optimum range of ξ for achieving maximum efficiency, as shown in Fig. 5.11. Figure 5.12A shows the variation in the efficiency of QDSC with QDs size and it is observed that there is an optimum value of QDs size to get maximum efficiency, which is in good agreement with experimental reports [118, 119, 120, 121, 129]. The variation in the efficiency of QDSC with QDs size can be explained based on the bandgap shift between the barrier and QD. The bandgap shift is small when smaller QDs used and large when

large QDs used. Therefore, photo-generated electrons can be transferred more rapidly from smaller QDs to barrier due to smaller recombination at smaller QD/barrier interface. Small QDs, however, cannot absorb long wavelengths of light, which means less of the solar spectrum can be used. On the other hand, larger QDs absorb long wavelength light, but they are unfavorable for electron escape (transfer) due to larger recombination at larger QD/barrier interface. This competitive relationship between light absorption and electron escape from QD according to the size of the QDs might lead to the optimal QD size to provide maximum solar energy conversion efficiency. The maximum power conversion efficiency of QDSC with cubic QDs ensemble is 34.4% at $a_0 = 8.1\ nm$, and spherical QD ensemble is 36.4% at $\overline{R} = 5.0\ nm$ (Table 5.1). Quantum dot solar cells with spherical QD ensembles have a higher maximum efficiency than quantum dot solar cells with cubic QD ensembles of comparable volume. Hence the efficiency of QDSC can be enhanced by choosing the appropriate shape of QDs. When the average size of a cubic QD exceeds $\sim 15nm$ and the average radius of a spherical QD exceeds $\sim 10.9\ nm$, the efficiencies of QDSCs are lower than that of the reference cell, as illustrated in Fig. 5.12A. It should be noted that $\overline{R} = 0.62a_0$ was used in the prior discussion and Fig. 5.8A for convenience.

To investigate the variation in QDSC efficiency with ξ, a QD size of $a_o = 8.0\ nm$ was optimised using the optimum range of average QD size for achieving maximum efficiency, as shown in Fig. 5.11. Figure 5.12B shows the variation of the efficiency of QDSC with ξ of QDs. There is an optimum QD ξ to provide maximum power conversion efficiency. The higher efficiencies (Table 5.2) of 34.4% and 36.5% can be obtained at $\xi = 0.11$ and $\xi = 0.12$ for QDSC with cubic and spherical QDs, respectively. The variation of QDSC efficiency with ξ agrees with the theoretical model of InAs/GaAs QDSC [88]. The optimized size dispersion can be chosen to enhance the conversion efficiency, but it depends on the dot size. Additionally, for each QDSC with a different QD average size, the maximum conversion efficiency occurs at the particular value of size dispersion. In this theoretical

investigation, Figure 5.12B also shows that the efficiency of QDSC with cubic and spherical QDs is roughly the same for QD size dispersion less than $\sim$ 0.04. Above this value of QD size dispersion, the efficiency of QDSC with spherical QDs is greater than with cubic QDs. As a result, addressing the shape-dependent characteristics of QDSC efficiency is worthless for QD size dispersion less than $\sim$ 0.04. This theoretical investigation demonstrates that optimizing QD size and size dispersion is necessary to achieve the best QDSC power conversion efficiency.

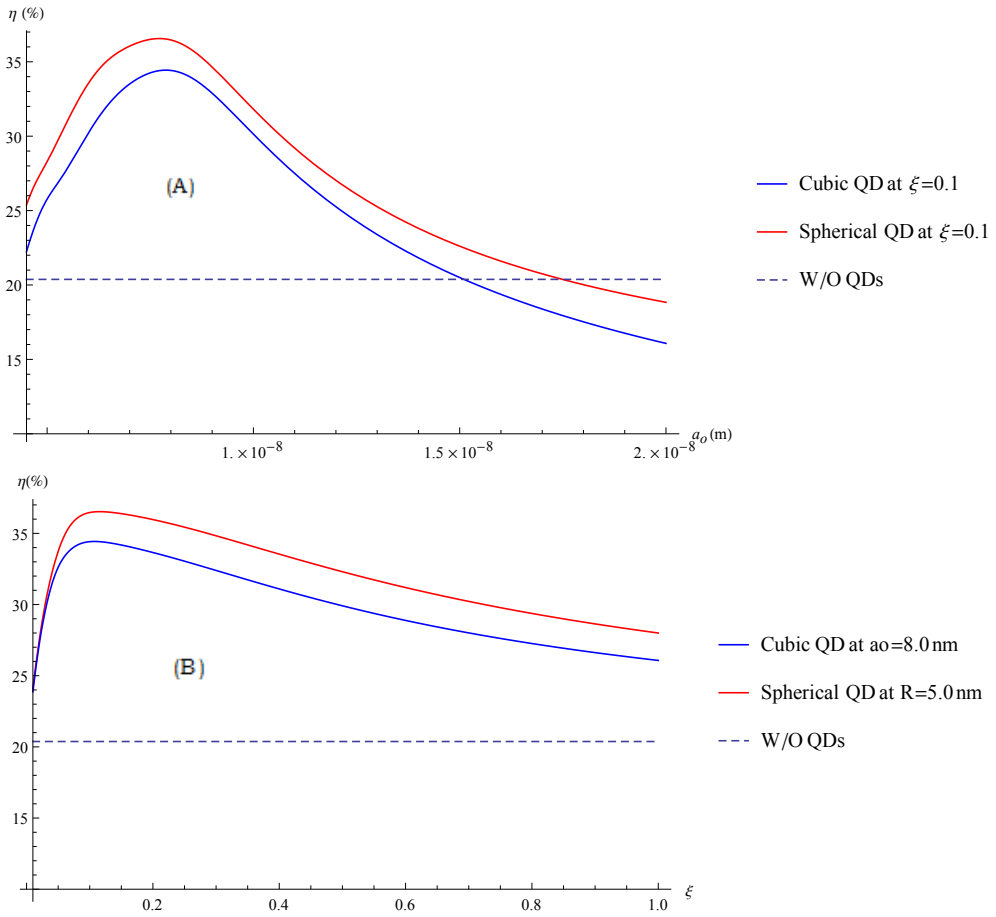

Figure 5.12: Effect of QDs size (A) and QDs size dispersion (B) on the efficiency of QDSC. The efficiency is defined by Eqns. (4.2.25).

Table 5.1: Short circuit current density, open circuit voltage, fill factor and efficiency of solar cell with and without QDs at $\xi = 0.1$.

solar cell	$Size/Radius\ of\ QD\ (nm)$	$J_{sc}\ (mA/cm^2)$	$V_{oc}\ (V)$	F.F (%)	η (%)
With cubic QDs	$a_o = 8.1$	57.6	0.80	86.1	34.4
With spherical QDs	$\overline{R} = 5.0$	60.0	0.82	86.2	36.4
Without QDs	—	33.0	0.84	84.6	20.3

Table 5.2: Short circuit current density, open circuit voltage, fill factor and efficiency of solar cell with cubic QD of size $a_o = 8.0$ nm and spherical QD of radius $\overline{R} = 5.0$ nm.

solar cell	ξ	$J_{sc}\ (mA/cm^2)$	$V_{oc}\ (V)$	F.F (%)	η (%)
With cubic QDs	0.11	57.7	0.80	86.0	34.4
With spherical QDs	0.12	60.2	0.82	86.2	36.5
Without QDs	—	33.0	0.84	84.6	20.3

5.4 Conclusions

A comparative study of the cubic and spherical quantum dots having the same volume was carried out. We have analyzed the effect of quantum dot size and size dispersion (size non-uniformity) on the absorption spectrum of a quantum dot system with a size distribution described by a Gaussian function. It is found that the absorption spectra of the cubic and spherical semiconductor QDs depend strongly on the dot size distribution described by the parameter ξ and the average size of QDs. This theoretical investigation demonstrates that there is an optimum average size and size dispersion of QDs to provide maximum power conversion efficiency. Thus, optimizing QD size and size dispersion is necessary to achieve the best QDSC power conversion efficiency. Inserting InAs QDs in the intrinsic region of GaAs n-i-p solar cell improves the performance of solar cells from 20.3% without QDs to an ideal maximum value of 34.4% (QDSC with cubic QDs ensembles) and 36.5% (QDSC with spherical QDs ensembles). This show that QDSC efficiency depends on the shape of the QD and this particular study shows that maximum QDSC efficiency is obtained for spherical shaped QD in comparison with cubic shape QD. The results of this theoretical model of an InAs/GaAs quantum dot solar cell can be used for experimental research on QDSCs as well as in the design and fabrication of better-performance solar cell panels.

Chapter 6

The Impact of Inserting an $InAs$ Quantum Dot in the Middle Subcell of a Triple junction $Ga_{0.51}In_{0.49}P/GaAs/Ge$ Solar Cell

6.1 Introduction

Semiconductor solar cells have been widely investigated as a device for generating electrical power directly from sun-light. One of the most common approaches to avoid spectral loss in solar cells is to use multi-junction solar cell (MJSC) approach [13, 20]. Multi-junction solar cells are solar cells with multiple p–n junctions made of different semiconductor materials connected via tunnel junctions [20]. The approach is based on the idea to build a stack of solar cells of different bandgaps to absorb larger portion of the solar spectrum to raise the efficiency of solar cells [13]. Multi-junction solar cell approach has a capacity to overcame the most important losses in single junction solar cell. Some of the advantages of multi-junction solar cell approach are:- 1) Effectively collecting sunlight, which has a wide-range spectrum from ultraviolet to infrared [31]. 2) Can reduce thermalization loss due to a high-energy photon absorbed by a small-bandgap material [13].

In MJSC, the topmost subcell with highest energy gap absorb photons at and above its bandgap [13]. This way it will absorb higher energy photons whose energy would be

dominantly converted to heat if absorbed by low bandgap subcells [130]. On the other hand, transmits the less energetic photons to the solar cells below, thus subcells with lower energy gap absorb them efficiently. This leads to the division of solar spectrum and each part is absorbed by different subcell specially optimized for those energies [130].

The strong demand for higher efficiency photovoltaic has recently attracted considerable interest in multi-junction solar cells based on III-V semiconductors [131]. First, they can be grown with excellent material quality and their bandgaps span a wide spectral range [132]. Second, they are capable of generating approximately twice as much power under the same conditions as traditional solar cells, depending on a particular technology [131]. Unfortunately, multi-junction solar cells are very expensive, so they are mainly used in high performance applications such as satellites at present [131].

The most widely fabricated MJSC today is triple-junction GaInP/GaAs/Ge. In this case, Ge (E_g=0.66 eV) serves as a substrate on which GaAs (E_g= 1.4 eV) and GaInP (E_g = 1.8-1.88 eV) subcells are grown. The highest efficiency this device can achieve is 34.1% under one-sun illumination and 41.6% under 364 suns. Highly mature lattice-matched design has achieved 40.1% efficiency at 135 suns concentration using $Ga_{0.5}In_{0.5}P$, $Ga_{0.98}In_{0.02}As$, and Ge junctions with the band gap combination of 1.86, 1.39, and 0.67 eV [133]. The efficiency would be higher if the energy gaps could be chosen more optimally. In this configuration, the lowest subcell generates current around twice as high as the two upper subcells, due to low energy gap in Ge. The device is not optimally current matched due to restrictions in lattice constants and energy gaps. Either way, Ge-based subcell increases V_{oc} by $\sim$ 250 mV [130].

Among the numerous technologies used to improve the conversion efficiency of solar cells, the multi-junction (M-J) concept, especially the triple-junction (3-J) concept based on InGaP, GaAs and Ge materials exhibit high efficiencies. Nevertheless, their performance is somehow restricted due to current limitation of the GaAs middle cell and lattice mismatch of Ge substrate [44, 45, 46].

Many approaches have been proposed to overcome those limitations and enhance the conversion efficiency of the 3-J configurations. The first approach consists in inserting a fourth subcell with a bandgap energy about 1 eV in order to absorb the photons which have a bandgap energy between 1.42 eV (GaAs) and 0.67 eV (Ge). InGaAsN is then a good candidate thanks to its lattice matched to Ge substrate and to its tunable bandgap energy. Theoretical calculations have indicated that such structures provide a conversion efficiency of about 47.7 % [45]. The second approach adding a second Ge subcell to the InGaP/GaAs/Ge multi-junction such that absorption of the near infrared spectrum is divided between two Ge subcells rather than one [46]. The resulting four junction InGaP/GaAs/Ge/Ge device benefits from an increased open circuit voltage as contributed by the second Ge subcell. Experimental report of this approach indicated that an improved efficiency from 26.5% to 28.0% . The third approach consists of inserting an intermediate band in the 3-J structure [45]. Aim is then to improve the spectral response of the solar cell in the energy region below the absorption edge of host material. Luque et al have been the first who proposed to insert multiple layers of InAs quantum dots (QDs) in GaAs subcell as an intermediate band [22].

Inserting InGaAsN subcell between GaAs and Ge subcells or inserting additional thin Ge subcell to form four junction solar cell will not improve the short circuit current of MJSC because the short circuit current is limited by GaAs subcell, but it improves the open circuit voltage and the efficiency of MJSC. On the other-hand, inserting optimized size of InAs QDs in the intrinsic region of n-i-p GaAs subcell could bring both current match and short circuit current improvement in triple junction QDSC. Due to the insertion of QDs open circuit voltage loss is expected. However, inserting QDs could result a better efficiency improvement compared to four junction solar cell. InAs QDs could be a potential candidate to overcame this current limitation problem in the middle subcell (GaAs).

In this study, we modeled n/p $Ga_{0.51}In_{0.49}P$ as a top subcell, n-i-p GaAs with InAs QDs in the intrisic region of GaAs as the middle subcell and n/p Ge as a bottom subcell. The

advantage of selecting $Ga_{0.51}In_{0.49}P$ as top cell is due to its wide band gap (1.86 eV) it has a capability of absorbing mostly the short-wavelength part of the solar spectrum and transparent to the light of longer wavelength which are absorbed more effectively by the GaAs (1.424 eV) middle cell [44] and Ge (0.66 eV) bottom cell and provide higher open circuit voltage to the triple-junction quantum dot solar cell. In addition $Ga_{0.51}In_{0.9}P$ lattice matched to GaAs [13, 134, 135], as a result generation of misfit dislocations which form recombination sites (a loss mechanism) can be avoided [135]. The misfit-dislocations were found to influence not to short circuit current but to open circuit voltage of the cell [136]. Germanium is suitable as a substrate material for this devices due to near lattice match with GaAs (0.08% lattice-mismatch) [136], favorable mechanical properties [46] and a slight voltage increase [13]. Triple-junction (3J) cell structure without and with InAs(QD)/GaAs(barrier) periods in the GaAs middle cell is modeled, simulated and optimized. Our objective is to insert the maximum number of InAs quantum dot layers to carry out intermediate bands energy in order to absorb the photons which have an energy lower than the bandgap of GaAs ($E_{photon} < E_g$) and improve the short circuit current to match with the top cell and improve the power conversion efficiency. Already the efficiency of the 3J structure increases considerably compared to a single solar cell. The creation of intermediate energy bands causes a more significant increase than a 3J solar cell.

A theoretical model of $Ga_{0.51}In_{0.49}P/GaAs/Ge$ triple-junction quantum dot solar cells (3J-QDSC) is developed using $InAs/GaAs$ QDSC as a middle subcell in Section 6.2. Section 6.3 presents the numerical optimization of the size of $InAs$ QD in the middle subcell, doping concentration and thickness of the top and the bottom subcells. The detail analysis of the impact of inserting $InAs$ QD in the middle subcell of 3J-QDSC is also presented in Section 6.3. Our findings concluded in Section 6.4.

6.2 Model

Figure 6.1 shows the model of $Ga_{0.51}In_{0.49}P/GaAs/Ge$ triple junction quantum dot solar cell (3J-QDSC). The cell's overall layer structure consists of two np-junctions, one n-i-p QDSC, and two tunnel junctions between the subcells. The three subcells were linked in series via two highly doped and ultra-thin tunnel junctions, which are favorable for a low resistance and high current density [137]. The device used both an AlGaAs/GaInP wide band gap tunnel junction and a GaAs/GaAs narrow band gap tunnel junction [138], as shown in Fig. 6.1. $InAs$ QDs is inserted only in the intrinsic region of $GaAs$ subcell (middle subcell). For each subcell, photogenerated carriers in n- and p-regions are collected

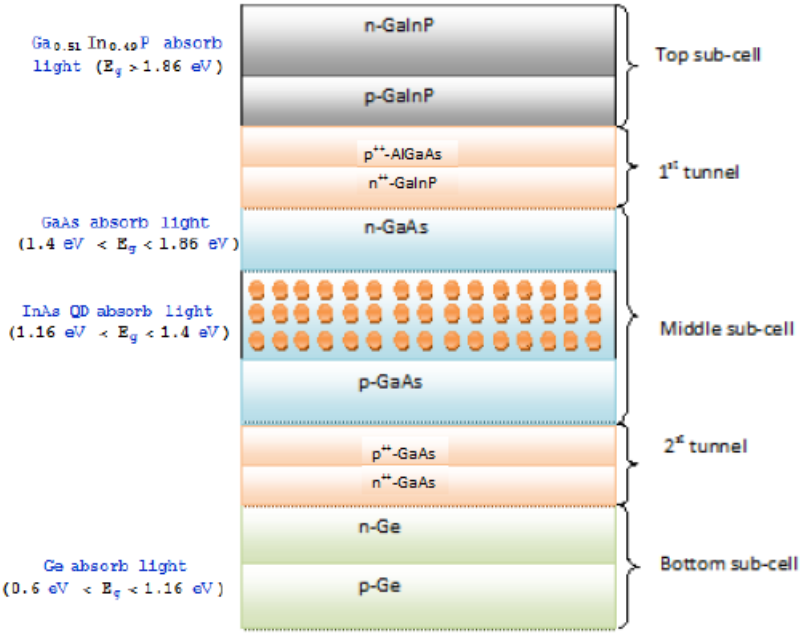

Figure 6.1: Triple junction quantum dot solar cell model.

by a diffusion process while that in the i-region by drift process. We divide the collection of photogenerated carriers in three regions: the top neutral region, the depletion region of the junction, and the substrate neutral region. The short circuit current density for the top and bottom subcells is the sum of Eqns. (2.7.8), (2.7.16), and (2.7.21) and for the middle subcell it is expressed by Eqn. (4.2.16). The total reverse saturated current

density for the top and bottom subcells is the sum of Eqns. (2.8.12) and (2.8.15) and for the middle subcell it is the sum of Eqns. (4.2.20) and (4.2.21).

For multi-junction solar cell the optimal current density in the m^{th} subcell is

$$J_{opt}^{(m)} = J_{sc}^{(m)} - J_o^{(m)}\left[\exp\left(\frac{qV_{opt}^{(m)}}{K_BT}\right) - 1\right]. \tag{6.2.1}$$

Written differently, the optimal voltage in the m^{th} subcell is

$$V_{opt}^{(m)} = \frac{K_BT}{q}\ln\left[\frac{J_{sc}^{(m)} - J_{opt}^{(m)}}{J_o^{(m)}} + 1\right]. \tag{6.2.2}$$

In series constrained multi-junction solar cell with M subcells

$$V_{opt} = \sum_{m=1}^{M} V_{opt}^{(m)}, \tag{6.2.3}$$

and

$$J_{opt}^{(1)} = J_{opt}^{(2)} = ... = J_{opt}^{(M)} = J_{opt}. \tag{6.2.4}$$

Therefore

$$V_{opt} = \sum_{m=1}^{M} \frac{K_BT}{q}\ln\left[\frac{J_{sc}^{(m)} - J_{opt}}{J_o^{(m)}} + 1\right], \tag{6.2.5}$$

where V_{opt} and J_{opt} are the optimal voltage and current density of MJSC, respectively. Equation (6.2.5) can be solved numerically to determine the relationship between current density and voltage in the MJSC. As a result, the open circuit voltage of MJSC is the sum of the open circuit voltages of each individual subcell, and the short circuit current density of MJSC is the least short circuit current density of the subcells.

6.3 Result and Discussion

Physical parameters used in this study are shown in Tables 6.1 and 6.2. The absorption coefficients of Ge [139], GaAs [51], and $Ga_{1-x}In_xP$ [52] are calculated using Eqns. (6.3.1), (6.3.2), and (6.3.3), respectively.

$$\alpha_{Ge} = \frac{1.9\sqrt{E - E_g}}{E}, \tag{6.3.1}$$

$$\alpha_{GaAs} = \frac{5.1\sqrt{E - E_g}}{E}, \tag{6.3.2}$$

$$\alpha_{GaInP} = 5.5\sqrt{E - E_g} + 1.5\sqrt{E - E_g - 0.1}, \tag{6.3.3}$$

where E is the photon's energy, and E_g is the energy band gap. When the unit is taken as eV, unit of α will be determined to be $1/\mu m$.

Table 6.1: The parameters used in calculations. Note that "SRV" stands for surface recombination velocity and "O" stands for optimized values in Subsections 6.3.1 and 6.3.2.

Parameters	Unit	$Ga_{0.51}In_{0.49}P$ [131]	GaAs [91]	Ge [52]
Electrons SRV (S_n)	cms^{-1}	1×10^6	6×10^3	1×10^4
Holes SRV (S_p)	cms^{-1}	1×10^6	6×10^3	1×10^4
Electron diffusion length (L_n)	μm	3.7	2.0	53.0
Hole diffusion length (L_p)	μm	0.6	3.0	8.8
Electrons diffusion constant (D_n)	cm^2s^{-1}	29.39	220.0	22.86
Holes diffusion constant (D_p)	cm^2s^{-1}	1.03	10.0	10.71
Band gap (E_{gB})	eV	1.86	1.424	0.66
Acceptor concentration (N_A)	cm^{-3}	1.5×10^{17} [O]	1×10^{17}	1×10^{17} [O]
Donor concentration (N_D)	cm^{-3}	2×10^{18} [O]	2×10^{18}	2×10^{18} [O]
n-region length (X_j)	μm	0.1 [O]	0.8	1.0 [O]
p-region length ($H^{'}$)	μm	1.5 [O]	2.0	2.5 [O]
i-region width (W_D)	μm	-	3.0	-

Table 6.2: The optimized parameters used in calculations for $InAs$ QD.

Parameters	Unit of measure	InAs QDs
Size of QDs(a_o)	nm	4.93
Barrier width(b)	nm	10.0
QDs volume (V_D)	cm^3	1.2×10^{-19}
QDs areal density (A_D)	cm^{-2}	4.5×10^{11}
QDs volume density (n_D)	cm^{-3}	3.0×10^{17}
number of layers		200

6.3.1 Optimizing the Size of InAs QDs and the Doping Concentration of Subcell-1 and Subcell-3

To achieve the current density match among the three subcells, the size of InAs QD in subcell-2 (n-i-p InAs/GaAs) and the doping concentration in subcell-1 (n/p $Ga_{0.51}In_{0.49}P$) and subcell-3 (n/p Ge) has to be optimized. In both Fig. 6.2(A) and 6.2(B) the current density match among the three subcells achieved at $a_o = 4.93\,nm$ size of the $InAs$ QD. The donor concentration (N_D) in subcell-1 is optimized at three different doping concentration ($N_D = 2.0 \times 10^{17}$, 2.0×10^{18}, and $2.0 \times 10^{19}\ cm^{-3}$) keeping $N_A = 1.5 \times 10^{17}\ cm^{-3}$. The current density match is achieved at $N_D = 2.0 \times 10^{18}\ cm^{-3}$ (Fig. 6.2(A)). The acceptor concentration (N_A) in subcell-1 is optimized at three different doping concentration ($N_A = 1.0 \times 10^{17}$, 1.5×10^{17}, and $2.0 \times 10^{17}\ cm^{-3}$) keeping $N_D = 2.0 \times 10^{18}\ cm^{-3}$. The current density match is achieved at $N_A = 1.5 \times 10^{17}\ cm^{-3}$ (Fig. 6.2(B)). In both Figs. 6.2(A) and 6.2(B) the donor (N_D) and acceptor (N_A) concentrations in subcell-3 have no significant effect for the current matching among the three subcells. But the three subcells current density match at $N_D = 2.0 \times 10^{18}\ cm^{-3}$ (Fig. 6.2(A)) and $N_A = 1.0 \times 10^{17}\ cm^{-3}$ (Fig. 6.2(B)) of subcell-3. The current density of subcell-3 is highly affected by the size of $InAs$ QD. It is clearly seen that the current density of subcell-3 decreases as the size of $InAs$ QD increases.

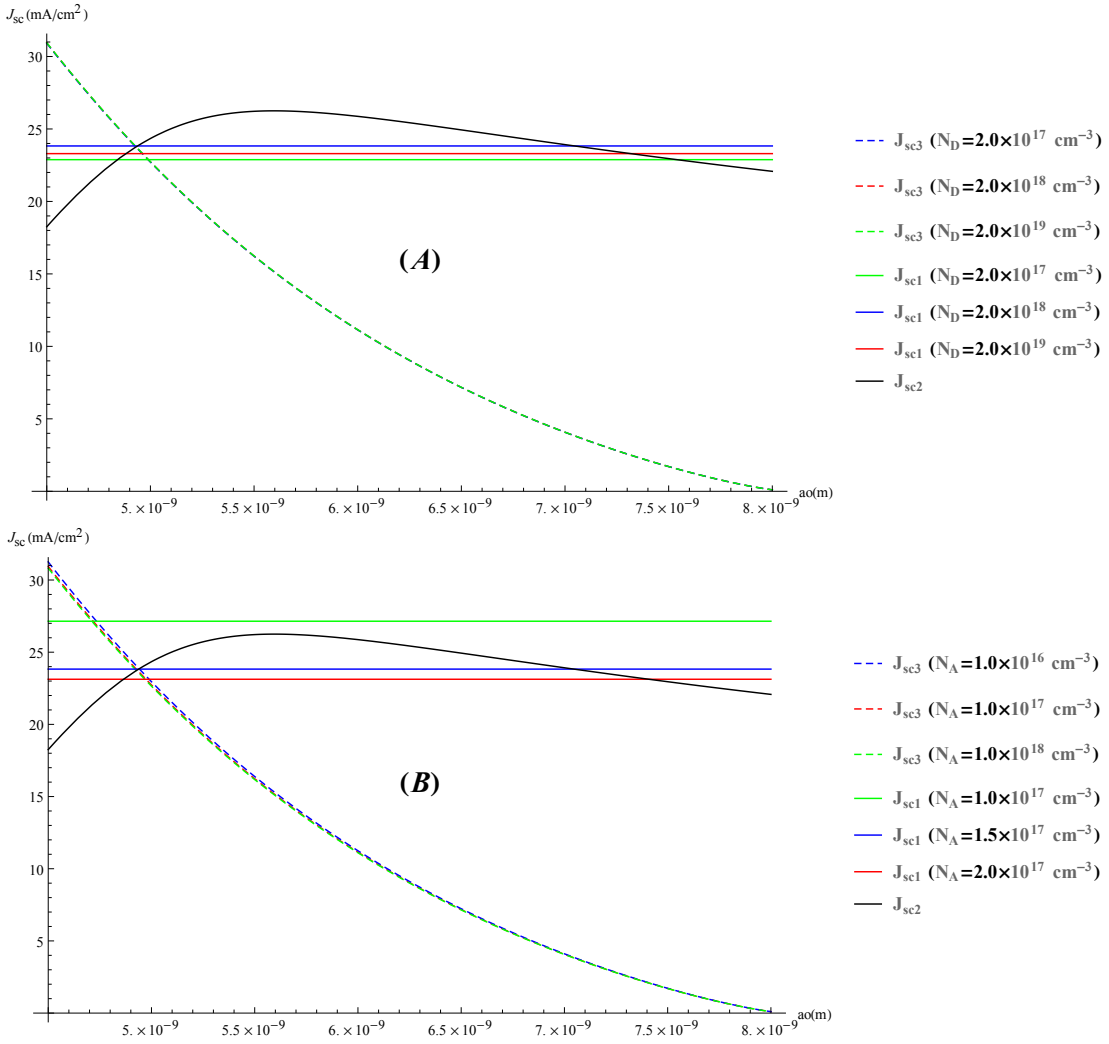

Figure 6.2: Optimizing the size of InAs QD and the doping concentration of subcell-1 and subcell-3 depicted in (A) N_D and (B) N_A.

6.3.2 Optimizing the Emitter and the Base Thickness of Subcell-1 and Subcell-3

It is mandatory to optimize the thickness of subcells to achieve current density match among subcells in the modeling of multi-junction solar cells. Figure 6.3 shows that the optimized emitter and base thickness of subcell-1 and subcell-3. The emitter thickness of subcell-1 is optimized at $W_n = 0.1,\ 0.15,\ and\ 0.2\ \mu m$ keeping $W_p = 1.5\ \mu m$ (Fig. 6.3(A)). It is observed that the current match among the three subcells achieved at $W_n = 0.1\ \mu m$.

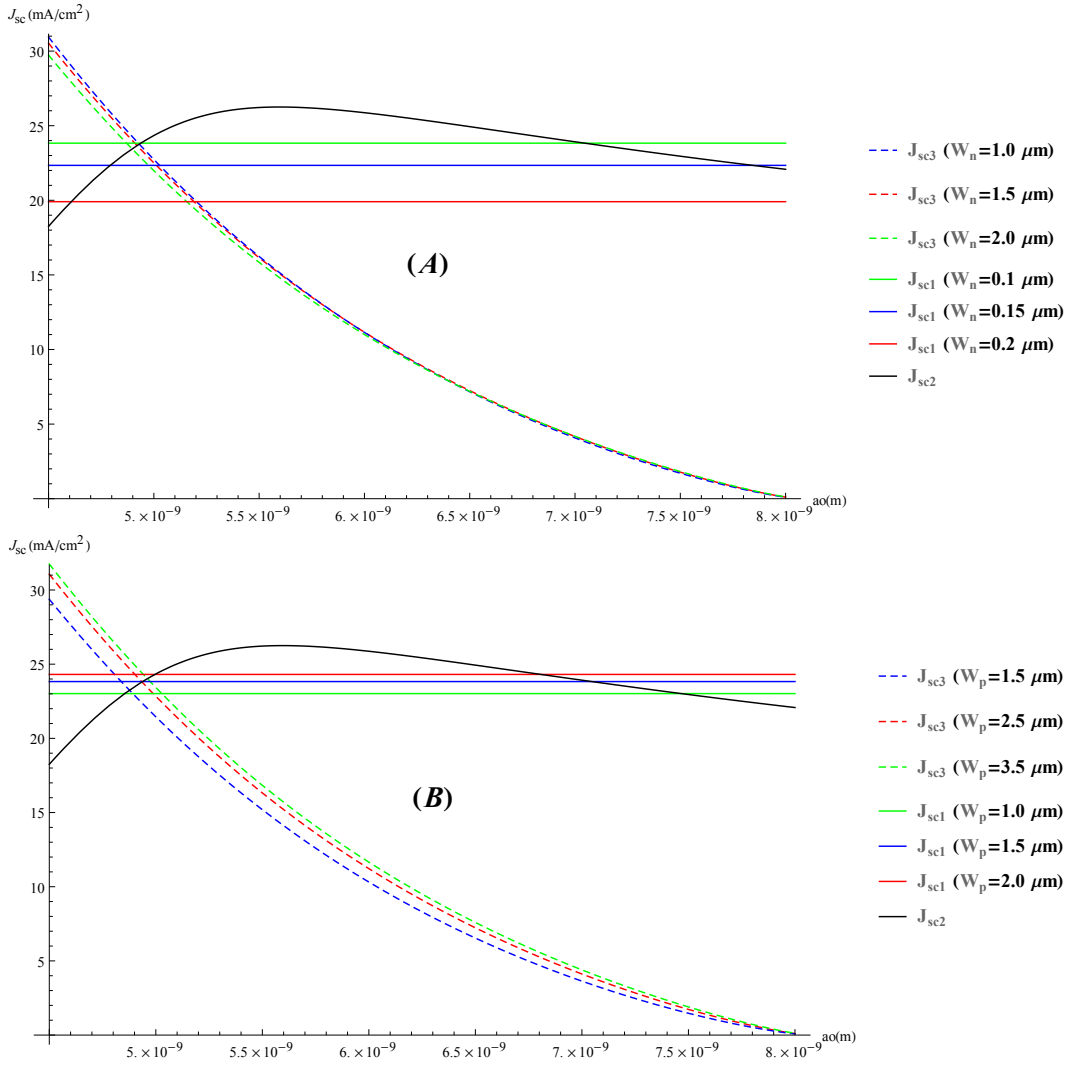

Figure 6.3: Optimizing (A) the emitter and (B) the base thickness of subcell-1 and subcell-3.

Similarly, the base thickness of subcell-1 is optimized at $W_p = 1.0,\ 1.5,\ and\ 2.0\ \mu m$ keeping $W_n = 0.1\ \mu m$ (Fig. 6.3(B)). The current match among the three subcells achieved at $W_p = 1.5\ \mu m$. For subcell-3 the current match achieved at $W_n = 1.0\ \mu m$ (Fig. 6.3(A)) and $W_p = 2.5\ \mu m$ (Fig. 6.3(B)).

The current match among these subcells is achieved only at $a_o = 4.93\ nm$ InAs QD. Below $a_o = 4.93\ nm$ InAs QD size, current density of subcell-3 is higher than subcell-1 and subcell-2 and when the size of InAs QD is greater than $a_o = 4.93\ nm$, then the current density of subcell-3 is smaller than subcell-1 and subcell-2 as shown in Figs. 6.2 and 6.3. The dependency of subcell-3 current density on the size of InAs QD of subcell-2 is explained by the energy band gap of InAs QD and the range of solar spectrum reaching subcell-3. Smaller size InAs QD have larger energy band gap, therefore large portion of low energy solar spectrum reach subcell-3 to generate electron-hole pair which result in higher current density in subcell-3. On the other hand, large size InAs QD have smaller energy ban gap, therefore small portion of low energy solar spectrum reach subcell-3 to generate electron-hole pair which result in smaller current density in subcell-3.

6.3.3 Current Density-Voltage Characteristics for Triple-Junction Solar Cell (3J-SC) Without QDs

First, we investigated a triple-junction solar cell based on $Ga_{0.51}In_{0.49}P/GaAs/Ge$ without InAs QDs. Figure 6.4 shows the evolution of the current density as a function of the voltage of a triple-junction solar cell based on three $Ga_{0.51}In_{0.49}P/GaAs/Ge$ semiconductors. Calculated values of short circuit current, open circuit voltage , fill factor and efficiency are shown in Table 6.3. It is noted that the open circuit voltage V_{oc} of the total cell achieved 2.26 V and the current density J_{sc} does not exceed the 14.7 mA/cm^2 value. The open circuit voltage of the total cell is equal to the sum of the three voltages of each single solar cell. On the other hand, the current density tends towards that of the solar cell which has the low current density. Figure 6.4 clearly indicates that the J_{sc} is limited

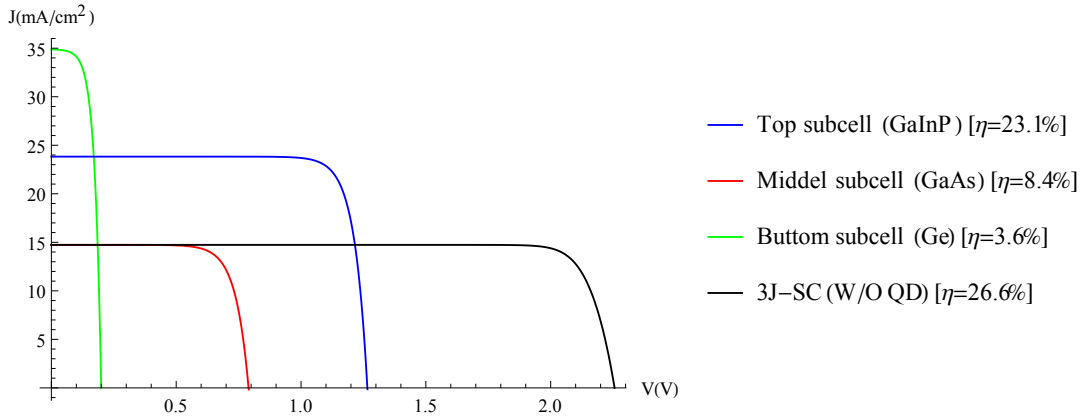

Figure 6.4: JV Curve for 3J-SC with out QDs: Plotted using Eqn. (6.2.5)

by GaAs middle subcell. This is in a good agreement with a theoretical model [44] and an experimental result [46]. However the efficiency of InGaP/GaAs/Ge triple-junction solar cell is improved compared to the other three subcells (Table 6.3).

Table 6.3: Short circuit current, open circuit voltage, fill factor and efficiency of 3J-SC with out InAs QD.

Solar cell	$J_{sc}(mA/cm^2)$	$V_{oc}(V)$	$FF(\%)$	$\eta(\%)$
Sub Cell-1	23.8	1.27	88.7	23.1
Sub Cell-2	14.7	0.79	83.9	8.4
Sub Cell-3	34.9	0.2	60.1	3.6
3J-SC(W/O QDs)	14.7	2.26	92.8	26.6

6.3.4 Current Density-Voltage Characteristics of Triple-Junction Quantum Dot Solar Cell (3J-QDSC)

Figure 6.5 shows the evolution of the current density as a function of the voltage of a triple-junction solar cell based on three $Ga_{0.51}In_{0.49}P/GaAs/Ge$ semiconductors with InAs QDs embedded in the intrinsic region of middle subcell (GaAs). Calculated values of short circuit current density, open circuit voltage , fill factor and efficiency are shown in Table 6.4. Inserting InAs QDs result in a considerable increase in the short circuit current density from 14.7 to 23.8 mA/cm^2, that is to say there is a gain of 61.9%. Inserting InAs QDs

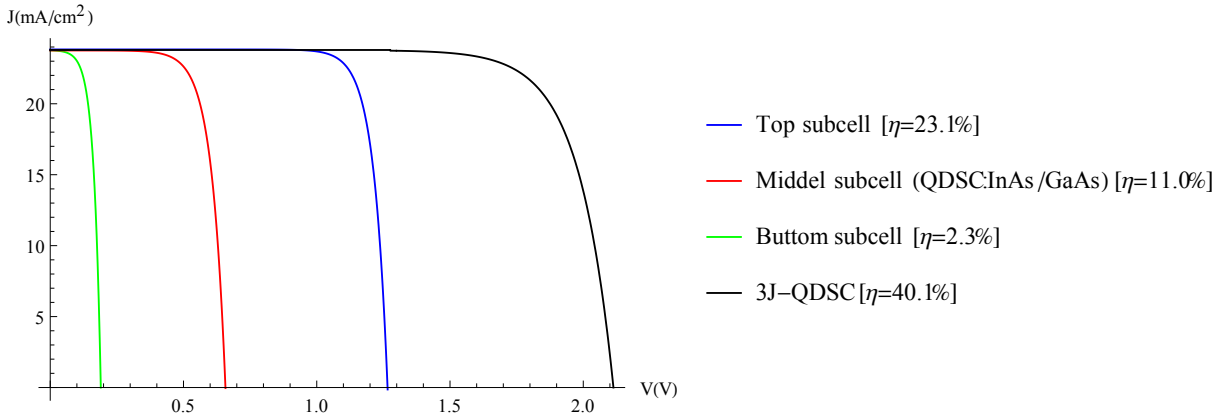

Figure 6.5: JV Curve for 3J-QDSC with InAs QDs: Plotted using Eqn. (6.2.5)

decreases the open circuit voltage with insignificant amount. The V_{oc} voltage decreases from 2.26 to 2.1 V. An open circuit voltage loss of $\delta V_{oc} = 0.16$ V is detected. The impact of incorporating InAs QDs on the open circuit voltage is opposite to that of the current density. It can be seen that the effect of the InAs QDs on the open circuit voltage is very small compared to the current density. Inserting InAs QDs causes a considerable increase in the efficiency from 26.6 % to 40.1 %, that is to say there is an increase efficiency of 50.8% (shown in Table 6.4).

Figure 6.6 shows the current density-voltage characteristic curves for 3J-QDSC, 3J-SC ($Ga_{0.51}In_{0.49}P/GaAs/Ge$), 4J-SC ($Ga_{0.51}In_{0.49}P/GaAs/Ge/Ge$), and 3J-SC using detailed balance theory ($Ga_{0.51}In_{0.49}P/GaAs/Ge$). It shows that inserting thin Ge as a forth sub-

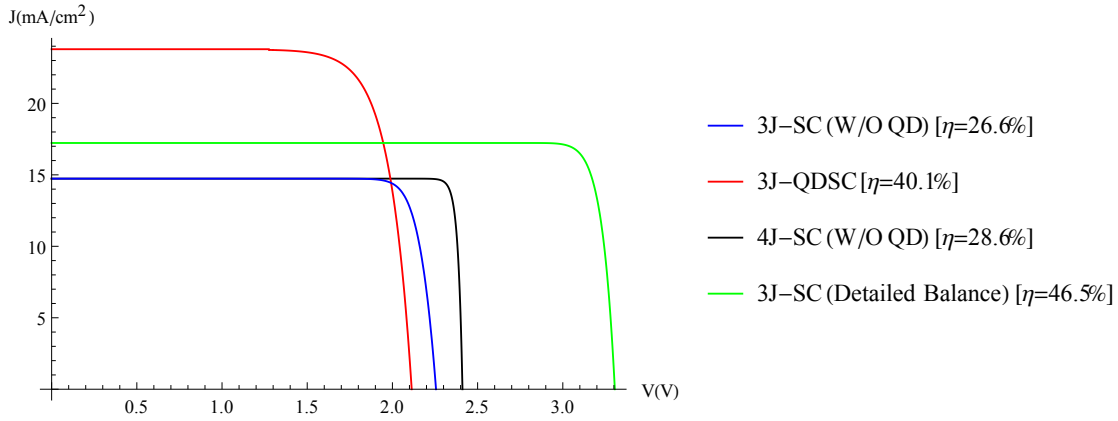

Figure 6.6: JV Curve for 3J-SC, 3J-QDSC, 3J-SC (detailed balance limit), and 4J-SC: Plotted using Eqn. (6.2.5)

cell improves the open circuit voltage but the short circuit current is still limited by GaAs subcell. However the power conversion efficiency of four junction solar cell is better than three junction solar cell. Inserting InAs QDs in the i-region of GaAs subcell improves the short circuit current the solar cell by a significant amount but there is a small degradation of open circuit voltage and a large improvement of efficiency compared to the four junction solar cell. In addition, Fig. 6.6 also illustrates that the power conversion efficiency of our 3J-QDSC model is 6.4 unit lower than the detailed balance limit of $Ga_{0.51}In_{0.49}P/GaAs/Ge$ triple junction solar cells.

Table 6.4: Short circuit current, open circuit voltage, fill factor and efficiency of 3J-QDSC.

Solar cell	$J_{sc}(mA/cm^2)$	$V_{oc}(V)$	$FF(\%)$	$\eta(\%)$
Sub Cell-1	23.8	1.27	88.7	23.1
Sub Cell-2	23.8	0.66	81.6	11.0
Sub Cell-3	23.8	0.2	58.9	2.3
3J-QDSC	23.8	2.1	92.4	40.1

6.4 Conclusion

In this Chapter we have investigated the insertion of InAs QDs in the middle subcell of triple-junction $Ga_{0.51}In_{0.49}P/GaAs/Ge$ solar cell on the power conversion efficiency of the solar cell. Inserting InAs QDs in triple-junction $Ga_{0.51}In_{0.49}P/GaAs/Ge$ solar cell causes a considerable increase in the current density from 14.7 to 23.8 mA/cm^2, which is a relative enhancement of about 61.9%, and insignificant degradation in open circuit voltage. In the same conditions inserting InAs QDs improves the power conversion efficiency from 26.6% to 40.1%, which is a relative enhancement of about 50.8%. Therefore, inserting InAs QDs ensembles in the i-region of GaAs of the triple-junction $Ga_{0.51}In_{0.49}P/GaAs/Ge$ solar cell improves both the short-circuit current density and efficiency without significant degradation in the open circuit voltage.

Chapter 7

Summary and Recommendations

This chapter provides a summary of the research conducted in this thesis to enhance comprehension of solar cell physics, specifically in the context of $InAs/GaAs$ quantum dot solar cells using the $n^+ - i - p^+$ solar cell structure. This study has some limitations that are highlighted. Additionally, a brief discussion of recommendations for potential future work is included in order to advance the development of quantum dot solar cells.

7.1 Summary

The concept of IBSC was proposed in an attempt to utilize sub-bandgap photons and overcome the Shockley-Queisser limit by introducing an IB within the bandgap. A confined levels of quantum dot (QD) was proposed to obtain the operational principles of IBSC. However, there have been many challenges in implementing high efficiency QDSCs. One of the challenges in the practical use of QDSC is figuring out the optimum number of QD layers, QD size, and size dispersion to get high efficiency QDSCs. The goal of this theoretical and numerical study was to address these issues by employing $InAs$ quantum dots inserted in the i-region of $GaAs$ in order to understand more about QDSCs based on $n - i - p$ solar cell structure.

The first part of this thesis investigate how the parameters of the quantum dot solar cell

were affected by the number of quantum dots layers. This study show that the conversion efficiency of the $n-i-p$ structure is significantly improved by embedding $InAs$ QD multilayer into the intrinsic region of $GaAs$. This study indicates that a maximum efficiency of $\eta_{max} = 27.4\%$ can be achieved with an optimal number of quantum dots layers ($n_l = 250$). Increasing the number of QD layers above the optimal value result in a decrease in efficiency.

The second part focuses on investigating the effect of QD size and size dispersion on the absorption coefficient of $InAs$ QD ensembles, QD photocurrent and conversion efficiency of $InAs/GaAs$ QDSC using cubic and spherical $InAs$ QDs of comparable volume. It is observed that the average size of QD and the dot size distribution have a significant influence on the absorption spectra of the spherical and cubic semiconductor QDs. This theoretical and numerical study demonstrated that the maximum quantum dot photocurrent can be obtained at the cubic QD average size of $a_o = 8.1\ nm$ ($J_{QD} = 24.7\ mA/cm^2$) and the spherical QD average radius of $\overline{R} = 5.0\ nm$ ($J_{QD} = 26.9\ mA/cm^2$). This study also shows that for best power conversion efficiency, there is an optimal QD average size and size dispersion. A maximum efficiency of 34.4% is obtained at $a_0 = 8.1\ nm$ and $\xi = 0.11$ for QDSC with cubic QDs ensembles and 36.5% is obtained at $\overline{R} = 5.0\ nm$ and $\xi = 0.12$ for QDSC with spherical QDs ensembles. This indicates that the shape of the QD affects QDSC efficiency, and this specific study demonstrates that, spherical shape QDs yield the highest QDSC efficiency compared to cubic shape QD. Therefore, the maximum possible QDSC power conversion efficiency might be achieved by optimising QD size and size dispersion.

The last part of this study focuses on examining the effect of inserting $InAs$ QDs in the middle subcell on the power conversion efficiency of the $Ga_{0.51}In_{0.49}P/GaAs/Ge$ triple-junction solar cell. The insertion of $InAs$ QDs generates a notable increase in short circuit current density and a slight drop in open circuit voltage. Consequently, the power

conversion efficiency of 3J-QDSC rises from 26.6% to 40.1%, indicating nearly 50.8% improvement when compared to 3J-SC without $InAs$ QDs. The results of this thesis can be used to both the experimental study of QDSCs and the design and manufacturing of solar cell panels with improved performance.

7.2 Limitation of the Study

The main focus of this thesis is the theoretical and numerical investigation of InAs/GaAs QDSC. Furthermore, doing experimental studies with optimised values of number of QD layers, quantum dot size, and size dispersions could provide additional insights into the photogeneration, carrier collection, and recombination processes that occur in real QDSCs.

7.3 Recommendation for Future Work

This thesis's result is not put to the test through experimentation. Reference [36] reports the fabrication of ultra-high stacked QD multi-layers up to 400 QD layers without any dislocations, no crystal defects, or deterioration in crystal quality. In order to comprehend our theoretical and numerical study to be used in real-world solar cell applications, we advise applying the growth method used by Ref. [36] to fabricate an ultra-high stacked multi-layers of InAs/GaAs QDSC using the optimised values of number QD layers, quantum dot size, and size dispersions.

Publications

- Dependence of quantum dot solar dell parameters on the number of quantum dot layers. AIP Advances, **13**(7):07521, 2023. https://doi.org/10.1063/5.0145361.

- Effect of cubic and spherical quantum dot size and size dispersion on the performance of quantum dot solar cells. AIP Advances, **14**(1):015236, 2024. https://doi.org/10.1063/5.0184745.

- The impact of inserting an $InAs$ quantum dot in the middle subcell of a triple junction $Ga_{0.51}In_{0.49}P/GaAs/Ge$ solar cell, manuscript under preparation.

Bibliography

[1] EIA. *International Energy Outlook 2023*. Technical report, The U.S. Energy Information Administration (EIA), October 2023.

[2] IPCC. *Climate Change 2007: The Physical Science Basis*. Cambridge University Press, 2007.

[3] EPIA and Greenpeace International. *Solar generation 6: Solar photovoltaic electricity empowering the world*. European Photovoltaic Industry Association, 2011.

[4] Malgorzata Wiatros-Motyka, Nicolas Fulghum, and Dave Jones. *Global Electricity Review 2024*. Ember, May 2024.

[5] Valerie Chase. *Grand challenges for engineering*. National Academy of Engineering, 2008.

[6] John Perlin. *From space to Earth : The story of solar electricity*. Aatec Publications, 1999.

[7] P. Hersch and K. Zweibel. *Basic photovoltaic principles and methods*. Technical Information Office of Solar Energy Research Institute, 2 1982. http://dx.doi.org/10.2172/5191389.

[8] D. M. Chapin, C. S. Fuller, and G. L. Pearson. A new silicon pn junction photocell for converting solar radiation into electrical power. *Journal of applied physics*, **25**(5):676, 1954. http://dx.doi.org/10.1063/1.1721711.

[9] Kunta Yoshikawa, Hayato Kawasaki, Wataru Yoshida, Toru Irie, Katsunori Konishi, Kunihiro Nakano, Toshihiko Uto, Daisuke Adachi, Masanori Kanematsu, Hisashi

Uzu, and Kenji Yamamoto. Silicon heterojunction solar cell with interdigitated back contacts for a photoconversion efficiency over 26%. *Nature Energy*, **2**:17032–, 2017. http://dx.doi.org/10.1038/nenergy.2017.32.

[10] Hao Lin, Miao Yang, Xiaoning Ru, Genshun Wang, Shi Yin, Fuguo Peng, Chengjian Hong, Minghao Qu, Junxiong Lu, Liang Fang, Can Han, Paul Procel, Olindo Isabella, Pingqi Gao, Zhenguo Li, and Xixiang Xu. Silicon heterojunction solar cells with up to 26.81% efficiency achieved by electrically optimized nanocrystalline-silicon hole contact layers. *Nature Energy*, **8**(8):789–799, August 2023. https://doi.org/10.1038/s41560-023-01255-2.

[11] Armin Richter, Martin Hermle, and Stefan W. Glunz. Reassessment of the limiting efficiency for crystalline silicon solar cells. *IEEE Journal of Photovoltaics*, **3**(4):1184–1191, 2013. http://dx.doi.org/10.1109/JPHOTOV.2013.2270351.

[12] Klaus Jager, Olindo Isabella, Arno H. M. Smets, Rene A. C. M. M. Van Swaaij, and Miro Zeman. *Solar Energy: Fundamentals, Technology, and Systems*. Delft University of Technology, 2014.

[13] Masafumi Yamaguchi, Frank Dimroth, John F. Geisz, and Nicholas J. Ekins-Daukes. Multi-junction solar cells paving the way for super high-efficiency. *Journal of applied physics*, **129**:240901, 2021. https://dx.doi.org/10.1063/5.0048653.

[14] Brendan M. Kayes, Hui Nie, Rose Twist, Sylvia G. Spruytte, Frank Reinhardt, Isik C. Kizilyalli, and Gregg S. Higashi. 27.6% conversion efficiency, a new record for single-junction solar cells under 1 sun illumination. 37^{th} IEEE Photovoltaic Specialists Conference (PVSC), IEEE, 2011. https://doi.org/10.1109/PVSC.2011.6185831.

[15] Motoshi Nakamura, Koji Yamaguchi, Yoshinori Kimoto, Yusuke Yasaki, Takuya Kato, and Hiroki Sugimoto. Cd-free $Cu(In, Ga)(Se, S)_2$ thin-film solar cell with a new world record efficacy of 23.35%. *IEEE Journal of Photovoltaics*, **9**(6):1863–1867, 2019. https://doi.org/10.1109/JPHOTOV.2019.2937218.

[16] Wei Chen, Yudong Zhu, Jingwei Xiu, Guocong Chen, Haoming Liang, Shunchang Liuand Hansong Xue, Erik Birgersson, Jian Wei Ho, Xinshun Qin, Jingyang

Lin, Ruijie Ma, Tao Liu, Yanling He, Alan Man-Ching Ng, and Xugang Guoand Zhubing Heand He Yanand Aleksandra B. Djurisicand Yi Hou. Monolithic perovskite/organic tandem solar cells with 23.6% efficiency enabled by reduced voltage losses and optimized interconnecting layer. *Nature Energy*, **7**(3):229–237, 2022. https://doi.org/10.1038/s41560-021-00966-8.

[17] Hironobu Ozawa, Takahito Sugiura, Takahiro Kuroda, Kouya Nozawa, and Hironori Arakawa. Highly efficient dye-sensitized solar cell based on a ruthenium sensitizer bearing a hexylthiophene modified terpyridine ligand. *Journal of Materials Chemistry A*, 2016. https://doi.org/10.1039/C5TA10393B.

[18] Aswani Yella, Hsuan-Wei Lee, Hoi Nok Tsao, Chenyi Yi, Aravind Kumar Chandiran, Md.Khaja Nazeeruddin, Eric Wei-Guang Diau, Chen-Yu Yeh, Shaik M Zakeeruddin, and Michael Gratzel. Porphyrin-sensitized solar cells with cobalt (II/III)–based redox electrolyte exceed 12 percent efficiency. *Science*, **334**:629, 2011. https://doi.org/10.1126/science.1209688.

[19] Uli Wurfel, Jan Herterich, Mathias List, Jared Faisst, Md Fahmid Matin Bhuyian, Hans-Frieder Schleiermacher, Klara T. Knupfer, and Birger Zimmermann. A $1cm^2$ organic solar cell with 15.2% certified efficiency: Detailed characterization and identification of optimization potential. *Solar RRL*, **5**(4):2000802, 2021. https://doi.org/10.1002/solr.202000802.

[20] Stefan Kremling, Christian Schneider, Sven Hofling, Martin Kamp, and Alfred Forchel. *AlGaInAs Quantum Dots for Intermediate Band Formation in Solar Cell Devices*, volume **15**, chapter 7, pages 167–186. Springer, 2014. http://dx.doi.org/10.1007/978-1-4614-8148-5.

[21] Louise C. Hirst and Nicholas J. Ekins-Daukes. Fundamental losses in solar cells. *Progress in Photovoltaics: Research and Applications*, **19**(3):286–293, https://doi.org/10.1002/pip.1024 2010.

[22] Antonio Luque and Antonio Marti. Increasing the efficiency of ideal solar cells by photon induced transitions at intermediate levels. *Physical review letters*, **78**(26):5014–5017, 1997. http://dx.doi.org/10.1103/PhysRevLett.78.5014.

[23] Rune Strandberg. *Theoretical studies of the intermediate band solar cell*. PhD thesis, Norwegian University of Science and Technology, 2010.

[24] Octavi E. Semonin, Joseph M. Luther, and Matthew C. Beard. Quantum dots for next-generation photovoltaics. *Materials Today*, **15**(11):508–515, 2012. http://dx.doi.org/10.1016/S1369-7021(12)70220-1.

[25] Graham H. Carey, Larissa Levina, Riccardo Comin, Oleksandr Voznyy, and Edward H. Sargent. Record charge carrier diffusion length in colloidal quantum dot solids via mutual dot-to-dot surface passivation. *Advanced Materials*, **27**(21):3325–3330, 2015. http://dx.doi.org/10.1002/adma.201405782.

[26] A. Marti, L. Cuadra, and A. Luque, editors. *Quantum Dot Intermediate Band Solar Cell*. 28^{th} IEEE Photovoltaic Specialists Conference, IEEE, 2000. http://dx.doi.org/10.1109/pvsc.2000.916039.

[27] I. Tobias, A. Luque, E. Antolin, P. Garcia-Linares, I. Ramiro, E. Hernández, and A. Marti. Realistic performance prediction in nanostructured solar cells as a function of nanostructure dimensionality and density. *Journal of applied physics*, **112**(12):124518, 2012. http://dx.doi.org/10.1063/1.4770464.

[28] A. Luque, A. Marti, N. Lopez, E. Antolin, and E. Canovas. Experimental analysis of the quasi-fermi level split in quantum dot intermediate-band solar cells. *Journal of applied physics*, **87**:083505, 2005. http://dx.doi.org/10.1063/1.2034090.

[29] N. Lopez, A. Marti, A. Luque, C. Stanley, C. Farmer, and P. Diaz. Experimental analysis of the operation of quantum dot intermediate band solar cells. *Journal of Solar Energy Engineering*, **129**(3):319–322, 2007. http://dx.doi.org/10.1115/1.2735344.

[30] A. Luque and A. Marti. General equivalent circuit for intermediate band devices: Potentials, currents and electroluminescence. *Journal of applied physics*, **96**(1):903–909, 2004. http://dx.doi.org/10.1063/1.1760836.

[31] Toshiyuki Sameshima, Jun Takenezawa, Masahiko Hasumi, Takashi Koida, Tetsuya Kaneko, Minoru Karasawa, and Michio Kondo. Multi junction solar cells stacked

with transparent and conductive adhesive. *Japanese Journal of Applied Physics*, **50**:052301, 2011. https://dx.doi.org/ 10.1143/JJAP.50.052301.

[32] Arno Smets, Klaus Jager, Olindo Isabella, Rene van Swaaij, and Miro Zeman. *Solar energy: The physics and engineering of photovoltaic conversion, technologies and systems*. UIT Cambridge, England, 2015.

[33] S. A. Blokhin, A. V. Sakharov, A. M. Nadtochy, A. S. Pauysov, M. V Maximov, N. N. Ledentsov, A. R. Kovsh, S. S. Mikhrin, V. M. Lantratov, S. A. Mintairov, N. A. Kaluzhniy, and M. Z. Shvarts. AlGaAs/GaAs photovoltaic cells with an array of InGaAs QDs. *Semiconductors*, **43**(4):514–518, 2009. https://doi.org/10.1134/S1063782609040204.

[34] C. G. Bailey, D. V. Forbes, R. P. Raffaelle, and S. M. Hubbard. Near 1 V open circuit voltage InAs/GaAs quantum dot solar cells. *Applied Physics Letters*, **98**(16):163105, 2011. http://dx.doi.org/10.1063/1.3580765.

[35] Denis Guimard, Ryo Morihara, Damien Bordel, Katsuaki Tanabe, Yuki Wakayama, Masao Nishioka, and Yasuhiko Arakawa. Fabrication of InAs/GaAs quantum dot solar cells with enhanced photocurrent and without degradation of open circuit voltage. *Applied Physics Letters*, **96**(20):203507, 2010. http://dx.doi.org/10.1063/1.3427392.

[36] Takeyoshi Sugaya, Osamu Numakami, Ryuji Oshima, Shigenori Furue, Hironori Komaki, Takeru Amano, Koji Matsubara, Yoshinobu Okano, and Shigeru Niki. Ultra-high stacks of InGaAs/GaAs quantum dots for high efficiency solar cells. *Energy and Environmental Science*, **5**(3):6233–6237, 2012. http://dx.doi.org/10.1039/c2ee01930b.

[37] A. Luque, N. Lopez A. Marti, E. Antolin, E. Canovas, C. Stanley, C. Farmer, and P. Diaz. Operation of the intermediate band solar cell under nonideal space charge region conditions and half filling of the intermediate band. *Journal of Applied Physics*, **99**:094503, 2006. http://dx.doi.org/10.1063/1.2193063.

[38] T. Sugaya, S. Furue, H. Komaki, T. Amano, and M. Mori. Highly stacked and well-aligned $In_{0.4}Ga_{0.6}As$ quantum dot solar cells with $In_{0.2}Ga_{0.8}As$ cap layer. *Applied Physics Letters*, **97**:183104, 2010. http://dx.doi.org/10.1063/1.3507390.

[39] Seth M. Hubbard, Chelsea Plourde, Zac Bittner, Christopher G. Bailey, Mike Harris, Tim Bald, Mitch Bennett, David V. Forbes, and Ryne Raffaelle, editors. *InAs quantum dot enhancement of GaAs solar cells*. 35^{th} Photovoltaic Specialists Conference, IEEE, 2010. http://dx.doi.org/10.1109/PVSC.2010.5614053.

[40] T. Sugaya, Y. Kamikawa, S. Furue, T. Amano, M. Mori, and S. Niki. Multi-stacked quantum dot solar cells fabricated by intermittent deposition of InGaAs. *Solar Energy Materials and Solar Cells*, **95**(1):163–166, 2011. https://doi.org/10.1016/j.solmat.2010.04.040.

[41] F. K. Tutu, I. R. Sellers, M. G. Peinado, C. E. Pastore, S. M. Willis, A. R. Watt, T. Wang, and H. Y. Liu. Improved performance of multilayer InAs/GaAs quantum-dot solar cells using a high-growth-temperature GaAs spacer layer. *Journal of Applied Physics*, **111**(4):046101–, 2012. http://dx.doi.org/10.1063/1.3686184.

[42] Jihene Zribi, Bouraoui Ilahi, Bernard Paquette, Abdelatif Jaouad, Olivier Theriault, Karin Hinzer, Ross Cheriton, Gilles Patriarche, Simon Fafard, Vincent Aimez, Richard Ares, and Denis Morris. Effect of dot-height truncation on the device performance of multilayer InAs/GaAs quantum dot solar cells. *IEEE Journal of Photovoltaics*, **6**(2):1–6, 2016. https://doi.org/10.1109/JPHOTOV.2016.2514708.

[43] V. Srimurugan, R. Sundheep, J. E. M. Haverkort, and R. Prasanth. Investigation of size and barrier dependent efficiency in InAs quantum dot solar cells. *Materials Today: Proceedings*, **80**(3):2602–2609, 2023. https://doi.org/10.1016/j.matpr.2021.06.418.

[44] Photovoltaic Specialists Conference. *Optimum design of InGaP/GaAs/Ge triple-junction solar cells with sub-wavelength surface texture structure*, number **37** in 37. IEEE, 2011. https://doi.org/10.1109/PVSC.2011.6186360.

[45] A. Aissat, S. Nacer, and J. P. Vilcot. Effect of $In_{0.70}Ga_{0.30}As$ quantum dot insertion in the middle cell of $In_yGa_{1-y}P/In_xGa_{1-x}As/Ge$ triple-junction for solar cells. *https://doi.org/10.1016/j.spmi.2020.106760*, 2000.

[46] Photovoltaic Specialists Conference. *InGaP/GaAs/Ge Multi-Junction Solar Cell Efficiency Improvements Using Epitaxial Germanium*, number **28** in 28. IEEE, 09 2000. https://doi.org/10.1109/PVSC.2000.916053.

[47] Jenny Nelson. *The physics of solar cells*. Imperial College, UK, 2007.

[48] Richard H. Bube. *Photovoltaic Materials*, volume 1. Imperial college press, 1998.

[49] Donald A. Neamen. *Semiconductor Physics and Devices: Basic Principles*. McGraw-Hill, fourth edition, 2012.

[50] S. M. Sze and Kwok K. Ng. *Physics of Semiconductor Devices*. John Wiley and Sons, 3 edition, 2007.

[51] Jasprit Singh. *Electronic and Optoelectronic Properties of Semiconductor Structure*. UIT Cambridge, 2003.

[52] Antonio Luque and Steven Hegedus. *Handbook of Photovoltaic Science and Engineering*. A John Wiley and Sons, Ltd., second edition, 2011. pp. 343.

[53] David L. Pulfrey. *Understanding Modern Transistors and Diodes || np- and Np-junction basics.*, chapter 6, pages 91–115. Cambridge University Press, 2010. https://doi.org/10.1017/CBO9780511840685.007.

[54] Antonio Luque and Steven Hegedus. *Handbook of Photovoltaic Science and Engineering*. John Wiley and Sons Ltd, 2003.

[55] C. B. Honsberg and S. G. Bowden. *Photovoltaics Education Website*. 2019. www.pveducation.org.

[56] Harold J. Hovel. *Semiconductor and Semimetals: Solar Cells*, volume 11. Acadamic Press, 1975.

[57] Antonio Luque and Antonio Marti. The intermediate band solar cell: Progress toward the realization of an attractive concept. *Advanced Materials*, **22**(2):160–174, 2010. http://dx.doi.org/10.1002/adma.200902388.

[58] William Shockley and Hans J. Queisser. Detailed balance limit of efficiency of p-n junction solar cells. *Journal of applied physics*, **32**(3):510–519, 1961. http://dx.doi.org/10.1063/1.1736034.

[59] P. Palacios, J. Fernandez, K. Sanchez, J. Conesa, and P. Wahnon. First-principles investigation of isolated band formation in half-metallic $Ti_xGa_{1x}P$ (x=0.3125–0.25). *Physical Review B*, **73**(8):1–8, 2006. http://dx.doi.org/10.1103/PhysRevB.73.085206.

[60] C. Tablero. Optoelectronic properties of Cr-substituted II–VI semiconductors. *Computational Materials Science*, **37**(4):483–490, 2006. https://doi.org/10.1016/j.commatsci.2005.11.009.

[61] P. Pacios, K. Sanchez, J. C. Conesa, and P. Wahnon. First principles calculation of isolated intermediate bands formation in a transition metal-doped chalcopyrite-type semiconductor. *Physica status solidi*, **203**(6):1395–1401, 2006. https://doi.org/10.1002/pssa.200566179.

[62] Weiming Wang, Albert S. Lin, and Jamie D. Phillips. Intermediate-band photovoltaic solar cell based on ZnTe:O. *Applied Physics Letters*, **95**(1):011103, 2009. http://dx.doi.org/10.1063/1.3166863.

[63] Weiming Wang, Albert S. Lin, Jamie D. Phillips, and Wyatt K. Metzger. Generation and recombination rates at ZnTe:O intermediate band states. *Applied Physics Letters*, **95**(26):261107, 2009. http://dx.doi.org/10.1063/1.3274131.

[64] A. Zrenner. A close look on single quantum dots. *The Journal of Chemical Physics*, **112**(18):7790, 2000. http://dx.doi.org/10.1063/1.481384.

[65] A. Marti, L. Cuadra, and A. Luque. Partial filling of a quantum dot intermediate band for solar cells. *IEEE Trans. Electron Devices*, **48**(10):2394–2399, 2001. http://dx.doi.org/10.1109/16.954482.

[66] R. B. Laghumavarapu, A. Moscho, A. Khoshakhlagh, M. El-Emawy, and L. F. Lester. GaSb/GaAs type II quantum dot solar cells for enhanced

infrared spectral response. *Applied physics letters*, **90**(17):173125, 2007. https://doi.org/10.1063/1.2734492.

[67] K. A. Sablon, J. W. Little, V. Mitin, A. Sergeev, and N. Vagidov. Strong enhancement of solar cell efficiency due to quantum dots. *Nano Letters*, **11**(6):2311–2317, 2011. https://doi.org/10.1021/nl200543v.

[68] D. Zhou, G. Sharma, S. F. Thomassen, T. W. Reenaas, and B. O. Fimland. Optimization towards high density quantum dots for intermediate band solar cells grown by molecular beam epitaxy. *Applied Physics Letters*, **96**(6):061913–3, 2010. https://doi.org/10.1063/1.3313938.

[69] R. Oshima, A. Takata, and Y. Okada. Strain-compensated InAs/GaNAs quantum dots for use in high-efficiency solar cells. *Applied Physics Letters*, **93**(8):083111, 2008. https://doi.org/10.1063/1.2973398.

[70] Yeongho Kim, Keun-Yong Ban, and Christiana B. Honsberg. Multi-stacked InAs/GaAs quantum dots grown with different growth modes for quantum dot solar cells. *Applied Physics Letters*, **106**(22):222104, 2015. http://dx.doi.org/10.1063/1.4922274.

[71] Christopher G. Bailey, David V. Forbes, Stephen J. Polly, Zachary S. Bittner, Yushuai Dai, Chelsea Mackos, Ryne P. Raffaelle, and Seth M. Hubbard. Open-circuit voltage improvement of InAs/GaAs quantum-dot solar cells using reduced inas coverage. *IEEE Journal of Photovoltaics*, **2**(3):269–275, 2012. http://dx.doi.org/10.1109/JPHOTOV.2012.2189047.

[72] A. Luque, A. Marti, E. Antolin, P. G. Linares, I. Tobias, and I. Ramiro. Radiative thermal escape in intermediate band solar cells. *AIP Advances*, **1**(2):022125–, 2011. http://dx.doi.org/10.1063/1.3597326.

[73] E. Antolin, A. Marti, C. R. Stanley, C. D. Farmer, E. Canovas, N. Lopez, P. G. Linares, and A. Luque. Low temperature characterization of the photocurrent produced by two-photon transitions in a quantum dot intermediate band solar cell. *Thin solid films*, **516**(20):6919–6923, 2008. http://dx.doi.org/10.1016/j.tsf.2007.12.061.

[74] Y. Okada, T. Morioka, K. Yoshida, R. Oshima, Y. Shoji, T. Inoue, and T. Kita. Increase in photocurrent by optical transitions via intermediate states in direct-doped InAs/GaNAs strain-compensated quantum dot solar cell. *Journal of applied physics*, **109**(2):024301, 2011. https://doi.org/10.1063/1.3533423.

[75] A. Marti, E. Antolin, E. Canovas, N. Lopez, P. G. Linares, A. Luque, C. R. Stanley, and C. D. Farmer. Elements of the design and analysis of quantum-dot intermediate band solar cells. *Thin Solid Films*, **516**(20):6716–6722, 2008. http://dx.doi.org/10.1016/j.tsf.2007.12.064.

[76] S. Tomic, T. S. Jones, and N. M. Harrison. Absorption characteristics of a quantum dot array induced intermediate band: Implications for solar cell design. *Applied Physics Letters*, **93**(26):263105, 2008. http://dx.doi.org/10.1063/1.3058716.

[77] A. Marti, N. Lopez, E. Antolin, E. Canovas, C. Stanley, C. Farmer, L. Cuadra, and A. Luque. Novel semiconductor solar cell structures: The quantum dot intermediate band solar cell. *Thin Film and Nanostructured Materials for Photovoltaics*, **511-512**:638–644, 2006. http://dx.doi.org/10.1016/j.tsf.2005.12.122.

[78] Martin A. Green, Ewan D. Dunlop, Masahiro Yoshita, Nikos Kopidakis, Karsten Bothe, Gerald Siefer, and Xiaojing Hao. Solar cell efficiency tables (version 63). *Prog Photovolt Res Appl.*, **32**(1):3-13, 2024. https://doi.org/10.1002/pip.3750.

[79] Martin A. Green, Ewan D. Dunlop, Gerald Siefer, Masahiro Yoshita, Nikos Kopidakis, Karsten Bothe, and Xiaojing Hao. Solar cell efficiency tables (version 61). *Prog Photovolt Res Appl.*, **31**(1):3-16, 2023. https://doi.org/10.1002/pip.3646.

[80] Robert McConnell and Vasilis Fthenakis. *Third Generation Photovoltaics || Concentrated Photovoltaics*, chapter 7. InTech, 2012. https://doi.org/10.5772/39245.

[81] Ryne Raffaelle, Samar Sinharoy, John Andersen, David Wilt, and Sheila Bailey. Multi-junction solar cell spectral tuning with quantum dots. volume **1**, page 162–166. IEEE 4^{th} World Conference on Photovoltaic Energy Conference, IEEE Photovoltaic Energy Conversion, June 2006. https://doi.org/10.1109/WCPEC.2006.279407.

[82] G.F. Brown and J. Wu. Third generation photovoltaics. *Laser and Photonics Reviews*, **3**(4):394–405, 2009. https://doi.org/10.1002/lpor.200810039.

[83] Y. Nakata and Y. Sugiyama. *Semiconductors and Semimetals || Molecular Beam Epitaxial Growth of Self-Assembled InAs/GaAs Quantum Dots*, volume **60**, chapter 2, pages 117–154. Academic Press, 1999.

[84] A. A. Darhuber, V. Holy, J. Stangl, G. Bauer, A. Krost, F. Heinrichsdorff, M. Grundmann, D. Bimberg, V. M. Ustinov, P. S. Kopev, A. O. Kosogov, and P. Werner. Lateral and vertical ordering in multilayered self-organized ingaas quantum dots studied by high resolution x-ray diffraction. *Applied Physics Letters*, **70**(8):955–957, 1997. https://doi.org/10.1063/1.118463.

[85] D. B. Bushnell, T. N. D. Tibbits, K. W. J. Barnham, J. P. Connolly, M. Mazzerb, N. J. Ekins-Daukes, J. S. Roberts, G. Hill, and R. Airey. Effect of well number on the performance of quantum-well solar cells. *Journal of applied physics*, **97**(12):124908, 2005. http://dx.doi.org/10.1063/1.1946908.

[86] M. C. Lynch, I. M. Ballard, D. B. Bushnell, J. P. Connolly, D. C. Johnson, K. W. J. Barnham T. N. D. Tibbits, N. J. Ekinsdaukes, J. S. Roberts, G. Hill, R. Airey, and M. Mazzer. Spectral response and I-V characteristics of large well number multi quantum well solar cells. *Journal of materials science*, **40**(6):1445–1449, 2005. http://dx.doi.org/10.1007/s10853-005-0580-4.

[87] Abiseka Akash Ganesan. *Quantum dot solar cells and electrochemical doping of QD films*. Master's thesis, Delft University of Technology, 2018.

[88] H. L. Weng, H. Y. Ueng, and C. P. Lee. Efficiency of quantum dot solar cell enhanced by improving quantum dots performance. *Physica Status Solidi (A)*, **212**(2):369–375, 2014. http://dx.doi.org/10.1002/pssa.201431261.

[89] Jafar Fathi, Hassan Babaei, Arash Nikniazi, Khadije Khalili, Hossein Movla, Foozieh Sohrabi, and Nima Es'haghi Gorji. Photocurrent and surface recombination mechanisms in the $In_xGa_{1x}N/GaN$ different-sized quantum dot solar cells. *Turkish Journal of Physics*, **34**:97–106, 2010. http://dx.doi.org/10.3906/fiz-1002-19.

[90] Nima Es'haghi Gorji, Hossein Movla, Foozieh Sohrabi, Ahmad Hosseinpour, Meisam Rezaei, and Hassan Babaei. The effects of recombination lifetime on efficiency and j–v characteristics of $In_xGa_{1-x}N$/GaN quantum dot intermediate band solar cell. *Physica E*, **42**(9):2353–2357, 2010. http://dx.doi.org/10.1016/j.physe.2010.05.014.

[91] V. Aroutiounian, S. Petrosyan, K. Touryan, and A. Khachatryan. Quantum dot solar cells. *Journal of applied physics*, **89**(4):2268, 2001. http://dx.doi.org/10.1063/1.1339210.

[92] H. I. Ikeri, A. I. Onyia, and P. U. Asogwa. Theoretical investigation of the size effect on energy gap of CdSe, ZnS and GaAs quantum dots using particle in a box model. *Chalcogenide Letters*, **14**(2):49–54, 2017.

[93] Martin A. Green. Solar cell fill factors: General graph and empirical expressions. *Solid-State Electronics*, **24**(8):788–789, 1981. https://doi.org/10.1016/0038-1101(81)90062-9.

[94] M. Levinshtein, S. Rumyantsev, and M. Shur. *Handbook Series on Semiconductor Parameters*, volume 1. World Scientific Publishing, 1996.

[95] Imran A., Jiang J., Eric D., Zahid M. N., Yousaf M., and Shah Z. Optical properties of InAs/GaAs quantum dot superlattice structures. *Results in Physics*, **9**:297–302, 2018. http://dx.doi.org/10.1016/j.rinp.2018.02.016.

[96] Edik U. Rafailov, Maria Ana Cataluna, and Eugene A. Avrutin. *Ultrafast lasers based on quantum dot structures*. Wiley, 2011.

[97] D. L. Ferreira and J. L. Alves. The effects of shape and size nonuniformity on the absorption spectrum of semiconductor quantum dots. *Nanotechnology*, **15**(8):975–981, 2004. http://dx.doi.org/10.1088/0957-4484/15/8/019.

[98] A. P. Zhou and W. D. Sheng. Electron and hole effective masses in self-assembled quantum dots. *The European Physical Journal B*, **68**(2):233–236, 2009. http://dx.doi.org/10.1140/epjb/e2009-00098-2.

[99] Menberu Mengesha. Linear and saturable nonlinear optical properties of GaAs quantum dot. *Lat. Am. J. Phys. Educ.*, **7**(2):326, 2013.

[100] Katsuyoshi Sakamoto, Yasunori Kondo, Keisuke Uchida, and Koichi Yamaguchi. Quantum-dot density dependence of power conversion efficiency of intermediate-band solar cells. *Journal of applied physics*, **112**(12):124515, 2012. http://dx.doi.org/10.1063/1.4771925.

[101] Christopher G. Bailey. *Optical and Mechanical Characterization of InAs/GaAs Quantum Dot Solar Cells*. PhD thesis, Rochester Institute of Technology, 2012.

[102] Guodan Wei and Stephen R. Forrest. Intermediate-band solar cells employing quantum dots embedded in an energy fence barrier. *Nano Letters*, **7**(1):218–222, 2007. https://dx.doi.org/10.1021/nl062564s.

[103] Nima Eshaghi Gorji. A theoretical approach on the strain-induced dislocation effects in the quantum dot solar cells. *Solar Energy*, **86**(3):935–940, 2012. http://dx.doi.org/10.1016/j.solener.2011.12.024.

[104] H. I. Ikeri, A. I. Onyia, and O. J. Vwavware. The dependence of confinement energy on the size of quantum dots. *International Journal of Scientific Research in Physics and Applied Sciences*, **7**(2):27–30, 2019. https://doi.org/10.26438/ijsrpas/v7i2.2730.

[105] Yuchang Wu and Levon V. Asryan. Theory of photovoltaic characteristics of semiconductor quantum dot solar cells. *Journal of Applied Physics*, **120**(8):084302, 2016. http://dx.doi.org/10.1063/1.4961046.

[106] Khalil Ebrahim Jasim. *Solar Cells- New Approaches and Reviews ||Quantum Dots Solar Cells*, chapter 11, pages 303–331. IntechOpen, Rijeka, Oct 2015. http://dx.doi.org/10.5772/59159.

[107] Stephen P. Bremner, Richard Corkish, and Christiana B. Honsberg. Detailed balance efficiency limits with quasi-fermi level variations. *IEEE Transactions on Electron Devices*, **46**(10):1932–1939, 1999. http://dx.doi.org/10.1109/16.791981.

[108] L. Cuadra, A. Marti, and A. Luque. Type II broken band heterostructure quantum dot to obtain a material for the intermediate band solar cell. *Physica E: Low-dimensional Systems and Nanostructures*, **14**(1):162–165, 2002. http://dx.doi.org/10.1016/S1386-9477(02)00370-3.

[109] Hossein Movla, Foozieh Sohrabi, Jafar Fathi, Hassan Babaei, Arash Nikniazi I, Khadije Khalili, and Nima Es'haghi Gorji. Photocurrent and surface recombination mechanisms in $In_xGa_{1-x}N/GaN$ different-sized quantum do t solar cells. *Turkish Journal of Physics*, **34**(2):97–106, 2010. http://dx.doi.org/10.3906/fiz-1002-19.

[110] P. Hari Krishna and Meera Ramrakhiani. Effect of particle size distribution on spectral characteristics of different quantum dots. *International Journal of Applied Engineering Research*, **13**(3):1722–1727, 2018.

[111] WeiYu Wu, J. N. Schulman, T. Y. Hsu, and Uzi Efron. Effect of size nonuniformity on the absorption spectrum of a semiconductor quantum dot system. *Applied physics letters*, **51**:710, 1987. http://dx.doi.org/10.1063/1.98896.

[112] Subindu Kumar and Dipankar Biswas. Effects of a Gaussian size distribution on the absorption spectra of III-V semiconductor quantum dots. *Journal of applied physics*, **102**:084305, 2007. http://dx.doi.org/10.1063/1.2798986.

[113] Sayantan Biswas, Avigyan Chatterjee, Ashim Kumar Biswas, and Amitabha Sinha. Spectral response of the intrinsic region of a GaAs-InAs quantum dot solar cell considering the absorption spectra of ideal cubic dots. *Physica E: Low-dimensional systems and nanostructures*, **84**:108, 2016. http://dx.doi.org/10.1016/j.physe.2016.05.043.

[114] Shabbir S. Bohra and Ashish K. Panchal. Investigation on current collection from a silicon quantum-dot p-i-n solar cell by varying dot size and insulating barrier layer thickness. *Journal of Nanomaterials, Nanoengineering and Nanosystems*, **230**(1):44–50, 2016. http://dx.doi.org/10.1177/1740349914541646.

[115] Pingrong Yu, Matthew C. Beard, Randy J. Ellingson, Suzanne Ferrere, Calvin Curtis, John Drexler, and Fred Luiszerand Arthur J. Nozik. Absorption cross-section and related optical properties of colloidal InAs quantum dots. *The Journal of Physical Chemistry B*, **109**(15):7084–7087, 2005. https://doi.org/10.1021/jp046127i.

[116] Cedrik Meier, Andreas Gondorf, Stephan Luttjohann, Axel Lorke, and Hartmut Wiggers. Silicon nanoparticles: Absorption, emission, and the nature

of the electronic bandgap. *Journal of Applied Physics*, **101**(10):103112, 2007. http://dx.doi.org/10.1063/1.2720095.

[117] Ryuji Oshima, Yoshitaka Okada, Ayami Takata, Shuhei Yagi, Kouichi Akahane, Ryo Tamaki, and Kenjiro Miyano. High-density quantum dot superlattice for application to high-efficiency solar cells. *Phys. Status Solidi C*, **8**(2):619–621, 2011. http://dx.doi.org/10.1002/pssc.201000461.

[118] T. K. Nideep, M. Ramya, and M. Kailasnath. The influence of ZnS buffer layer on the size dependent efficiency of CdTe quantum dot sensitized solar cell. *Superlattices and Microstructures*, **130**:175–181, 2019. http://dx.doi.org/10.1016/j.spmi.2019.04.034.

[119] K. Veerathangam, Muthu Senthil Pandian, and P. Ramasamy. Size-dependent photovoltaic performance of cadmium sulfide (CdS) quantum dots for solar cell applications. *Journal of Alloys and Compounds*, **735**:202–208, 2018. https://doi.org/10.1016/j.jallcom.2017.11.055.

[120] Yunqing Cao, Ping Zhu, Dongke Li, Xianghua Zeng, and Dan Shan. Size-dependent and enhanced photovoltaic performance of solar cells based on Si quantum dots. *Energies*, **13**(18):4845, 2020. http://dx.doi.org/10.3390/en13184845.

[121] Qinghui Shao. *Optimized designs and materials for nanostructure based solar sells.* PhD thesis, University of California, Riverside, 2009.

[122] Q. Shao, A. A. Balandin, A. I. Fedoseyev, and M. Turowski. Intermediate-band solar cells based on quantum dot supracrystals. *Applied Physics Letters*, **91**(16):163503, 2007. http://dx.doi.org/10.1063/1.2799172.

[123] Wolfgang J. Parak, Liberato Manna, and Thomas Nann. *Nanotechnology || Fundamental Principles of Quantum Dots*, volume 1, chapter 4, pages 73–96. John Wiley and Sons, Ltd, 2010. http://dx.doi.org/10.1002/9783527628155.nanotech004.

[124] Sanjib Kabi, Siddhartha Panda, and Dipankar Biswas. Computations of the optical transitions and absorption spectra in a set of realistic, elongated InAs/GaAs quantum boxes having a gaussian distribution. *Journal of Applied Physics*, **109**(5):053110, 2011. http://dx.doi.org/10.1063/1.3549151.

[125] K. W. Sun, A. Kechiantz, B. C. Lee, and C. P. Lee. Ultrafast carrier capture and relaxation in modulation-doped InAs quantum dots. *Applied Physics Letters*, **88**:163117, 2006. http://dx.doi.org/10.1063/1.2197309.

[126] J. Y. Marzin, J. M. Gerard, A. Izrael, and D. Barrier. Photoluminescence of single InAs quantum dots obtained by self-organized growth on GaAs. *Physical review letters*, **73**(5):716, 1994. https://doi.org/10.1103/PhysRevLett.73.716.

[127] K. H. Schmidt, G. Medeiros-Ribeiro, and P. M. Petroff. Photoluminescence of charged InAs self-assembled quantum dots. *Physical review B*, **58**(7):3597–3600, 1998. https://link.aps.org/doi/10.1103/PhysRevB.58.3597.

[128] T. Mano, R. Notzel, G. J. Hamhuis, T. J. Eijkemans, and J. H. Wolter. Formation of InAs quantum dot arrays on GaAs (100), by self-organized anisotropic strain engineering of a (In, Ga)As superlattice template. *Applied Physics Letters*, **81**(9):1705–1707, 2002. http://dx.doi.org/10.1063/1.1503872.

[129] Haihua Yang, Wenguang Fan, Aleksandar Vaneski, Andrei S. Susha, Wey Yang Teoh, and Andrey L. Rogach. Heterojunction engineering of CdTe and CdSe quantum dots on TiO_2 nanotube arrays: Intricate effects of size- dependency and interfacial contact on photoconversion efficiencies. *Advanced Functional Materials*, **22**(13):2821–2829, 2012. http://dx.doi.org/10.1002/adfm.201103074.

[130] Slobodan Cicic. *Heuristic Modelling of Multijunction Solar Cells Using a Parallel Genetic Algorithm*. Phd thesis, University of Salford School of Computing, Science and Engineering, Manchester, 2018.

[131] Gui Jiang Lin, Jingfeng Bi, Minghui Song, Jianqing Liu, Weiping Xiong, and Meichun Huang. *III-V Multi-Junction Solar Cells*, chapter 11, pages 445–471. InTech, second edition, 2013. http://dx.doi.org/10.5772/50965.

[132] Frank Dimroth and Sarah Kurtz. High-efficiency multijunction solar cells. *MRS Bulletin*, **32**:230–235, 2007. https://doi.org/10.1557/mrs2007.27.

[133] R. R. King, D. C. Law, K. M. Edmondson, C. M. Fetzer, and G. S. Kinsey. 40% efficient metamorphic GaInP/GaInAs/Ge multijunction solar cells. *Applied Physics Letters*, **90**:183516, 2007. http://dx.doi.org/10.1063/1.2734507.

[134] Inigo Ramiro, Juan Villa, Phu Lam, Sabina Hatch, Jiang Wu, Esther Lopez, Elisa Antolin, Huiyun Liu, Antonio Marti, and Antonio Luque. Wide-bandgap InAs/InGaP quantum-dot intermediate band solar cells. *IEEE journal of photovoltaics*, **5**(3), 2015. https://dx.doi.org/10.1109/JPHOTOV.2015.2402439.

[135] J. F. Geisz, D. J. Friedman, J. S. Ward, A. Duda, W. J. Olavarria, T. E. Moriarty, J. T. Kiehl, M. J. Romero, A. G. Norman, and K. M. Jones. 40.8% efficient inverted triple-junction solar cell with two independently metamorphic junctions. *Applied Physics Letters*, **93**:123505, 2008. http://dx.doi.org/10.1063/1.2988497.

[136] Masafumi Yamaguchi, Tatsuya Takamoto, Kenji Araki, and Nicholas Ekins-Daukes. Multi-junction III–V solar cells: current status and future potential. *Solar Energy*, **79**:78–85, 2005. http://dx.doi.org/10.1016/j.solener.2004.09.018.

[137] Yiming Bai, Lingling Yan, Jun Wang, Lin Su, Zhigang Yin, Nuofu Chen, and Yuanyuan Liu. Enhancing the photocurrent of top-cell by ellipsoidal silver nanoparticles: Towards current-matched GaInP/GaInAs/Ge triple-junction solar cells. *Nanomaterials*, **6**(6):98, 2016. https://doi.org/10.3390/nano6060098.

[138] Lei Zhang, Pingjuan Niu, Yuqiang Li, Minghui Song, Jianxin Zhang, Pingfan Ning, and Peizhuan Chen. Investigation on high-efficiency $Ga_{0.51}In_{0.49}P/In_{0.01}Ga_{0.99}As/Ge$ triple-junction solar cells for space applications. *AIP Advances*, **7**(12):125217, 2017. https://doi.org/10.1063/1.5006865.

[139] Lin Guijiang, Wu Jyhchiarng, and Huang Meichun. Theoretical modeling of the interface recombination effect on the performance of III–V tandem solar cells. *Journal of Semiconductors*, **31**(8), 2010. https://dx.doi.org/10.1088/1674-4926/31/8/082004.